Permeability of rubble mound breakwaters and its effect on wave overtopping

Master thesis

Mikkel Houe

Mathias Wilsfort Lund

Aalborg University

Study board of the Built Environment

M.Sc Structural and Civil Engineering
Aalborg University
http://www.aau.dk

STUDENT REPORT

Title:
Permeability of rubble mound breakwaters and its effect on overtopping

Theme:
Marine structures

Project period:
2023.02.01 to 2023.06.09

Project type:
Master thesis 30 ECTS

Participants:
Mikkel Houe
Mathias Wilsfort Lund

Supervisors:
Claes Eskilsson
Thomas Lykke Andersen
Mads Røge Eldrup

Pages:
100

Due date:
2023.06.09

Preface

The present 30 ECTS master thesis is submitted on 9. June 2023 as part of the final semester of the structural and civil engineering master's at Aalborg University.

The project is devised under the supervision of Thomas Lykke Andersen, Mads Røge Eldrup and Claes Eskilsson to whom a big thanks is owed.

The experimental laboratory equipment provided by Aalborg University as well as help from the laboratory technicians was essential in conducting the experiments and therefore deserves a mention.

Reading instructions

In the report, citations are made with the use of the Harvard-method. The citations are therefore written out as [Author, Year] or Author [Year]. When referencing to figure or table it will be written as Figure/Table X.X, where references to equations will be written as Eq. (X.X). Units are provided in SI-format when appropriate.

This thesis should be printed in color, in order to obtain the full understanding.

Contents

Summary

The current guidelines for designing for wave overtopping offer no intermediate level of core permeability for the engineer when designing rock armoured rubble mound breakwaters. The permeability is quantified by the influence factor of roughness elements on a slope, γ_f. The current guidelines consider only extreme values of either impermeable or permeable cores, when dealing with armour unit type rock. The limitation of any nuanced level of permeability might lead to an overestimation of the calculated wave overtopping rates. In contrast, designing for stability, the permeability of a rubble mound breakwater can be described in a variety of ways, through the notional permeability factor P. However, the majority of research on the impact of core permeability on wave overtopping has been conducted on permeable cores. In contrast, the guidelines for impermeable cores are based on wave run-up data, leaving gaps in the current design codes. The present project studied the effects of permeability on wave overtopping, of rock armoured rubble mound breakwaters.

Extensive experimental work has been conducted on small-scale breakwater models with five separate layer compositions with varying permeability. The purpose was to study the influence of structure permeability on roughness, γ_{P*}, in regards to wave overtopping, based on the relevant ranges of wave steepness and relative freeboards. Furthermore, multiple test was conducted on highly impermeable and permeable structures, in order to cover dispersion of the upper- and lower limits of permeability. The present wave overtopping tests showed that the current guidelines greatly overestimate γ_{P*} on structures with impermeable cores. A recommendation to remove the differentiation between impermeable and permeable cores for rock armoured breakwaters is proposed, which significantly increases the accuracy in estimating wave overtopping.

This project also attempted to replicate the experimental results, through Computational Fluid Dynamic (CFD) simulations, by simulating regular wave series, on two experimental tested breakwater models. The replicated surface elevation was found to agree well with the measured signal from the wave flume. There was, however, a discrepancy in the measured overtopping volumes of the numerical and experimental models. Data collected from the experimental work in the wave flume is considered more reliable than data from the numerical model. Nevertheless, the results of the model indicated a small influence of the core permeability on the wave overtopping. The numerical data was greatly limited and no consistent trend was observed.

Summary in danish

Ved design af bølgeoverskyld for stenkastnings moler er ingeniøren i dag nødt til at træffe et valg mellem en permeabel eller impermeabel kerne. Permeabiliteten kvantificeres af faktoren for ruhedselementer på molens skråning γ_f, men disse retningslinjer tager kun hensyn til ekstremer, heraf enten impermeabel eller permeabel kerne. Denne begrænsning fører til relativt store design forskelle i det nødvendige fribord. I modsætning hertil kan permeabiliteten af en stenkastnings mole beskrives på forskellige måder ved design for stabilitet, gennem den såkaldte imaginære permeabilitetsfaktor P.

Flertallet af undersøgelser om kernepermeabilitetens indvirkning på bølgeoverskyld er udført på permeable kerner. I modsætning hertil er retningslinjerne for impermeable kerner ikke baseret på overskyldsdata, hvilket efterlader huller i de nuværende designkoder. Det nuværende projekt undersøgte indflydelsen af permeabilitet på bølgeoverskyld for stenkastnings moler.

Omfattende eksperimentelt arbejde er udført på mindre skala modeller af moler med fem separate lagssammensætninger med varierende permeabilitet. Formålet var at undersøge indflydelsen af molens permeabilitet på ruhedsfaktoren, γ_{P*}, i forhold til bølgeoverskyld. Relevante intervaller af bølgestejlhed og relative friborde er blevet undersøgt. Der blev samtidigt udført flere tests på stærkt impermeable og permeable moler for at dække spredningen af γ_{P*} på de øvre og nedre grænser for permeabilitet. De udførte overskyldstest viser, at de nuværende retningslinjer i høj grad overestimerer γ_{P*} på moler med impermeable kerner. Dette resulterede i en anbefaling om at fjerne differentieringen mellem impermeable og permeable kerner for stenkastnings moler, hvilket væsentligt øger nøjagtigheden ved estimering af bølgeoverskyld.

Dette projekt forsøgte samtidigt at genskabe disse eksperimentelle resultater gennem Computational Fluid Dynamic (CFD) simuleringer. De genskabte bølgetog korreleret fint med de målte signaler fra bølgeranden. Derimod, var der en uoverensstemmelse imellem det målte og det simulerede bølgeoverskyld. Data indsamlet fra det eksperimentelle arbejde, var dog vurderet til at være mest pålidelig. Ikke desto mindre, indikerede resultaterne fra den numeriske model, at kernepermeabiliteten havde en lille indflydelse på bølgeoverskyllet. Dog var størrelsen på det numeriske dataset så lille at ingen forenelig sammenhæng var observeret.

Introduction 1

The present project studies the effects of permeability on wave overtopping of rock armoured rubble mound breakwaters. The prediction of overtopping discharges involves complex physical phenomena such as wave breaking and porous flow in the core and outer layers. A fundamental understanding of the hydraulic response and composition of the breakwater layout is therefore essential for the study of wave overtopping.

The objective of rubble mound breakwaters is to mitigate wave action in harbours to obtain allowable conditions for vessels harbouring within. Breakwaters are also used in relation to the protection of coastline and navigation channels from wave attack and sediment transport. A layout of a conventional breakwater without a crown wall is shown in Figure 1.1.

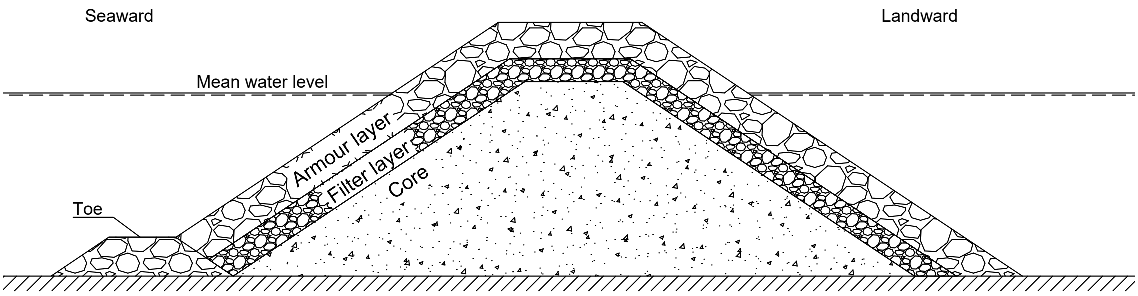

Figure 1.1. Illustration of breakwater layout without a crown wall.

Rubble mound breakwaters are generally constructed with a core, filter and armour layer. The core consists of sand, rubble or quarry-run which is then covered by one or more filter layers of larger rock material to prevent outwash of the core through the armour layer. The armour layer is the outermost layer and serves to protect the core material, by absorbing energy from wave attacks on the front and overtopping on the rear side. Commonly the breakwater is designed with a toe to prevent scour, causing the armour layer to slide down and exposing the filter layer or core. [USACE, 2002]

Energy from the incident wave is dissipated mainly through wave breaking on the front slope of the breakwater and through viscous forces in the core and protective layers. Some energy is reflected back and some is transmitted through the breakwater by wave overtopping or penetration. An important design consideration for rubble mound breakwaters is a safe design level of the hydraulic response, such as wave run-up, wave overtopping, wave transmission and wave reflection. Understanding of the physical processes is fundamental for describing the influence of permeability on overtopping. [USACE, 2002]

1.1 Physical processes

The distribution of the wave energy depends on the incident wave and the geometry and layer composition of the breakwater layout. Considering an impermeable smooth slope, no energy is dissipated through the structure and more energy is as a result dissipated upwards along the slope. In relation, a narrow grading or a small rock size of the core material will create an impermeable slope, where run-up R_{up} and run-down R_d will occur in the outermost permeable layers, such as the filter and armour layer causing more energy dissipation compared to a smooth slope. Run-up and run-down are measured as the highest and lowest vertical distance reached by the incident wave from the mean water level (MWL).

For an impermeable slope, no energy will be transmitted through or absorbed in the core and a higher run-up level is thus expected. Consequently also more run-down occurs and larger destabilising drag forces are exerted on the armour units. Contrary, a wide grading or a larger rock size of the core material creates a more permeable slope and more energy is dissipated in the core causing a lower run-up level. Figure 1.2 illustrates the flow variation and flow velocity vectors for an impermeable and permeable slope. [USACE, 2002]

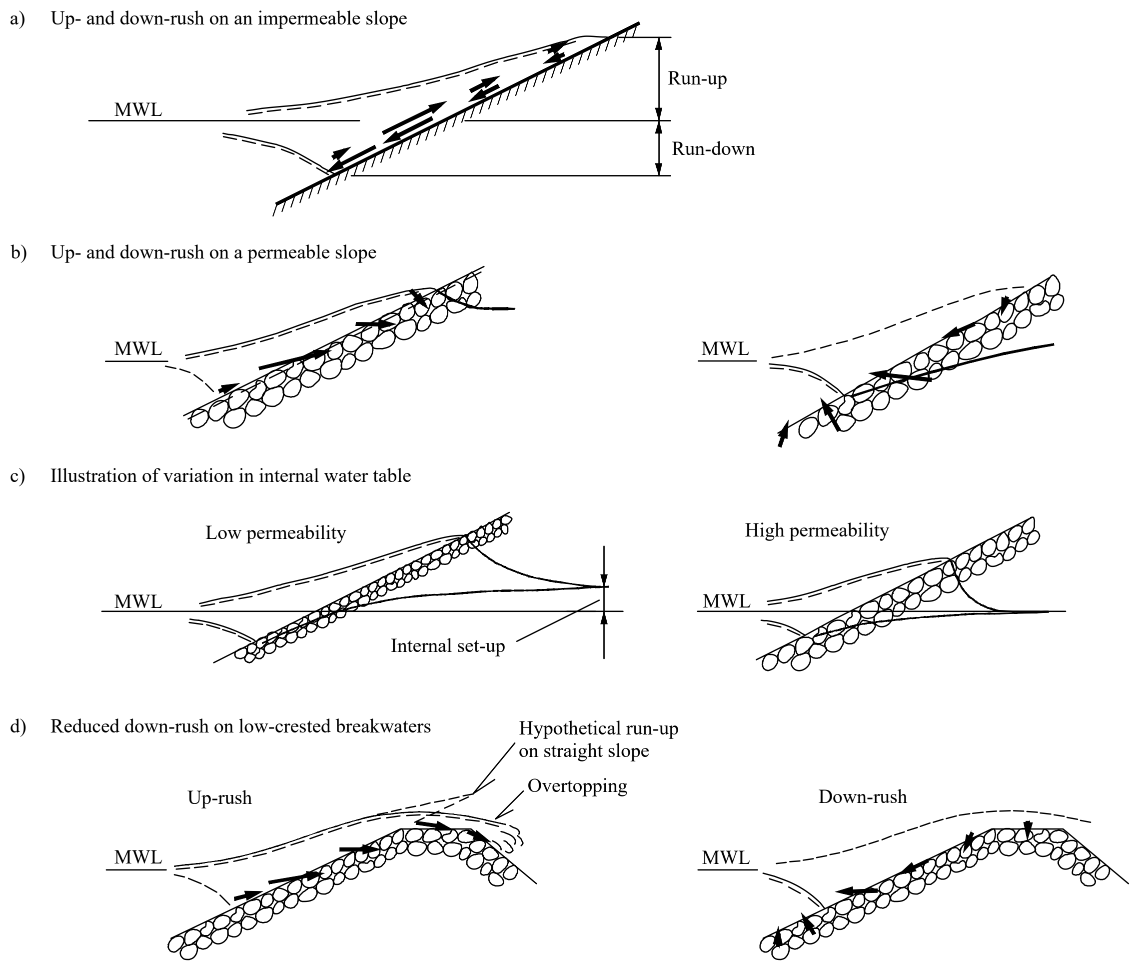

Figure 1.2. Illustration of run-up and run-down on an impermeable and permeable slope. [USACE, 2002]

If the run-up level exceeds the crest height, energy is passed over the structure in the form of wave overtopping. Allowing greater amounts of overtopping to pass the crest reduces the run-down on the front slope and thereby the destabilising flow forces. However, greater amounts of overtopping, can have a negative impact on what the breakwater is essentially protecting, such as access roads or public footpaths.

Wave impact on the front slope can greatly influence the run-up level reached by the wave. When the wave approaches the front slope a wave structure interaction occurs, that might cause the wave to break. The type of wave breaking varies and is described as spilling, collapsing, plunging or surging. The observed type of wave breaking is illustrated in Figure 1.3 and is characterised by the surf similarity parameter $\xi = \tan(\alpha)/(s)^{0.5}$, where α is the slope angle and $s = H/L$ is the wave steepness, where H is the wave height used in combination with the wavelength $L = gT^2/(2\pi)$. The surf similarity parameter is determined differently for irregular waves $\xi_{m-1,0}$ and regular waves ξ_0. The spectral wave height H_{m0} and wave period $T_{m-1,0}$ are used for computing the spectral wave steepness $s_{m-1,0} = H_{m0}/L_{m-1,0}$ for $\xi_{m-1,0}$ and for regular waves, the deep water wave height H_0 and wave period T_0 is used for the deep water steepness $s_0 = H_0/L_0$ for ξ_0.

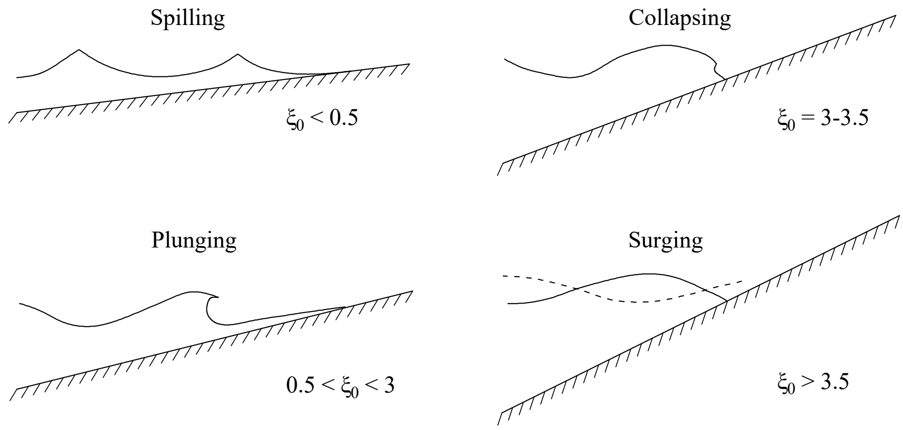

Figure 1.3. Observed types of wave breaking on an impermeable slope for a regular wave depending on the surf similarity parameter ξ_0. [USACE, 2002]

The type of wave breaking of the front slope of the breakwater can greatly influence the type of overtopping. Plunging waves create more of an impact when the wave breaks on the slope of the structure causing high energy dissipation and spray overtopping. The core permeability of the structure is expected to have little influence on the overtopping in regard to this type of wave breaking as more energy is dissipated on the slope than within the core. However, due to the low steepness of collapsing and surging waves, wave breaking is less likely to occur. Therefore, for a permeable slope, more wave energy is dissipating within the core and less energy transmitted over the structure, whereby the core permeability is expected to have a greater influence.

The geometrical influences and complex dynamics of wave breaking and porous flow makes overtopping prediction challenging. Nevertheless, research on the overtopping of rubble mound breakwaters has been performed to a great extent, to establish practical design formulae for overtopping predictions. Gaining information on this, allows for a more informative assessment of its limitations, paving the way for potential improvements.

1.2 Existing methods for prediction of wave overtopping

Coastal engineers are referred to the EurOtop [2018] manual for guidelines for the prediction of wave overtopping. The manual describes methods for determining the average overtopping discharge of coastal structures, such as breakwaters. The formulae are mainly based on empirical work from physical model tests. Formulae for determining the average overtopping discharge, by the mean value approach, for breaking ($\xi_{m-1,0} < 1.8$) and non-breaking ($\xi_{m-1,0} \geq 1.8$) waves on the slope are given in Eq. (1.1) and Eq. (1.2), respectively. [EurOtop, 2018, Eq. 5.10 and 5.11]

$$\frac{q}{\sqrt{gH_{m0}{}^3}} = \frac{0.023}{\sqrt{\tan(\alpha)}} \cdot \xi_{m-1,0} \cdot \exp\left[-\left(2.7\frac{R_c}{\xi_{m-1,0}H_{m0}\gamma_b\gamma_{f\ \mathrm{mod}}\gamma_\beta\gamma_v}\right)^{1.3}\right]C_r \tag{1.1}$$

with a maximum of

$$\frac{q}{\sqrt{gH_{m0}{}^3}} = 0.09 \cdot \exp\left[-\left(1.5\frac{R_c}{H_{m0}\gamma_{f\ \mathrm{mod}}\gamma_\beta}\right)^{1.3}\right]C_r \tag{1.2}$$

Where q is the average overtopping discharge per meter at the rear shoulder of the rubble mound, g is the gravitational acceleration, H_{m0} is the spectral significant wave height, γ_β includes the influence of wave obliquity, γ_b includes the influence of a berm, γ_v includes the influence of a vertical wall, C_r includes the influence of the crest width. $\gamma_{f\ \mathrm{mod}}$ includes the influence of roughness of the armour layer and the wave steepness given in Eq, (1.4) .

The crest width and roughness influence are provided in Eq. (1.3) [EurOtop, 2018, Eq. 6.8]. Eq. (1.3) is quite influential as it shows that a crest width G_c greater than $0.75H_{m0}$ results in an exponential reduction of the overtopping.

$$C_r = \min\left[3.06 \cdot \exp\left(-1.5\frac{G_c}{H_{m0}}\right),\quad 1\right] \tag{1.3}$$

where G_c is the crest width. The influence of roughness, $\gamma_{f,\mathrm{mod}}$ are provided in Eq. (1.4) [EurOtop, 2018, Eq. 6.7]

$$\gamma_{f\ \mathrm{mod}} = \begin{cases} \gamma_f, & \xi_{m-1,0} < 5 \\ \gamma_f + (\xi_{m-1,0} - 5)(1-\gamma_f)/5, & 5 < \xi_{m-1,0} < 10 \\ 1, & \xi_{m-1,0} > 10 \end{cases} \tag{1.4}$$

where γ_f is the influence factor for surface roughness, $\xi_{m-1,0} = \tan(\alpha)/\left(s_{m-1,0}\right)^{0.5}$ is the surf similarity parameter, α is the front slope angle, $s_{m-1,0} = H_{m0}/L_{m-1,0}$ is the wave steepness and $L_{m-1,0} = gT_{m-1,0}{}^2/(2\pi)$ is the spectral wavelength determined using the spectral wave period $T_{m-1,0}$. Initially $\gamma_{f,\mathrm{mod}}$ is constant, whereas it varies linearly in the range of $5 < \xi_{m-1,0} < 10$, as EurOtop [2018] deemed it wise to increase the influence of roughness for low wave steepness. For rubble mound breakwaters with a permeable core, the maximum value for $\gamma_{f\ \mathrm{mod}}$ is 0.60. [EurOtop, 2018]. Values for γ_f are selected based on the permeability and armour type of the breakwater design. Currently, for breakwaters with armour type of rocks, permeability in overtopping prediction is distinguished by a permeable and impermeable core and differentiated by armour unit type. Recommended values for γ_f are presented in Table 1.1. [EurOtop, 2018]

Table 1.1. Selected values for influence factor on roughness γ_f for permeable rubble mound structures with front slope 1:1.5. [EurOtop, 2018, Table 6.2]

Type of armour layer	γ_f [-]
Smooth impermeable surface	1.00
Rocks (1 layer, impermeable core)	0.60
Rocks (1 layer, permeable core)	0.45
Rocks (2 layers, impermeable core)	0.55
Rocks (2 layers, permeable core)	0.40

Using EurOtop [2018] the needed crest freeboard height R_c is calculated for an example, shown in Figure 1.4. The example is for a rubble mound breakwater with a front slope of 1:1.5 and a significant wave height of 5 m. Estimation of R_c is based on the mean value approach and all variables are assumed deterministic. Figure 1.4 evaluates R_c based on current recommended values for an impermeable ($\gamma_f = 0.55$) and permeable ($\gamma_f = 0.40$) core.

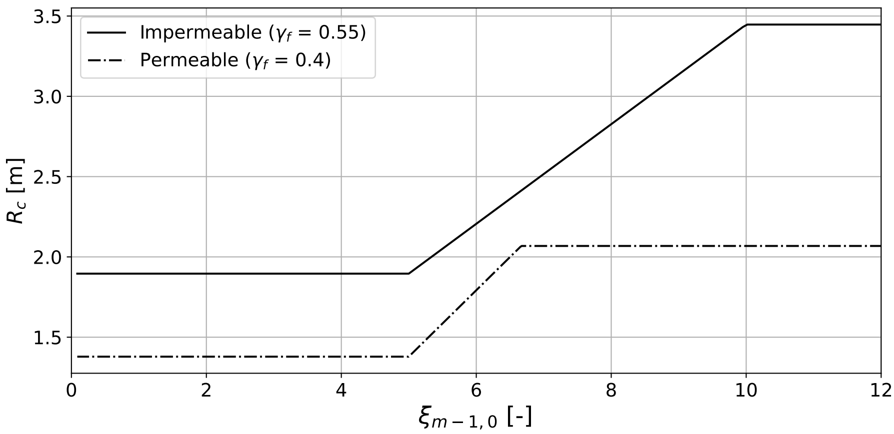

Figure 1.4. Required crest freeboard height R_c for design example. an average overtopping discharge of $q = 5$ l/s per m corresponding to a safe design for larger yachts with $H_{m0} = 5$ m. [EurOtop, 2018]

From Figure 1.4 a difference in crest freeboard height R_c of approximately 0.75 m is observed for low surf similarity parameters $\xi_{m-1,0} < 5$ (high wave steepness'). The difference in R_c significantly increases for $\xi_{m-1,0} > 7$ (low wave steepness') and the smallest difference is observed when $\xi_{m-1,0} \approx 7$. This is because $\gamma_{f,\mathrm{mod}}$ has an upper limit of 0.6 for a permeable core. Grounded in the potential savings in materials, more accurate guidelines for the permeability of the breakwater could prove beneficial for determining overtopping discharges.

Presently, limited knowledge exists for evaluating the influence of the permeability of rubble mound breakwaters, regarding wave overtopping. Current guidelines provide a rough distinction between a permeable and impermeable core with differentiation of the armour unit and layer thicknesses. [EurOtop, 2018]. By thoroughly examining the literature behind the current guidelines, one can establish a foundation for identifying the strengths and weaknesses of the guidelines, identifying potential research gaps

Literature review 2

This chapter seeks to investigate further, the current design guidance on wave overtopping prediction provided by EurOtop [2018], along with a comprehensive exploration of some of the literature that has shaped its development.

The primary prediction methods found in the manual are based on empirically fitted formulae where wave overtopping is specified as an average overtopping discharge q. Various influence factors, γ-values are used to include different wave parameters and geometrical influences of the breakwater layout. However, the influence factors are calibrated to certain breakwater geometries combined with specific wave parameters and are therefore governed by a range of validity, In regards to the influence of roughness, however, the variations of γ_f in Table 2.1 appear rather straightforward, as the value is only depended on the permeability of the core.

Table 2.1. Selected values for influence factor on roughness γ_f for permeable rubble mound structures with front slope 1:1.5. [EurOtop, 2018, Table 6.2]

Type of armour layer	γ_f [-]
Smooth impermeable surface	1.00
Rocks (1 layer, impermeable core)	*0.60*
Rocks (1 layer, permeable core)	*0.45*
Rocks (2 layers, impermeable core)	*0.55*
Rocks (2 layers, permeable core)	0.40

The recommended value of 0.40 from Table 2.1 are fitted values from a series of small-scale measurements of wave overtopping performed by Bruce et al. [2009]. Tests were performed on a cross-section with rock armoured slope of slope angle $\cot(\alpha) = 1.5$ and crest width $G_c = 3D_n$, where D_{n50} is the unit nominal diameter. The fitting of γ_f for the average overtopping discharge was done using Eq. (2.1). γ_f was assumed to include the effects of armour roughness and porosity. [Bruce et al., 2009, Eq. 5]

$$\frac{q}{\sqrt{g H_{m0}{}^3}} = 0.2 \exp\left(-2.6 \frac{R_c}{H_{m0}} \frac{1}{\gamma_f}\right) \tag{2.1}$$

From Eq. (2.1) no correction for the influence of the crest width G_c is included, why 0.40 should only be applied to structures with $G_c = 3D_n$ and $\cot(\alpha) = 1.5$, since only a slope of $\cot(\alpha) = 1.5$ with $G_c = 3D_n$ was tested. Wave overtopping was measured for wave heights repeated for three nominal wave steepness' of $s_{op} = 0.02$, 0.035 and 0.05 at two water depths $h = 0.186$ and 0.258 m with freeboard heights $R_c = 0.095$ and 0.134 m respectively.

Generated waves in Bruce et al. [2009] are based on a JONSWAP spectrum with peak enhancement factor $\gamma = 3.3$ and wave trains of 700-1300 waves. The smooth impermeable surface was modelled using a wooden plate where $G_c = 0\,\text{m}$. Two armour stone sizes of $D_{n50} = 0.042\,\text{m}$ and $D_{n50} = 0.030\,\text{m}$ with layer thickness $2D_{n50}$ were tested for the two layer rock armour with a permeable core. The cross-section for the permeable core was constructed with core material of $D_{n50} = 0.009\,\text{m}$ and a filter layer of unknown stone size but layer thickness $2D_{n50}$. However, the median stone mass $W_{50} = 7.42\,\text{g}$ is given for the filter layer and assuming a mass density $\rho = 2700\,\text{kg/m}^3$, yields a stone size of $D_{n50} = \sqrt[3]{W_{50}/\rho} \approx 0.014\,\text{m}$ [CIRIA et al., 2007].

A total of 14 tests were conducted for $D_{n50} = 0.042\,\text{m}$ and 15 tests for $D_{n50} = 0.030\,\text{m}$, results are shown in Figure 2.1. All values of γ_f are compared to tests of a smooth impermeable slope where data was found to fit quite well but fitting of γ_f yield 1.05. Therefore, all subsequent values of γ_f was reduced with 5 %. [Bruce et al., 2009]

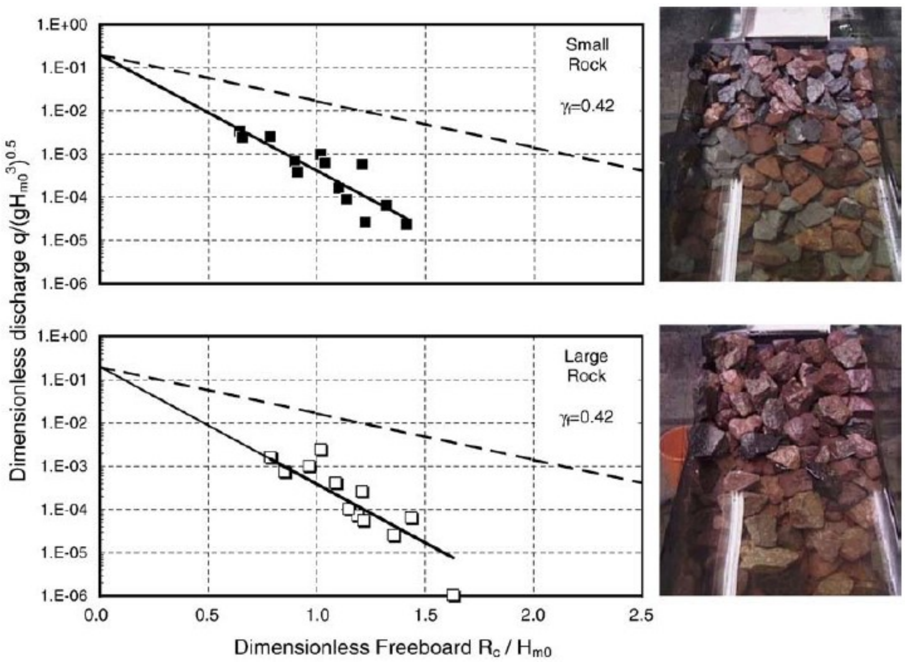

Figure 2.1. Results of tests for two layered rock armoured slopes with $\cot(\alpha) = 1.5$ for small rock ($D_{n50} = 0.030\,\text{m}$) and large rock ($D_{n50} = 0.042\,\text{m}$). Dashed lines are for $\gamma_f = 1$. [Bruce et al., 2009, Fig. 6]

Values for γ_f from Figure 2.1 are fitted to all tested wave steepness' of $s_{op} = 0.02$, 0.035 and 0.05. No great deviation is found for γ_f and similar results of $\gamma_f = 0.42$ are found for both rock armour sizes, small and large, shown in Figure 2.1. Bruce et al. [2009] established a confidence band from their own test data for two layered rock armoured permeable slopes with $\cot(\alpha) = 1.5$. The upper and lower 95 % confidence band were determined to be 0.43 and 0.37 respectively, with a mean value of 0.40.

A slope of $\cot(\alpha) = 2.0$ was also tested for a two layered rock armoured slope. This slope was however only tested using small armour stones of size $D_{n50} = 0.030\,\text{m}$. The results and fitting of γ_f are shown in Figure 2.2.

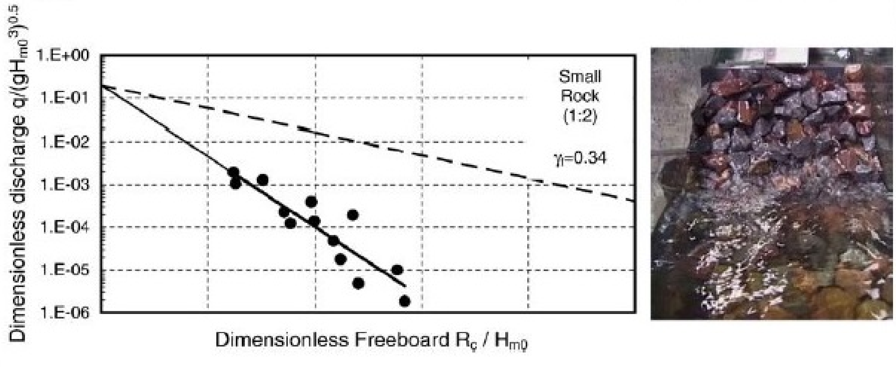

Figure 2.2. Results of tests for two layered rock armoured slopes with small rocks ($D_{n50} = 0.030\,\mathrm{m}$) and $\cot(\alpha) = 2.0$. Dashed lines are for $\gamma_f = 1$. [Bruce et al., 2009, Fig. 10]

A lower value of $\gamma_f = 0.34$ is found when fitting γ_f using Eq. (2.1) to data of $\cot(\alpha) = 2.0$ than with $\cot(\alpha) = 1.5$. Bruce et al. [2009] does not provide a confidence band for $\cot(\alpha) = 2.0$. However, Bruce et al. [2009] mentions that the 95 % confidence band of $\cot(\alpha) = 2.0$ is observed to be outside the confidence band of other tests. A variation with front slope angle was therefore observed but not further investigated. The variation of the slope was, however, later included in the expressions for $\gamma_{f,\mathrm{mod}}$ in EurOtop [2018].

Values in italic for γ_f in Table 2.1 are based on a series of small-scale model experiments of wave run-up on rubble mounds collected as part of the stability tests on rock slopes by Van der Meer [1988]. The 2 % wave run-up heights were measured for rock slopes with $\cot(\alpha) = 1.5$, 2, 3 and 4 with impermeable and permeable cores. γ_f-values were determined by the mean value approach for the wave run-up, given in Eq. (2.2) and Eq. (2.3) for breaking and non-breaking waves respectively. [EurOtop, 2007, Eq. 5.3]

$$\frac{R_{u2\%}}{H_{m0}} = 1.65 \cdot \gamma_b \cdot \gamma_f \cdot \gamma_\beta \cdot \xi_{m-1,0} \tag{2.2}$$

with a maximum of

$$\frac{R_{u2\%}}{H_{m0}} = 1.00 \cdot \gamma_b \cdot \gamma_{\text{f, surging}} \cdot \gamma_\beta \cdot \left(4 - \frac{1.5}{\sqrt{\xi_{m-1,0}}}\right) \tag{2.3}$$

where $R_{u2\%}$ is the run-up height exceeded by 2 % of the incident waves, and γ_b includes the influence of a berm. Van der Meer [1988] tested wave steepness' s_m in the range of 0.01-0.06 on two layer rock armoured slopes. Results of the relative run-up tests are shown in Figure 2.3.

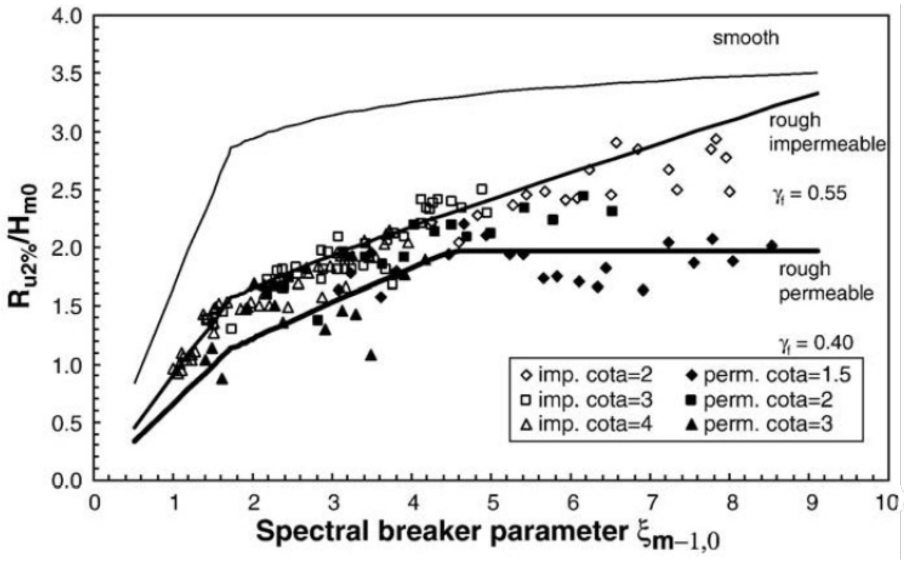

Figure 2.3. Relative run-up on straight rock slopes with permeable and impermeable core, compared to smooth impermeable slopes. Data is from Van der Meer [1988], while the graph is from Bruce et al. [2009].

The top curve in Figure 2.3 is the prediction of a smooth impermeable slope where $\gamma_f = 1$. A maximum for $\cot(\alpha) = 1.5$ where the relative run-up $R_{u2\%}/H_{m0} = 1.97$ is reached for the permeable core at $\xi_{m-1,0} \approx 4.9$. For two layers of rock armour with an impermeable core γ is fitted to a value of 0.55, or a permeable core this reduces to 0.40. Data points in Figure 2.3 are sporadic but the data seems to be grouped when $\xi_{m-1,0} < 5$ (high steepness waves) and the difference in the data becomes more apparent for $\xi_{m-1,0} > 5$ (low steepness waves). For larger values of $\xi_{m-1,0}$ the impermeable core approaches the smooth impermeable dashed line. The reason for this could be that the surging wave fills the pores of the armour layer and thereby approaches a smooth surface. The influence of the roughness γ_f for non-breaking waves ($\xi_{m-1,0} > 1.8$) on the relative run-up $R_{u2\%}/H_{m0}$ is accounted for by $\gamma_{\text{f, surging}}$ provided in Eq. (2.4). [EurOtop, 2007, Eq. 6.1]

$$\gamma_{\text{f, surging}} = \begin{cases} \gamma_f + (\xi_{m-1,0} - 1.8)(1 - \gamma_f)/8.2, & 1.8 < \xi_{m-1,0} < 10 \\ 1, & \xi_{m-1,0} > 10 \end{cases} \tag{2.4}$$

γ_f-values of 0.55 and 0.40 show good agreement with wave run-up data and $\gamma = 0.40$ is also backed by a number of wave overtopping data, for example the work by Bruce et al. [2009].

2.1 Rock armour stability

Van der Meer [1988] established stability formulae for rock armoured rubble mound breakwaters based on different layer compositions and mainly deep water wave conditions. Furthermore, the stability formulae are derived for two layered rock armoured slopes. The stability of statically stable non-overtopped rock armoured breakwaters is given for plunging and surging waves in Eq. (2.5) and Eq. (2.6) respectively [Van der Meer, 1988, Eq. 3.23 and 3.24].

Plunging waves ($\xi_{0m} < \xi_{m,cr}$ or $\cot(\alpha) \geq 4$)

$$\frac{H_s}{\Delta D_{n50}} = 6.2 \cdot P^{0.18} \cdot \left(\frac{S_d}{\sqrt{N}}\right)^{0.2} \cdot \xi_{0m}{}^{-0.5} \tag{2.5}$$

Surging waves ($\xi_{0m} \geq \xi_{m,cr}$ or $\cot(\alpha) < 4$)

$$\frac{H_s}{\Delta D_{n50}} = 1.0 \cdot P^{-0.13} \cdot \left(\frac{S_d}{\sqrt{N}}\right)^{0.2} \cdot \sqrt{\cot(\alpha)} \cdot \xi_{0m}{}^{P} \tag{2.6}$$

Where H_s is the significant wave height from the time domain (average of 1/3 highest wave heights), $\Delta = \rho_{armour}/\rho_{water} - 1$ is the relative mass density, D_{n50} is the nominal stone diameter, P is the notional permeability factor, S_d is the damage level, N is the number of waves, α is the front slope angle, ξ_{0m} is the surf similarity parameter based on the mean wave period T_m and deep water wavelengths. T_m is preferred for describing static stability as the influence of the spectral shape becomes neglectable. The shift from plunging to surging waves is given as the intersection of both formulae and expressed as $\xi_{m,cr}$ provided in Eq. (2.7). [Van der Meer, 1988, Eq. 3.25]

$$\xi_{m,cr} = \left(6.2 \cdot P^{0.31} \cdot \sqrt{\tan(\alpha)}\right)^{\frac{1}{P+0.5}} \tag{2.7}$$

Van der Meer [1988] tested three layer compositions with different notional permeability factors P giving some indication of the range and value of P. The notional permeability factor is lowest for a structure consisting of an impermeable core with a 2-layered armour layer separated by a thin filter layer ($P = 0.1$) and largest for a homogeneous structure ($P = 0.6$). However, the selection of P was still left to the judgement of the engineer.

The notional permeability factor P was introduced to include the permeability of the structure but has no physical meaning. Nonetheless, Eldrup et al. [2019] established an empirical formula to estimate P for new layer compositions. The formula is based on model tests of seven layer compositions, where two are replicated from Van der Meer [1988]. The new method for determining P is described in Appendix A.

2.2 State of the art for wave overtopping prediction

A modified version for overtopping prediction for non-breaking waves Eq. (1.2) was proposed in Eldrup et al. [2022]. The modified version was calibrated to a large dataset to enlarge the area of applicability through a new crest width influence factor γ_{cw} and improvement of $\gamma_{f\ \mathrm{mod}}$ termed γ_{fS}. Eldrup et al. [2022] dataset consists of 888 tests covering a range of relative crest width G_c/H_{m0} = 0.00-5.18, front slope angles $\cot(\alpha)$ = 1.5-4 and wave steepness' $s_{m-1,0}$ = 0.005-0.062 and a variety of different armour types. The study by Eldrup et al. [2022] was only based on non-breaking waves ($\xi_{m-1,0} > 1.8$). Nevertheless, part of the available data contained tests from structures within the breaking waves domain with slope angle $\cot(\alpha) = 4$. The updated formula for non-breaking waves is provided in Eq. (2.8). [Eldrup et al., 2022, Eq. 5]

$$\frac{q}{\sqrt{gH_{m0}{}^3}} = 0.09 \cdot \exp\left[-\left(1.5\frac{R_c}{H_{m0}\gamma_{fS}\gamma_{cw}\gamma_\beta}\right)^{1.3}\right] \tag{2.8}$$

The crest width influence is accounted for through γ_{cw} on the relative freeboard R_c/H_{m0} instead of directly influencing q through C_r. The new influence factor γ_{cw} is provided in Eq. (2.9). [Eldrup et al., 2022, Eq. 6]

$$\gamma_{cw} = \min\left[1.1 \cdot \exp\left(-0.18\frac{G_c}{H_{m0}}\right), \quad 1\right] \tag{2.9}$$

Moreover, the roughness influence factor was improved when treating the front slope angle α and wave steepness $s_{m-1,0}$ separately, as the wave steepness was found much more influential for wave overtopping on breakwaters with steep slopes (non-breaking waves). The data for various rock armoured slopes were fitted using the power function in Eq. (2.10).

$$\gamma_{fS} = 0.05(s_{m-1,0})^{-0.5} + b \tag{2.10}$$

Here b was taken as a function of the slope angle $\cot(\alpha)$ and fitted to each slope angle in the dataset, regardless of the permeability of the structure. Figure 2.4 shows the fitted curves for each slope angle and the fitted power function. The Mean Absolute Percentage Error (MAPE) was used to judge the goodness of the fit.

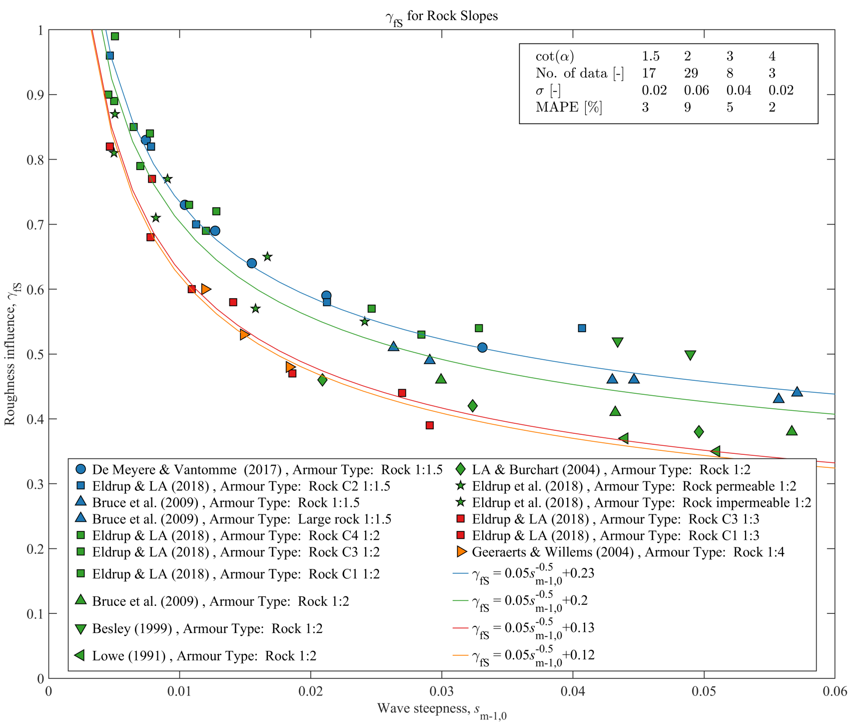

Figure 2.4. Influence of wave steepness $s_{m-1,0}$ on γ_{fS} for various slope angles and all data sets for rock armour. [Eldrup et al., 2022, Fig. 14]

Figure 2.4 shows that the b-coefficient shifts the curves parallel to the y-axis, in relation to the slope of the breakwater. What may also be noticed is that only a very limited amount of data points is from structures with an impermeable core. For data from rock armoured slopes of $\cot(\alpha) = 1.5$ (blue Δ) an average value of $\gamma_{fS} = 0.45$ was found for large waves steepness', where the influence of the waves steepness becomes negligible and γ_{fS} approaches a constant value. Nevertheless, an influence of the slope angle $\cot(\alpha)$ is apparent and b was assumed to mainly depend on the slope angle $\cot(\alpha)$ for a rock slope as shown in Eq. (2.11). [Eldrup et al., 2022]

$$b = 0.34 - 0.07 \cdot \min[\cot(\alpha), 3] \tag{2.11}$$

Data provided in Figure 2.4 is fitted for rock armoured slopes. However, Eldrup et al. [2022] also investigated the influence of different armour types. The dataset included amour units of type rock, Haro, Acropode, a smooth surface and more. The influence of the armour type was found by assuming that 0.34 in Eq. (2.11) varies with the armour unit type. The final influence of the armour type incorporates γ_f to describe the influence of the armour type, where the constant 0.09 is an offset of the γ_f from EurOtop [2018]. The new roughness factor γ_{fS} is provided in Eq. (2.12). [Eldrup et al., 2022, Eq. 12]

$$\gamma_{fS} = \min\left[\gamma_f + 0.05 \cdot (s_{m-1,0})^{-0.5} - 0.07 \cdot \min\left[\cot(\alpha), 3\right] - 0.09,\ \ 1\right] \tag{2.12}$$

To show the differences in evaluation of the roughness influence of $\gamma_{f\text{mod}}$ by EurOtop [2018] and γ_{fS} by Eldrup et al. [2022] the example of the needed freeboard height R_c in Figure 1.4 is reformulated to the method by Eldrup et al. [2022], shown in Figure 2.5.

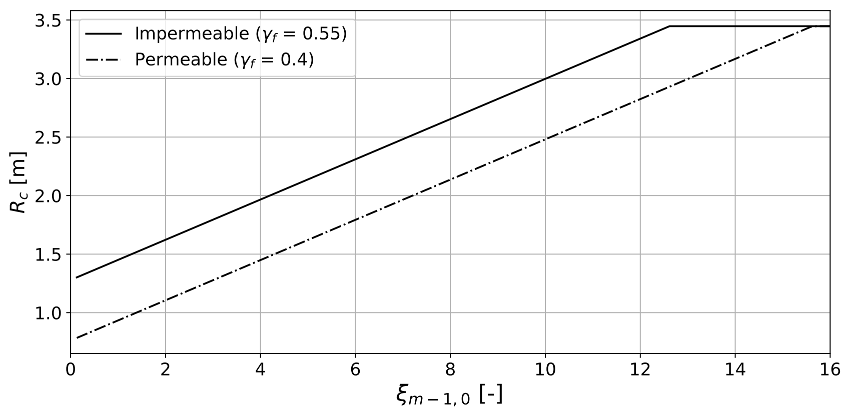

Figure 2.5. Required crest freeboard height R_c for design example. an average overtopping discharge of $q = 5\,\text{l/s}$ per m corresponding to a safe design for larger yachts with $H_{m0} = 5\,\text{m}$. [Eldrup et al., 2022]

A significant improvement was found when comparing EurOtop [2018] in Eq. (1.2) and Eq. (2.8) for the overtopping prediction. The improvement can be illustrated by the use of Figure 2.5, where the difference in R_c went from 0.75 m and varying in Figure 1.4 to a constant of 0.50 m. Therefore, Eq. (2.8) by Eldrup et al. [2022] will henceforth be used for overtopping prediction.

Summary

Even though an improvement was made by Eldrup et al. [2022], Figure 2.5 still highlights the significance of design decisions in breakwater projects and the need for careful consideration when choosing between permeable and impermeable structures. The choice of core type in a breakwater design can significantly impacts the freeboard height of the structure, for example, by 0.5 meters. Designing for wave overtopping rates requires a distinct choice between permeable and impermeable structure, as the current guidelines offers no middle ground, typically represented by a γ_f value of either 0.40 or 0.55, respectively. However, when it comes to stability design, the permeability of a breakwater is more nuanced, as the notional permeability factor, P can encompass various permeability descriptions.

The current understanding of wave overtopping and the associated values of γ_f primarily comes from studies focused on structures with permeable cores, as documented in the work by Bruce et al. [2009]. On the other hand, the recommendation for the γ_f value for structures with impermeable cores, as provided in EurOtop [2018], was derived from the data of Van der Meer [1988], which primarily addressed wave run-up rather than wave overtopping, as indicated in Figure 2.3. These observations emphasise the need for further investigation into the permeability and roughness of structures, when designing for wave overtopping rates.

Through intense experimental work, data will be collected, covering a wide range of wave steepness and roughness influence factors, as done in many of the mentioned literature. This will be accomplished by testing a range of different structures with different permeability. These investigations, will potentially contribute to more knowledge regarding the impacts of permeability and roughness on wave overtopping, providing the engineer with a better basis for design decisions during the project design.

Experiment 3

A series of small-scale model tests have been performed in order to map the influence of permeability on the average overtopping discharge. The test program covers a range of different sea states, water levels and layer compositions with permeable and impermeable cores. Henceforth, the permeability of a breakwater will be described with the specific P-value. The empirical results of the tests are also used as supplements and later evaluated against a computational fluid model. The numerical model requires the specification of porosity parameters, to describe the hydraulic resistance within the breakwater. These porosity parameters are found by physical model experiments and are included in this chapter.

3.1 Experimental setup

All physical model tests of wave overtopping were performed in a wave flume with a horizontal bottom of dimensions $25.0\,\text{m} \times 1.5\,\text{m} \times 1.0\,\text{m}$ (l × w × h) at Aalborg University. Generated waves propagated perpendicular to the model and 11 wave gauges measured the surface elevation. One wave gauges array of four wave gauges was placed near the wavemaker for validation of the wave generation in the numerical model. Another array was placed near the breakwater to separate incident and reflected waves. The experimental setup in the wave flume is sketched in Figure 3.1, along with the position of the model and installed wave gauges.

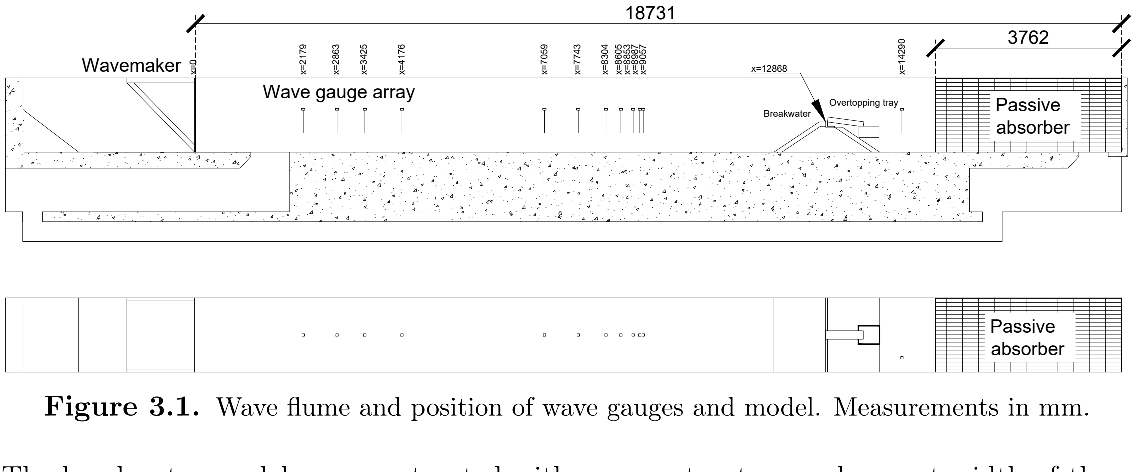

Figure 3.1. Wave flume and position of wave gauges and model. Measurements in mm.

The breakwater model was constructed with a superstructure and a crest width of three 3 times the nominal diameter of the armour rocks D_{n50A}. The superstructure was placed the same distance from the wavemaker in all tests, as shown in Figure 3.1. The breakwater model was constructed with two front slopes of 1:1.5 and 1:3 with the toe placed 11.758 m and 10.860 m from the wavemaker, respectively. Two water levels of 0.480 m and 0.522 m were used in the test series. Overtopping was measured as the amount of water passing over the crest of the superstructure. Breakwater models were constructed such that most of the structural elements remained in the same position throughout each test campaign. The aspiration was to have the layer composition i.e. the permeability, as the only variation in each test. The cross-section of the breakwater model with $\cot(\alpha) = 1.5$ and $\cot(\alpha) = 3.0$ is shown in Figure 3.2 with the definition of water depth h, freeboard height R_c, crest width $G_c = 3D_{n50A}$ and slope angle α.

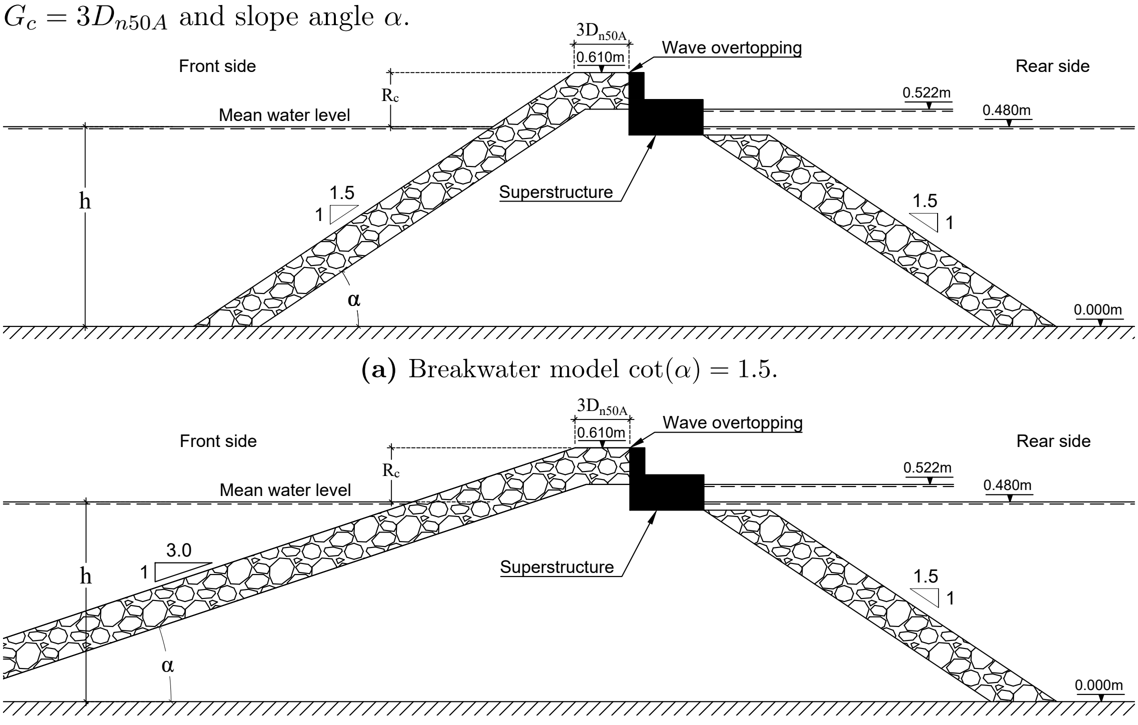

(a) Breakwater model $\cot(\alpha) = 1.5$.

(b) Breakwater model $\cot(\alpha) = 3.0$.

Figure 3.2. Geometry of the breakwater model with tested water depths $h = 0.480$ m and 0.522 m.

Figure 3.3 shows the setup of the measuring equipment for the model measurements. The overtopping discharge was measured with an overtopping tray of 0.3 m width, leading the water into a tank, containing a wave gauge and a pump. The wave gauge measured the change in water level and the pump would empty the tank when the water reached a certain level. Lastly, a wave gauge was installed to measure wave transmission on the rear side, along with a plate, preventing any disturbance from the pump action.

(a) Front view of model setup. **(b)** Side view of model setup.

Figure 3.3. Test setup of the measurement equipment used in the wave flume.

Significant overtopping scale effects are only expected to occur for fairly low overtopping discharges [Lykke Andersen, 2006]. The limit of overtopping measurements is set to $q/(gH_{m0}{}^3)^{0.5} = 10^{-6}$, regarded as zero overtopping in the model tests, according to EurOtop [2018]. Wave parameters and water levels were chosen so that target values of the overtopping discharge were above this limit. Additionally, excessive overtopping was unwanted to avoid flooding the tank and preventing unacceptable damage to the model. Unacceptable damage was judged as a change in cross-section, great enough to influence the overtopping and evaluated through visual inspection.

The average overtopping discharge q is derived from the tank signal by correcting the signal for the pump action. An example of the measured overtopping signal is shown in Figure 3.4.

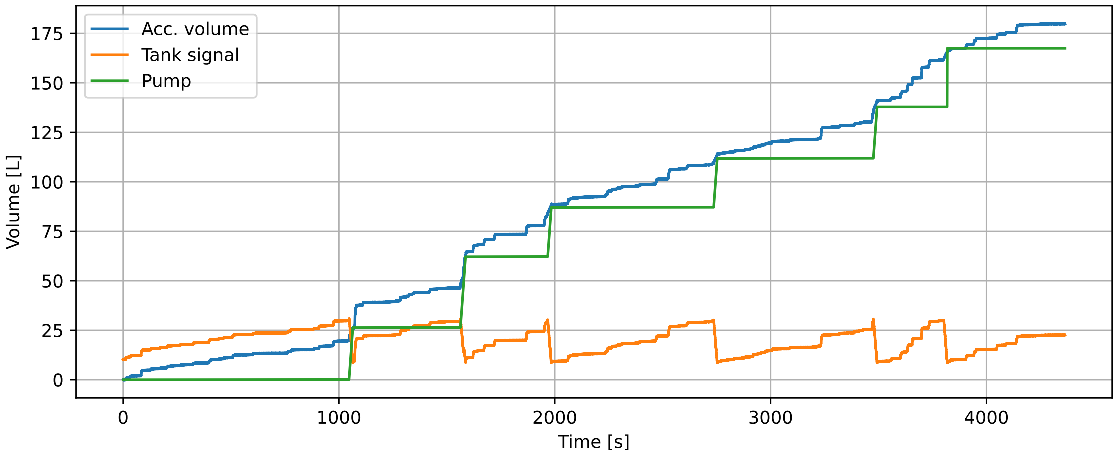

Figure 3.4. Example of overtopping signal for an arbitrary test.

The total volume overtopping the model varies significantly in each test, ranging from the lowest of 1.26 L to a maximum of 2084 L. The average overtopping discharge was determined from wave trains consisting of about 2000 waves for each test.

3.1.1 Breakwater layer composition

Five different rock materials ranked class I to V, were used to create the layer compositions used in the model tests. The material properties of these rocks are listed in Table 3.1. Coefficient d and f are laminar and turbulent coefficients derived from empirical data for the Darcy-fochheimer relation, further described in appendix C.

Table 3.1. Material properties of rock materials used for layer compositions.

	Median weight	Nominal diameter	Grading	Mass density	Darcy coef.	Forchheimer coef.	Porosity
Rock class	W_{n50} [g]	D_{n50} [m]	D_{n85}/D_{n15} [-]	ρ [kg/m^3]	d [1/m^2]	f [1/m]	n [-]
I	221.00	0.044	1.296	2620	4.02×10^6	239.61	0.43
II	30.00	0.022	1.115	2658	6.57×10^6	737.01	0.43
III	9.00	0.015	1.357	2768	7.23×10^6	983.11	0.43
IV	5.15	0.012	1.298	2713	8.70×10^6	1428.70	0.41
V	0.65	0.006	1.360	2936	23.03×10^6	2631.93	0.39

For each layer composition, the notional permeability factor P has been determined using the method by Eldrup et al. [2019], further described in Appendix A. Sketches of the different layer compositions used in the model tests are shown in Figure 3.5, with their estimated P-value. Note that the outer armour layer is the same throughout every composition and $P = 0.1$ and 0.5, has been tested with a slope of $\cot(\alpha) = 1.5$ and 3.0.

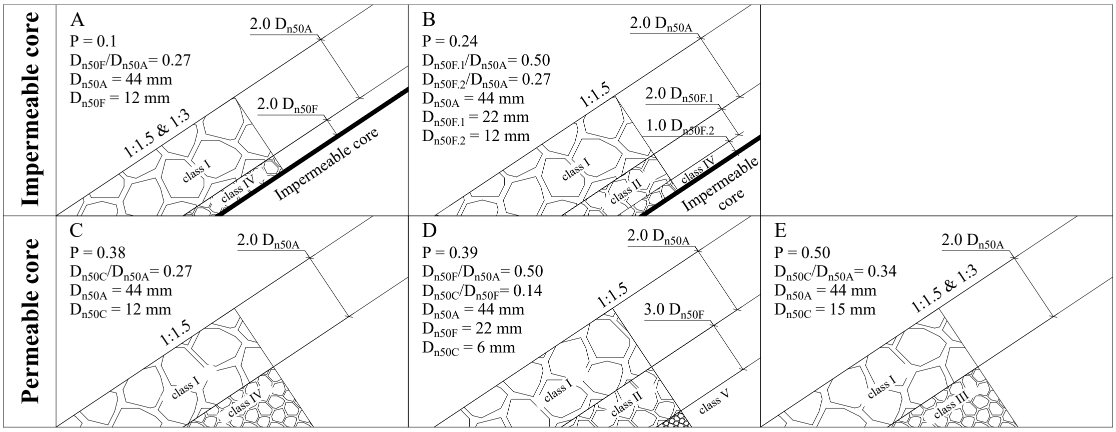

Figure 3.5. Tested layer compositions.

The side view for each model is shown in Figure 3.6.

(a) $P = 0.10$, $\cot(\alpha) = 1.5$.

(b) $P = 0.24$, $\cot(\alpha) = 1.5$.

(c) $P = 0.38$, $\cot(\alpha) = 1.5$.

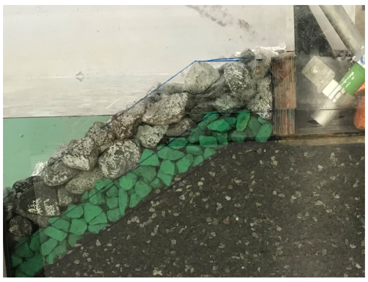

(d) $P = 0.39$, $\cot(\alpha) = 1.5$.

(e) $P = 0.50$, $\cot(\alpha) = 1.5$.

Figure 3.6. Side view of each tested model.

The rear side of the model was constructed with a slope of 1:1.5, and an armour layer consisting of stones with a nominal diameter of $D_{n50} = 0.054\,\text{m}$. When needed, appropriate filter stones were used, to prevent the core material from outwashing, see Figure 3.7.

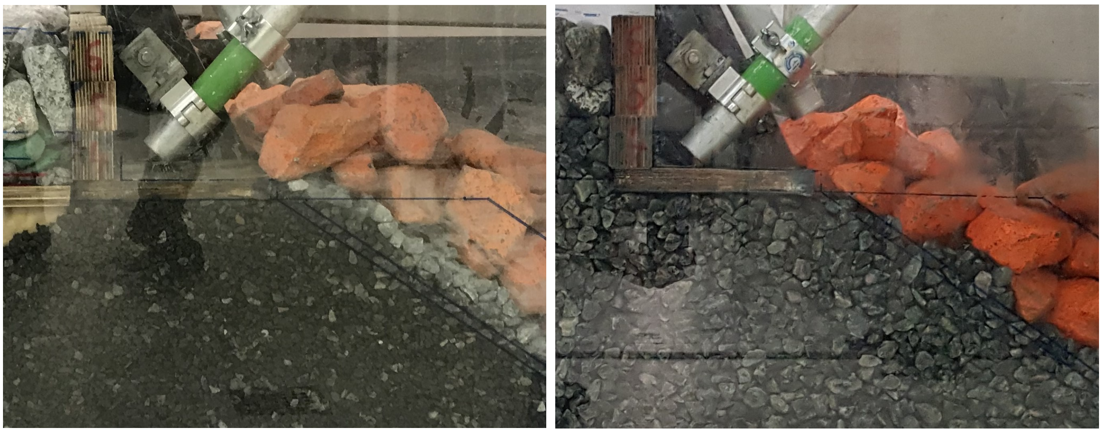

(a) Rear side with a filter layer. **(b)** Rear side without a filter layer.

Figure 3.7. Sideview of the rear side, with- and without a filter layer.

3.1.2 Wave generation and wave analysis

The piston wavemaker generates the waves trains by use of the software package AwaSys 7 by Aalborg University [2023a]. AwaSys 7 is capable of producing both regular- and irregular wave trains, using the methods described in Eldrup and Lykke Andersen [2019b]. The wave generation includes active wave absorption, based on wave gauges installed at the paddle face using the Lykke Andersen et al. [2016] method. For calibration and validation of the numerical model, regular waves series were produced using approximate stream function theory. The irregular wave trains were produced using a theoretical JONSWAP spectrum, with a peak enhancement factor $\gamma = 3.3$ and a target number of 2000 waves. The wavemaker theory followed the second. order wavemaker theory by Schäffer [1996], when the respective seastate was in the validity range, S<2.0, following the studies of Eldrup and Lykke Andersen [2019b], where S is the nonlinearity parameter. When outside the validity range, the ad-hoc unified wavemaker theory of Zhang et al. [2007] was used.

To separate the incident and reflected wave trains, an array of seven resistant type wave gauges was used with individual distances of 0.69, 1.24, 1.55, 1.79, 1.93 and 2.00 m. The analysis was conducted using the software package WaveLab 3 by Aalborg University [2023b], using the nonlinear method by Eldrup and Lykke Andersen [2019a]. Previous experience from the wave flume shows that multiple consecutive test campaigns can result in a build-up of dirt and limescale on the installed wave gauges. To prevent any significant source of error regarding this, each wave gauge was cleaned and calibrated before and after every test campaign.

3.2 Test campaign and parameter ranges

A total of 495 separate tests were performed in the flume. In general, these tests were split into separate test campaigns with 18 different sea states in each campaign. The main goal for the test campaigns was to cover a range of different wave steepness, relative freeboards and overtopping discharges. One test campaign consisted of one water level, three wave heights and six wave steepness' for each wave height. The determination of tested wave steepness was based on the literature study in chapter 2. The target range of wave steepness spanned from 5‰to 45‰, somewhat covering the same range of data as in Figure 2.4. The six specific target wave steepness values is: 5, 7, 10, 20, 30 and 45‰, covering the presumed steep and flat part of Figure 2.4.

The order of the tests in a campaign was designed to prevent unacceptable damage to the model early in the campaign. This was ensured by starting with the smallest wave height and selecting the initial wave steepness based on the model tested according to the stability formulae by Van der Meer [1988]. For the models with a permeable core, the initial test would be of the smallest wave height and the lowest wave steepness, followed by the same wave height with a higher wave steepness until all six steepness would be tested for that wave height. Then follows the second wave height, with the same order of wave steepness. If the model was with an impermeable core, the initial test would be of the smallest wave height and highest wave steepness. The parameter ranges for all the tested layer compositions are shown in Table 3.2.

Table 3.2. Parameter ranges for the 495 performed tests. The definitions of the layer composition (LC) are shown in Figure 3.5.

LC	P	n [-]	cot(α) [-]	G_c/H_{m0} [-]	R_c/H_{m0} [-]	h/H_{m0} [-]	$s_{m-1,0}$ [‰]	$\xi_{m-1,0}$ [-]
A	0.10	140	1.5	1.26 - 2.31	0.86 - 1.70	4.58 - 9.11	4.72 - 50.07	2.98 - 9.71
A	0.10	79	3.0	0.92 - 2.30	0.69 - 1.53	3.35 - 9.09	4.95 - 51.05	1.48 - 4.74
B	0.24	36	1.5	1.28 - 2.29	0.87 - 1.71	4.66 - 9.04	4.79 - 50.24	2.97 - 9.63
C	0.38	36	1.5	1.07 - 2.30	0.87 - 1.54	3.88 - 9.09	5.16 - 49.32	3.00 - 9.28
D	0.39	36	1.5	1.07 - 2.31	0.86 - 1.55	3.90 - 9.13	4.89 - 50.11	2.98 - 9.53
E	0.50	126	1.5	1.07 - 2.30	0.89 - 1.55	3.89 - 9.08	4.97 - 49.98	2.99 - 9.45
E	0.50	42	3.0	1.09 - 1.69	0.81 - 1.54	3.95 - 6.69	4.76 - 50.11	1.49 - 4.83

As Table 3.2 shows, most tests were conducted on model $P = 0.10$ and $P = 0.50$ to estimate the spreading of the measured overtopping for a permeable and impermeable structure. In order to create disparity, the armour layer was rearranged in five separate tests for $\cot(\alpha) = 1.5$ and two for $\cot(\alpha) = 3.0$ with $h = 0.522\,\text{m}$, in order to study repeatability and spreading caused by armour replacement.

Before analysing the data from the tests, potential outliers or invalid data, have to be identified and excluded from further investigation. One data point was excluded from further analysis, as it was deemed an outlier and invalid. This is later shown in Figure 3.10, as the permeable test, with a relative freeboard at $R_c/(H_{m0}\gamma_{cw}\gamma_{fS}) \approx 5.6$.

Even though the test campaigns were designed to produce a sufficient amount of overtopping, some tests may have had an insufficient amount $(q/(gH_{m0}{}^3)^{0.5} > 10^{-6})$.

To eliminate such tests, a minimum requirement of $q/(gH_{m0}{}^3)^{0.5} = 10^{-6}$ is applied before a data point can be carried further to data analysis. In total, three tests were eliminated due to this threshold.

As this threshold only corresponds to a small amount of overtopping, visual inspection during testing revealed rapid repetition of large amounts of overtopping. This caused the overtopping tray to overflow and any extra amounts of overtopping would as a consequence not be measured. During a total amount of 30 tests the overtopping tray was full, 1-3 times during testing. Even though this is a source of error in the measured data, tests that have had a full overtopping box, also had a total amount of 1000-2000 L measured overtopping. Consequently, the tests will not be eliminated, since the amount of lost overtopping is estimated not to have had any significant impact on the final result. The test which resulted in a full overtopping tray is indicated with arrows in Figure 3.9.

The tests were designed to prevent excessive damage ($S_d > 8$) to the model. After every test campaign the damage to the model was assessed by visual inspection and any damage was repaired before running the next test or test campaign. If the damage was deemed unacceptable, meaning either the filter layer was exposed or the cross-section of the model was significantly altered, the model was repaired and the respective test was repeated. Damage was observed after most test campaigns however, the change in cross-section was regarded as acceptable ($S_d < 8$) in most cases. Figure 3.8 shows a visual inspection of a model before and after a test campaign ($\approx$ 32000 waves).

(a) Before test campaign. **(b)** After test campaign.

Figure 3.8. Damage inspection on layer composition $P = 0.50$. The performed test campaign features a water depth 0.522 m, six wave steepness' between 5-45‰ and three wave heights of 0.06, 0.08 and 0.10 m

All test results for each layer composition are shown in Figure 3.9. Note that all the data points are only corrected by the influence of the crest width γ_{cw} from (2.9).

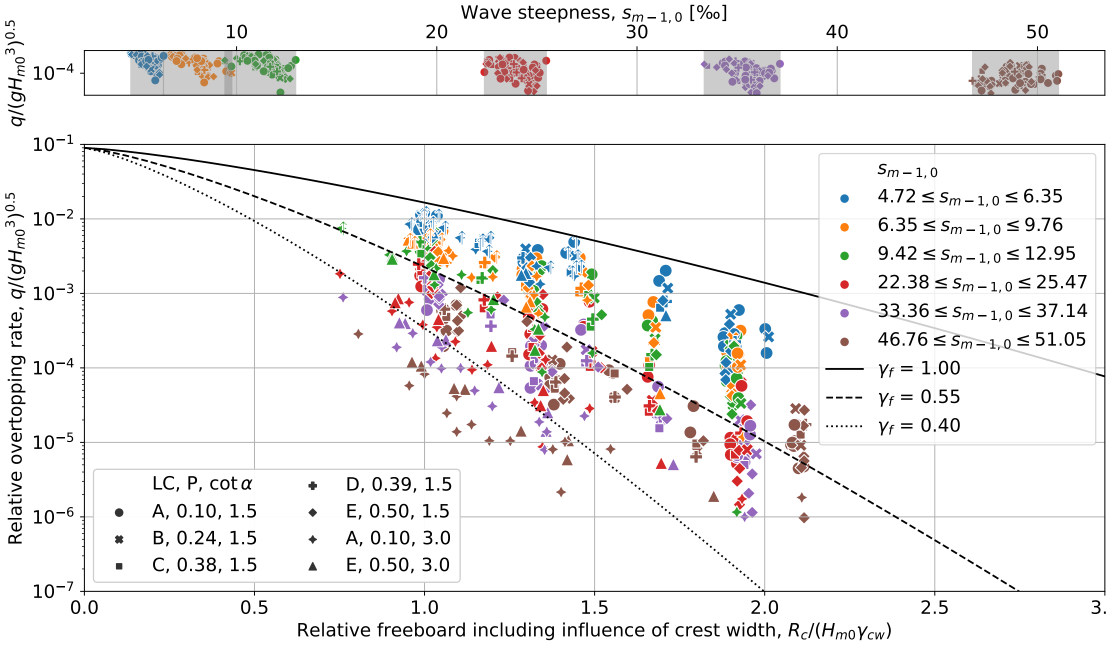

Figure 3.9. Overtopping data for all tests. Arrows indicate data points where the overtopping tray was filled to overflowing.

The results for the performed test are compared to Eq. (2.8) by Eldrup et al. [2022], along with the 90 % confidence band from EurOtop [2018] in Figure 3.10. Giving that the lower wave steepness' results in significantly more measured overtopping, the results are corrected, using the influence of roughness of the armour layer γ_{fS} Eq. (2.12) by Eldrup et al. [2022].

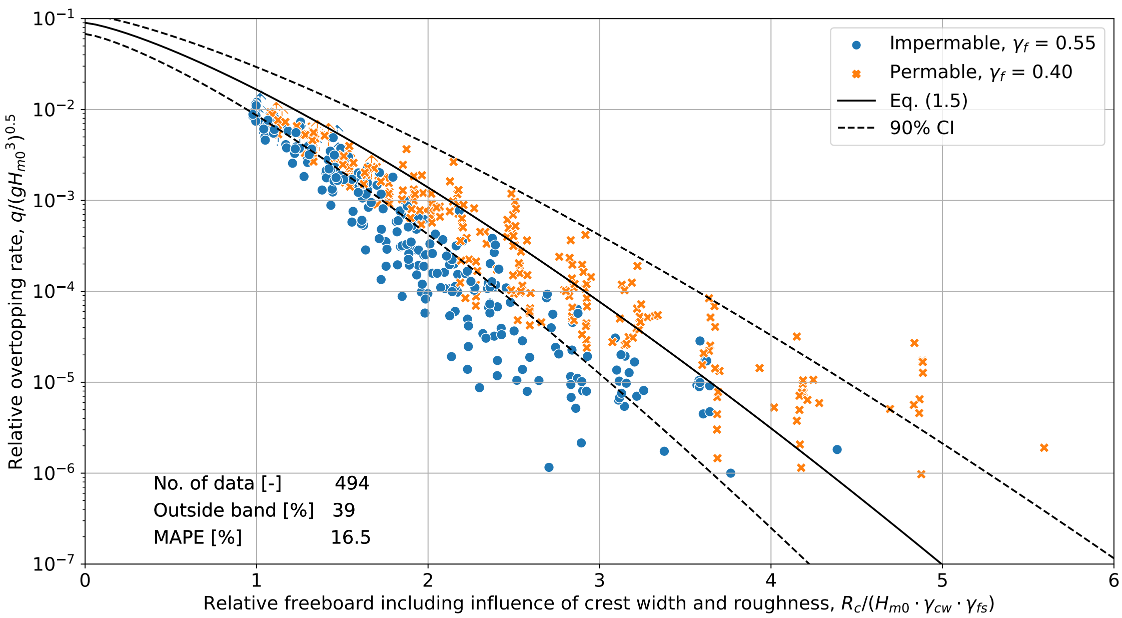

Figure 3.10. Overtopping data and non-breaking formula in (2.8), seperated by core type. Arrows indicate data points, in which the overtopping tray was filled to overflowing.

Figure 3.10 shows a clear distinction between an impermeable and permeable core and most of the impermeable cores lie outside and in the lower limit of the 90% confidence band, which could indicate an overestimation of the predicted overtopping discharge, based on the influence of roughness. This may be further investigated in the following data analysis.

3.3 Data analysis

Initially, a preliminary investigation was undertaken to examine the primary uncertainties inherent in the data analysis. This study specifically focused on assessing the uncertainties associated with two key parameters: the significant wave height, H_{m0}, and the freeboard, R_c, as well as their potential impact on the data analysis and ultimate conclusions. Detailed information on this investigation can be found in Appendix D. The study concluded that the uncertainties surrounding H_{m0} and R_c are not anticipated to exert a substantial influence on the final conclusions drawn from the present data analysis. However, it remains vital to acknowledge and duly consider these uncertainties.

The results from the performed test are shown in Figure 3.11, separating the data set in each P-value. The data points are corrected using γ_{cw} and γ_{fS} by Eldrup et al. [2022]. Solid markers indicates impermeable cores, with a $\gamma_f = 0.55$ and open markers indicates permeable cores, $\gamma_f = 0.40$

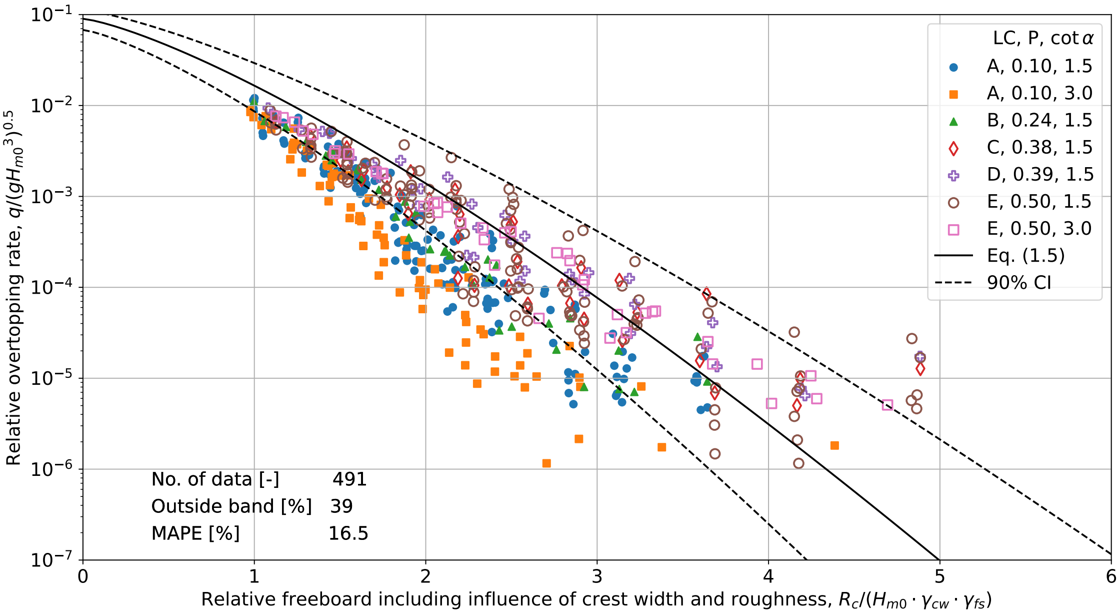

Figure 3.11. Overtopping data and non-breaking formula in Eq. (2.8). Solid markers indicates impermeable cores, with a $\gamma_f = 0.55$ and open markers indicates permeable cores, $\gamma_f = 0.40$.

Figure 3.11 suggest that it might be advantageous to separate the influence of roughness based on the individual P-value instead of solely on permeable and impermeable cores. In the remaining data analysis, the influence of roughness and permeability is referred to as γ_{P*}. The fitting of γ_{P*} was performed separately for each notional permeability factor P and slope $\cot(\alpha)$ and the data was grouped on wave steepness $s_{m-1,0}$. The lowest Mean

Absolute Percentage Error (MAPE) was chosen as the fitting method for γ_{P*}. The fitting equation follows the method by Eldrup et al. [2022] and is provided in Eq. (3.1).

$$\frac{q}{\sqrt{gH_{m0}^3}} = 0.09 \cdot \exp\left[-\left(1.5\frac{R_c}{H_{m0}\gamma_{cw}} \cdot \frac{1}{\gamma_{P*}}\right)^{1.3}\right] \tag{3.1}$$

where γ_{P*} is the only unknown variable, since γ_{cw} is calculated by Eq. (2.9). The principle of fitting γ_{P*} for each group of wave steepness and P-value, is shown in Figure 3.12. Figure 3.12 shows the results for one test campaign for $P = 0.10$ and $\cot(\alpha) = 1.5$, $h = 0.522$ m. The remaining fits for every test campaign are available in appendix B.

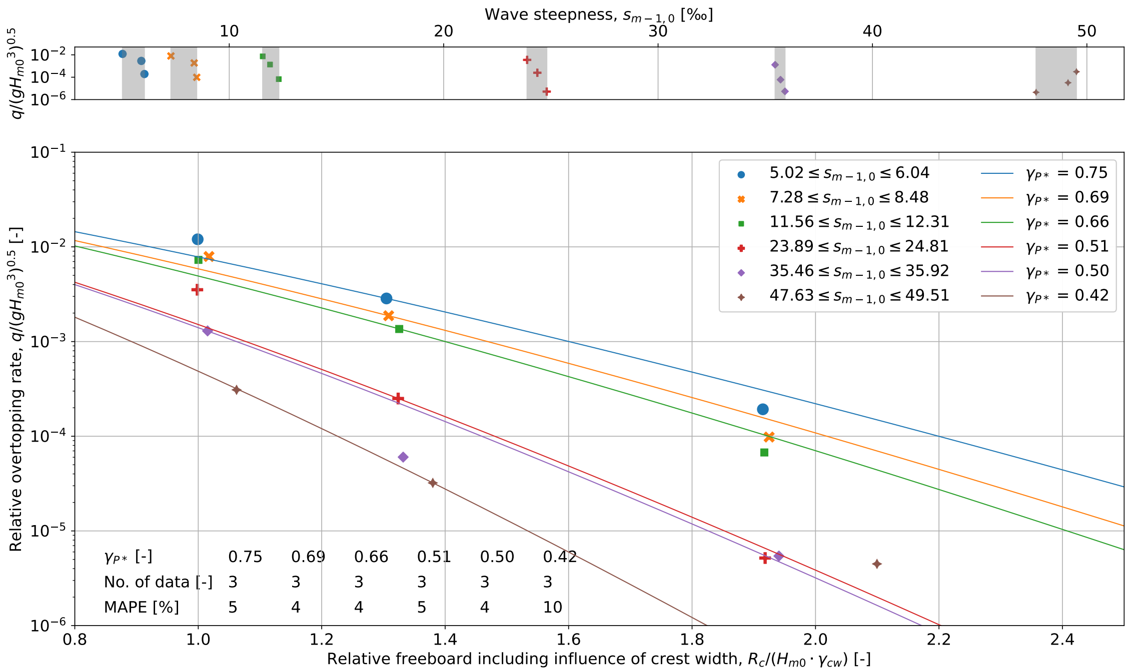

Figure 3.12. Fitting of influence factor γ_{P*} for $P = 0.10$, $\cot(\alpha) = 1.5$ and $h = 0.522$ m.

Figure 3.12 shows γ_{P*} is dependent on the wave steepness. Although, Figure 3.12 also shows the scatter of the points increases with increasing wave steepness, which could be due to the limited amount of wave overtopping on the higher wave steepness and smaller wave height. A summary of all the calculated γ_{P*}-values for all conducted tests are shown in Figure 3.13 along with the corresponding mean value of $s_{m-1,0}$. One γ_{P*} value is fitted for three wave heights and one wave steepness in a test campaign.

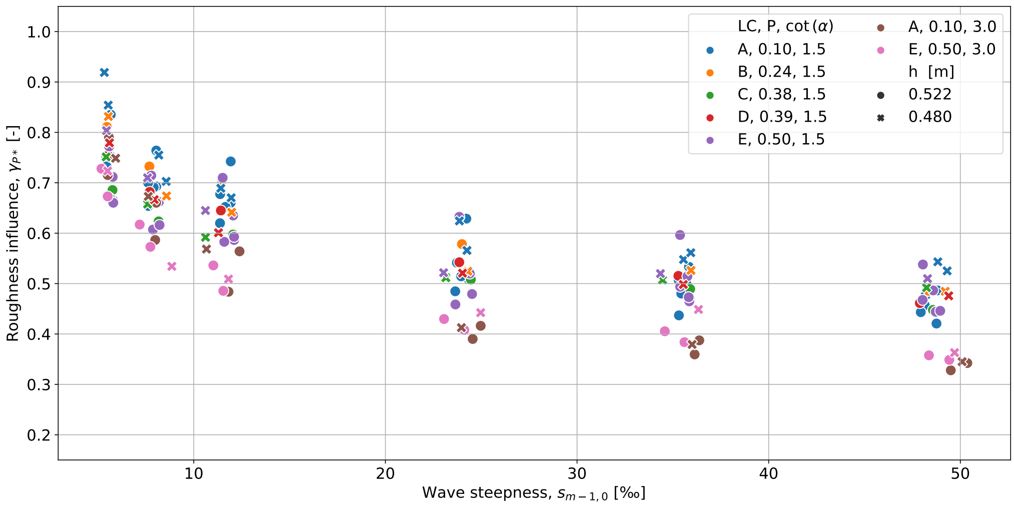

Figure 3.13. All fitted γ_{P*}-values with mean waves steepness $s_{m-1,0}$.

The calculated γ_{P*}-values, are compared to the guideline for γ_{fS} of Eldrup et al. [2022], along with some of the test data used by Eldrup et al. [2022] to establish Eq. (2.12). The comparison are shown in Figure 3.14. The data from De Meyere et al. [2017] indicates that the core had impermeable characteristics. This was stated, since the core material was very fine gravel ($D_{50} \approx 2\,\text{mm}$) and a cloth between the filter layer and the core material was present.

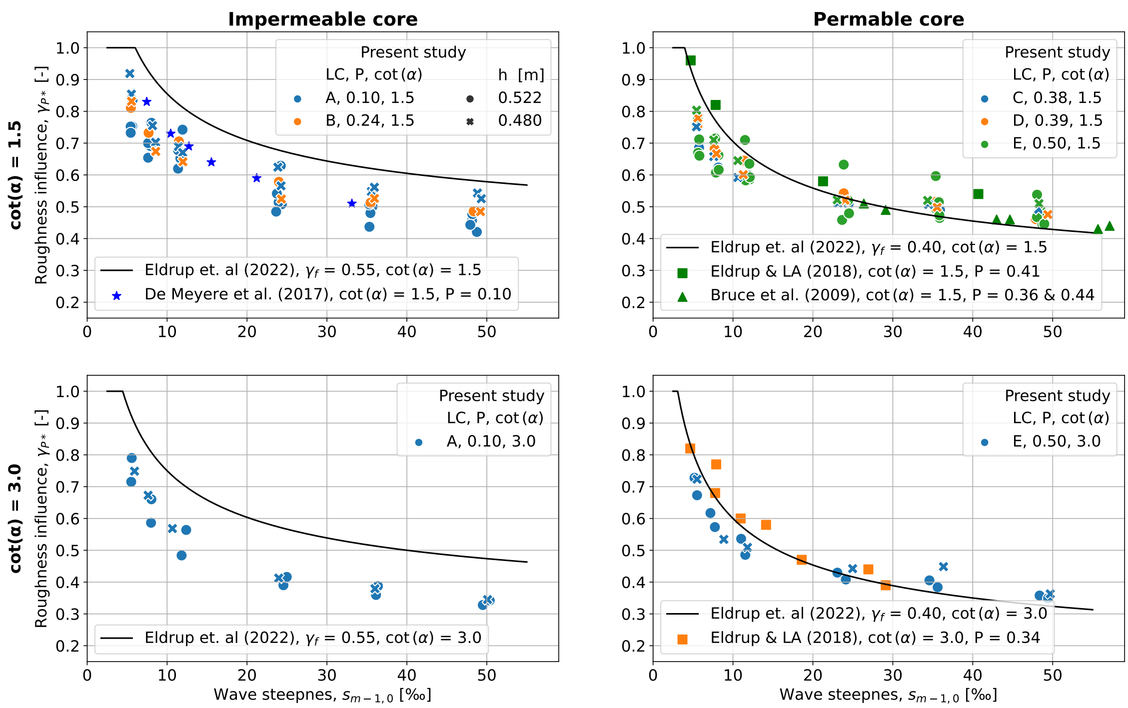

Figure 3.14. All calculated γ_{P*}-values with γ_{fS} by Eldrup et al. [2022], along with data from De Meyere et al. [2017], Bruce et al. [2009] and Eldrup and Andersen [2017].

To further simplify the comparison, Figure 3.15 shows the mean value of all γ_{P*} along with the 90% confidence band for all groups of wave steepness', only separated by the slope of the breakwater model. The lines indicate Eq. (2.12) for the tested slopes for an impermeable and permeable core with a γ_f value of 0.55 and 0.40 respectively. The mean value and 90% confidence bands are calculated based on the tests performed in this project. The 90% confidence band of γ_{P*} for $\cot(\alpha) = 1.5$ varies from ≈ 0.2 at the lowest wave steepness to ≈ 0.1 for high wave steepness.

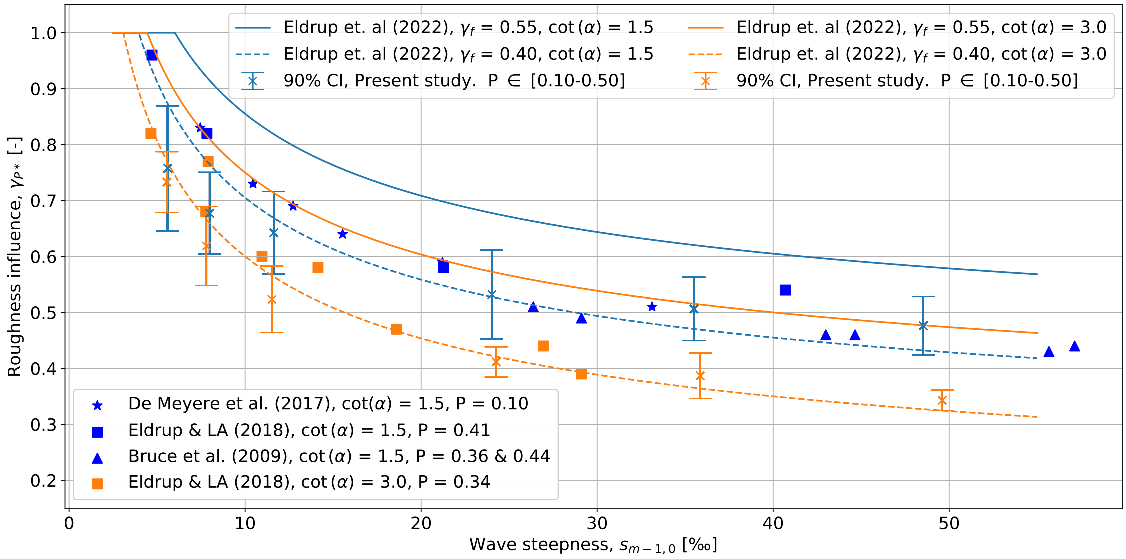

Figure 3.15. Confidence band and mean value for γ_{P*} and mean of $s_{m-1,0}$, along with various data from De Meyere et al. [2017], Bruce et al. [2009] and Eldrup and Andersen [2017].

Figure 3.15 shows that for $\gamma_f = 0.55$ and $\cot(\alpha) = 1.5$ Eq. (2.12) is not within the 90% confidence band of the corresponding test data, which could indicate an overestimation of γ_{fS} for structures with an impermeable core. Figure 3.15 also shows that the implemented data-points used by Eldrup et al. [2022] is somewhat within the measured confidence band of this project, except for the low wave steepness, where they tend to reach higher values of γ_{P*}. This implies, that the conducted tests form this project provides a reasonable accurate estimation of the 90% confidence bands for similar tests.

To cover the dispersion of the upper- and lower limits of γ_{P*}, six separate tests campaigns were conducted on $P = 0.10$ and $P = 0.50$ for $\cot(\alpha) = 1.5$, whereas five of these was with a water depth of $h = 0.522$. It is assumed that a model with $P = 0.10$ will be sufficient to cover the disparity of breakwaters with impermeable cores and $P = 0.50$ for permeable cores. For each test campaign a γ_{P*} was fitted for each group of wave steepness (Figure 3.12), giving at least six separate γ_{P*}-values per group of wave steepness. The results for $P = 0.10$ and $P = 0.50$ are shown in Figure 3.16. It should be mentioned that only three test campaigns were conducted on $P = 0.10$ and $P = 0.50$ for $\cot(\alpha) = 3.0$, were two of these was with a water depth of $h = 0.522\,\text{m}$, meaning that the reliability of the statistics is reduced. Nevertheless, the calculated 90% confidence intervals for these cases are still provided for completeness.

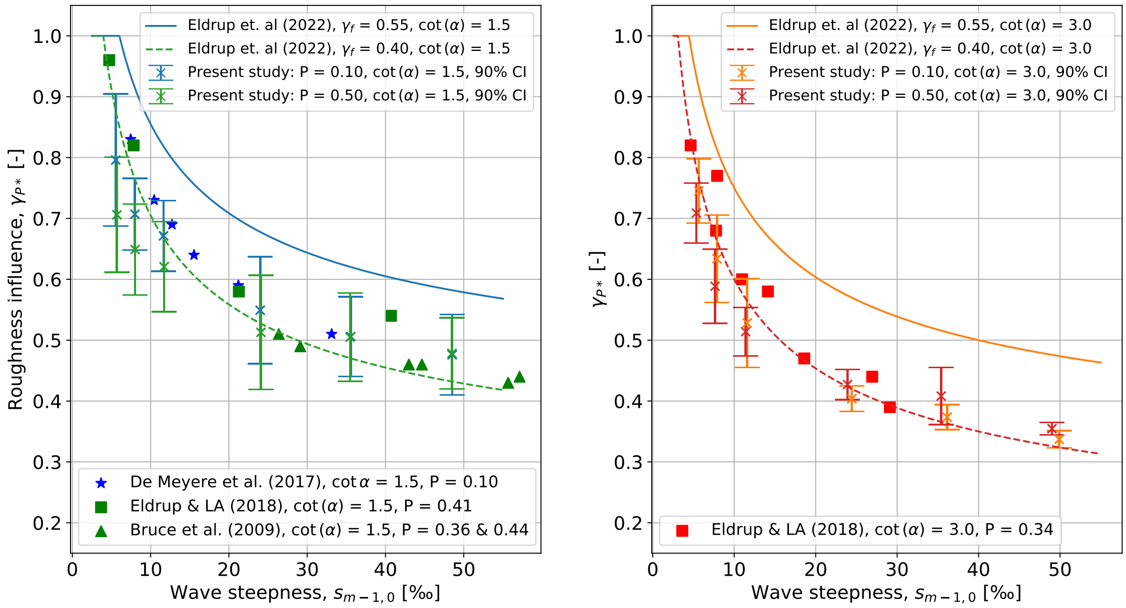

(a) $\cot\alpha = 1.5$. **(b)** $\cot\alpha = 3.0$.

Figure 3.16. γ_{P*}-values for impermeable and permeable cores, $P = 0.10$, $P = 0.50$ respectively, seperated by the slope of the structure.

Figure 3.16 clearly demonstrates that (2.12) by Eldrup et al. [2022] overestimates the influence of roughness (γ_{P*}) on rubble mound breakwaters with an impermeable core ($\gamma_f = 0.55$). Additionally, it shows that (2.12) overestimates γ_{P*} when $s_{m-1,0} < 20‰$, and the overestimation appears to be less pronounced at larger wave steepness values.

Furthermore, the distinction between permeable and impermeable models ($P = 0.10$ and $P = 0.50$) does not seem to have a significant impact on γ_{P*} when $s_{m-1,0} > 30‰$, as they converge towards a similar value of approximately $\gamma_{P*} = 0.45$. The upper and lower limits of the confidence band for $P = 0.1$ and $P = 0.50$ for $\cot(\alpha) = 1.5$ at high wave steepness are, however, approximately 0.55 and 0.40 respectively, which corresponds to the γ_f values presented in Table 1.1 from EurOtop [2018] for two layer armour type rock. The statistical values for the tested structures is listed in Table 3.3. Is should be noted that only the statistical values for $\cot(\alpha) = 1.5$ are included in Table 3.3. This is due to the insufficient amount of data points for structures with $\cot(\alpha) = 3.0$ making the statistics less reliable.

Table 3.3. Statistical values for γ_{P*} from experimental work, done on structures with a slope of $\cot(\alpha) = 1.5$.

	$P = 0.10$			$P = 0.50$			$P \in [0.10, 0.50]$		
$s_{m-1,0}$ [‰]	90% CI, low	μ	90% CI, high	90% CI, low	μ	90% CI, high	90% CI, low	μ	90% CI, high
5	0.69	0.80	0.90	0.61	0.71	0.80	0.65	0.76	0.87
7	0.65	0.71	0.77	0.57	0.65	0.72	0.60	0.68	0.75
10	0.61	0.67	0.73	0.55	0.62	0.69	0.57	0.64	0.72
20	0.46	0.55	0.64	0.42	0.51	0.61	0.45	0.52	0.61
30	0.44	0.51	0.57	0.43	0.51	0.58	0.44	0.51	0.56
45	0.41	0.48	0.54	0.42	0.48	0.54	0.42	0.50	0.53

At wave steepness below 30‰ , there appears to be a difference in γ_{P*} between an impermeable $P = 0.10$ and a permeable structure $P = 0.50$. This difference at low wave steepness can be attributed to the time required for water to dissipate from the pores before being replenished by another wave. Another possible reason could be that, for low steepness waves wave breaking is less likely to occur on the slope of the breakwater. The lesser energy dissipated through wave breaking, the more energy is left to interact with the core of the structure. The impermeable structure does not allow the energy to dissipate through transmission in the core, leaving more energy to be dissipated over the structure in the form of overtopping. This was also discussed in section 1.1. On the contrary, γ_{P*}-values for short waves with steepness' above 40‰ seem to approach a constant value with an average of $\gamma_{P*} = 0.45$.

What may be worth noticing, is that similar observations can be drawn from the work of Van der Meer [1988], when dealing with wave run-up as a function of the breaker parameter, $\xi_{m-1,0}$. Van der Meer [1988] found that for high steepness waves, the relative wave run-up, $R_{u2\%}/H_{m0}$ was relatively similar for structures with impermeable and permeable cores, but the most significant difference was observed at high values of $\xi_{m-1,0}$, see Figure 2.3. Consequently, this led to a notable differentiation in γ_f in the current guidelines between structures with permeable and impermeable cores, disregarding the influence of varying wave steepness (breaker parameters). The observations made in this project, however, suggest that this differentiation is clearly overestimated.

Although Eq. (2.12) from Eldrup et al. [2022] was primarily established from tests conducted on models with a permeable core, the distinction between permeable and impermeable cores seems to be overestimated according to the results in Figure 3.16 and requires some form of correction. Developing a new function for this purpose would not be advantageous since it would only be applicable to a two-layer rock armour type structure. The benefit of using Eq. (2.12) lies in its applicability for structures with all types of armour layers, with differentiation occurring only in the value of γ_f stated in EurOtop [2018].

Figure 3.16 indicates that permeable and impermeable models tend to converge toward the same γ_{P*} value at high wave steepness and approach the equation for permeable structures by Eldrup et al. [2022]. Figure 3.17 displays the results for the data points when all $\gamma_f = 0.40$ is applied for all data points even those with impermeable cores.

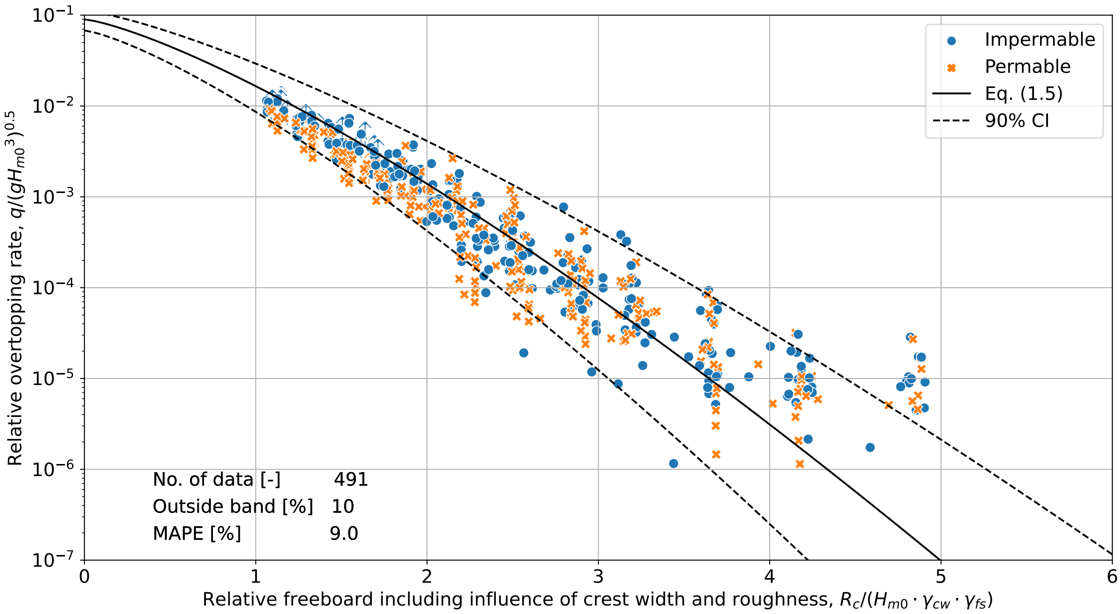

Figure 3.17. Overtopping data and non-breaking formula in (2.8), seperated by core type. A $\gamma_f = 0.40$ is used to correct all the data points. Arrows indicate data points where the overtopping tray was filled to overflowing.

A near 75% reduction of points outside the 90% confidence band is achieved by treating all the models as a permeable core ($\gamma_f = 0.40$) according to EurOtop [2018], using Eq. (2.12) by Eldrup et al. [2022], resulting in a significantly better estimation of the relative overtopping rates. As previously mentioned, a potential improvement in reducing the scatter of the data points, could be achieved by either introducing a new function for γ_{P*} or adopting new values of γ_f. However, what is particularly noteworthy, is that a simple correction has the potential to significantly enhance the estimation accuracy without the need for substantial alterations in the existing guidelines of EurOtop [2018].

3.3.1 Preliminary conclusion

Based on the results obtained from tests conducted in this project, it is evident that using $\gamma_f = 0.55$ for impermeable cores in the case of two layered rock armoured breakwaters leads to an overprediction of the wave overtopping. No reliable relation between the influence of roughness and permeability, γ_{P*} and the notional permeability factor P can, however, be achieved in this project due to the limited amount of testing for P = 0.24, 0.38 and 0.39. Consequently, this project does not provide a specific recommendation for a more nuanced description of the influence of roughness. However, based on the results of $P = 0.10$ and 0.50, it appears that the variation of γ_{P*} for P-values in between these two extremes might be minimal.

By not proposing a new function for γ_{fS}, the present data analysis concludes that Eq. (2.12) by Eldrup et al. [2022] remains applicable and effective for describing the influence of roughness of the armour layer for structures with various types of armour layers. However, it is important to note that the guidelines from EurOtop [2018] regarding γ_f for 2-layer rock armour with impermeable cores is recommended to be adjusted from $\gamma_f = 0.55$ to

$\gamma_f = 0.40$, as it appears to be an overestimation. This project thereby recommends to remove the distinction in influence of roughness for structures of 2-layer rock armour, disregarding the permeability of the core material. This adjustment is supported by the results in Figure 3.16, showing that using $\gamma_f = 0.40$ provides a more accurate estimation of the relative overtopping discharge compared to using $\gamma_f = 0.55$.

Numerical modelling 4

The experimental data showed that wave overtopping of rubble mound breakwaters is far less influenced by the core permeability than EurOtop [2018] suggests. To further support this claim, a 2-dimensional numerical wave tank model of wave overtopping of structures with an impermeable and permeable core was constructed. The structures of interest are layer composition A ($P = 0.10$) and E ($P = 0.50$) with front slope angle $\cot(\alpha) = 1.5$ as the test results of these compositions are associated with high credibility. The objective of the numerical model is to examine if the relative difference in wave overtopping is similar to that of the experimental data.

The numerical modelling was based on computational fluid dynamics (CFD) in the open-source software, OpenFOAM-v2206 utilising the third-party toolbox waves2Foam, [Jacobsen, 2017]. The waves2Foam toolbox expands the capabilities of OpenFOAM for coastal engineering applications enabling the generation and absorption of surface water waves and wave-structure interaction for porous bodies, such as rubble mound breakwaters. General settings and numerical schemes are available in appendix F.

4.1 Governing equations

The behaviour of the fluid is governed by the Navier-Stokes equations, where the momentum- and continuity equation yields (4.1) and (4.2). [Jacobsen, 2017, Eq. 2.1 and Eq. 2.2]

$$\frac{\partial \rho \mathbf{u}}{\partial t} + \nabla \cdot \rho \mathbf{u}\mathbf{u}^T = -\nabla p^* + \mathbf{g} \cdot (\mathbf{x} - \mathbf{x}_r)\nabla p + \nabla \cdot \mu_{tot} \nabla \mathbf{u} \tag{4.1}$$

$$\nabla \cdot \mathbf{u} = 0 \tag{4.2}$$

where ρ is the fluid density, $\mathbf{u}$ is the velocity vector, $\nabla = (\partial/\partial x, \partial/\partial y, \partial/\partial z)$ is the differential operator, $p^* = p - \rho \mathbf{g} \cdot \mathbf{x}$ is the excess pressure calculated from the total pressure p and the static pressure $\rho \mathbf{g} \cdot \mathbf{x}$. $\mathbf{x} = (x, y, z)$ is the coordinate vector, $\mathbf{x}_r$ is a reference location, $\mathbf{g}$ is the gravitaional vector and μ_{tot} is the total dynamic viscosity. (4.1) and (4.2) are solved by the OpenFOAM interFOAM solver for two incompressible, isothermal immiscible fluids. interFOAM uses the VOF method to track the position and shape of the interface between the fluids and solves the Navier-Stokes equation simultaneously, for each fluid phase. [G. Jacobsen et al., 2011]

The interphase between two fluids is tracked using a phase fraction α. The spatial variation of the fluid properties is described by the scalar field α and the fluid properties in the flow field are determined from a linear function as shown in (4.3) and (4.4). [G. Jacobsen et al., 2011,Eq. 5]

$$\rho = \alpha\rho_1 + (1-\alpha)\rho_0 \tag{4.3}$$

$$\mu = \alpha\mu_1 + (1-\alpha)\mu_0 \tag{4.4}$$

Where μ is the dynamic viscosity and the subscripts 0 and 1 refer to fluid properties where $\alpha = 0$ and $\alpha = 1$ respectively. In waves2Foam $\alpha = 1$ corresponds to a cell full of water and $\alpha = 0$ corresponds to a cell full of air. The distribution scalar field α is described by the advection equation in Eq. (4.5). [G. Jacobsen et al., 2011, Eq. 4]

$$\frac{\partial\alpha}{\partial t} + \nabla\cdot\mathbf{u}\alpha + \nabla\cdot\mathbf{u}_r(1-\alpha)\alpha = 0 \tag{4.5}$$

Where $\mathbf{u}_r$ is a relative velocity.

4.1.1 Modification due to porous media

To model the porous flow within the permeable layers of the rubble mound breakwater model, waves2Foam offers the possibility to include porous media. The velocity in the porous media is defined as the filter velocity $\mathbf{u}$, given in (4.6).

$$\mathbf{u} = n\mathbf{u}_p \tag{4.6}$$

Where n is the porosity and $\mathbf{u}_p$ is the pore velocity vector. The distribution scalar field α is affected by a porous media since the voids of the permeable material limit the amount of fluid available in a cell. The advection equation is therefore also modified to include porous media in Eq. (4.7). [Jacobsen, 2017, Eq. 2.7]

$$\frac{\partial\alpha}{\partial t} + \frac{1}{n}(\nabla\cdot\mathbf{u}\alpha + \nabla\cdot\mathbf{u}_r(1-\alpha)\alpha) = 0 \tag{4.7}$$

The modified momentum equation for permeable structures is given by (4.8). [Jacobsen, 2017, Eq. 2.4]

$$(1+C_m)\frac{\partial}{\partial t}\frac{\rho\mathbf{u}}{n} + \frac{1}{n}\nabla + \cdot\frac{\rho}{n}\mathbf{u}\mathbf{u}^T = -\nabla p^* + \mathbf{g}\cdot(\mathbf{x}-\mathbf{x}_r)\nabla\rho + \frac{1}{n}\nabla\cdot\mu_{tot}\nabla\mathbf{u} - \mathbf{F}_p \tag{4.8}$$

Where C_m is the added mass coefficient, added to take the transient interaction between grains and water into account and $\mathbf{F}_p$ is the resistance force, included to take the resistance due to porous media into account. C_m takes into account the inertia term in the extended Darcy–Forchheimer equation, whereas $\mathbf{F}_p$ takes the linear- and non-linear resistance forces into account in the extended Darcy–Forchheimer equation. [Jensen et al., 2014b].

The formula for the resistance force, $\mathbf{F}_p$ is derived by Jensen et al. [2014b] whereas the added mass coefficient, C_m is derived by van Gent [1995], shown in Eq. (4.9) and Eq. (4.10), respectfully.

$$\frac{\mathbf{F}_P}{\rho} = a\mathbf{u} + b\mathbf{u}||\mathbf{u}||_2 \tag{4.9}$$

$$C_m = \gamma_P\frac{1-n}{n} \tag{4.10}$$

Where a and b are resistance coefficients and γ_P is a closure coefficient with a value of 0.34 [G. Jacobsen et al., 2011]. The coefficients a and b are implemented for the porosity zone by use of the Darcy-Fochheimer flow model *nativeOF* in waves2Foam [Jacobsen, 2017]. The model includes the viscous forces through the coefficient d and the inertia forces by f. A further description of the determination of d and f is provided in Appendix C. The material properties and porosity coefficients are listed in Table 4.1.

Table 4.1. Material properties of rock material. The coefficients are calculated based on an experiment, explained in Appendix C.

	Median weight	Nominal diameter	Grading	Mass density	Darcy coef.	Forchheimer coef.	Porosity
Rock class	W_{n50} [g]	D_{n50} [m]	D_{n85}/D_{n15} [-]	ρ [kg/m^3]	$d \times 10^6$ [1/m^2]	f [1/m]	n [-]
I	221.00	0.044	1.296	2620	4.02	239.61	0.43
II	30.00	0.022	1.115	2658	6.57	737.01	0.43
III	9.00	0.015	1.357	2768	7.23	983.11	0.43
IV	5.15	0.012	1.298	2713	8.70	1428.70	0.41
V	0.65	0.006	1.360	2936	23.03	2631.93	0.39

The individual influence of each stone is not taken into account in the numerical solution. Instead, the average resistance of the porous layers on the flow is modelled.

The inclusion of a turbulence model may capture the wave breaking better and reduce the turbulent flow on the rear. A turbulence model may therefore affect the results positively, as the wave breaking is of interest and appear to influence the overtopping. Though the numerical model is not expected to suffer from the absence of a turbulence model, based on the investigation by Jensen et al. [2014a]. The findings of Jensen et al. [2014a] were, however, predicated on the fact that no or little wave breaking occurred. Jensen et al. [2014a] argues that the turbulence within the porous media is captured sufficiently by the Darcy-Fochheimer flow model. Nevertheless, no turbulence model is included and the effects will not be investigated further.

4.1.2 Relaxation zone

The relaxation zone technique is implemented in the waves2Foam toolbox and allows for both wave generation and absorption. The relaxation zone technique employs a weighting between the computed solution in the velocity field and the indicator field in the target solution [Jacobsen, 2017]. The relaxation zones are implemented by the use of an explicit time integration method, given in Eq. (4.11).

$$\phi = (1 - w_R)\phi_{\text{target}} + w_R\phi_{\text{computed}} \tag{4.11}$$

Where ϕ is either the velocity field $\mathbf{u}$ or the distribution scalar field F and w_R is a weighting function. This method explicitly corrects the velocity field $\mathbf{u}$ and the distribution scalar field F before solving the pressure-velocity field, [G. Jacobsen et al., 2011]. The weighting function is implemented using the exponential weight distribution, following the work of Fuhrman et al. [2006].

$$w_R(\sigma) = 1 - \frac{\exp(\sigma^p) - 1}{\exp(1) - 1} \tag{4.12}$$

Where p is equal to 3.5 as a default value and σ is a local coordinate system, $\in [0:1]$. The definition of σ is so that in the interface between the non-relaxed part of the domain and the relaxation zone w_R is always equal to one and equal to zero when at domain outlet as stated in Eq. (4.13) and Eq. (4.14). [G. Jacobsen et al., 2011]

$$w_R(0) = 1 \tag{4.13}$$

$$w_R(1) = 0 \tag{4.14}$$

No relaxation zone where used for wave generation. Instead, a moving wall boundary method was applied to generate the waves.

The relaxation zone technique was, however, utilized for wave absorption in the validation of the moving wall boundary. The extent of the outlet relaxation zone is shown in Figure 4.1. Regular wave trains were generated for layer composition A during the experimental investigations and the wave overtopping and surface elevation, as well as the wavemaker signal, were logged during testing. The wavemaker signal contains the position of the paddle during run time, why the moving wall boundary will use the position as a boundary condition, utilizing the dynamic mesh functionality in OpenFOAM. The wavemaker signal contains the reflection compensation from the active absorption described in section 3.1.2.

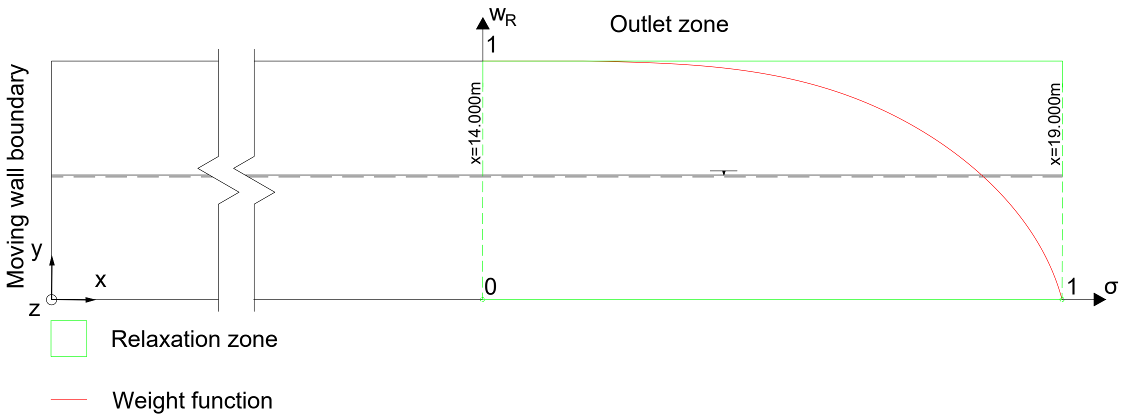

Figure 4.1. Illustration of weight function $w_R(\sigma)$ in outlet zone.

No relaxation zone was implemented for wave generation or absorption in the numerical models of the breakwater compositions.

The validation of the moving wall boundary is described in appendix E. Spacial convergence for the wave generation concluded that a global mesh size of $1.85 \times 1.75 \times 100$ cm ($dx \times dy \times dz$) was sufficient for capturing the desired wave propagation and wave height. Cells sizes will henceforth be referred to in $dx \times dy$ format, as all cells span 100 cm in z. However, no temporal convergence for the paddle was examined due to the limitations of the available resources. No additional analysis of the overtopping was performed.

4.2 Spatial discretization

The computational domain is created as a predominantly hexahedral mesh using the *blockMesh* utility in OpenFOAM. Modification and refinement of the mesh were done using the utility *snappyHexMesh*. The model domain was made to replicate the setup in the wave flume, meaning the toe and superstructure were placed approximately the same distance from the moving wall boundary as the model was from the wavemaker in the experiment, confer Figure 3.1.

The refinement zones and levels used for validation of the moving wall boundary are applied for the domains including the breakwater model. The reader is referred to appendix E for further details on this matter. The cell size around the free surface was of size $0.44 \times 0.44\,\mathrm{cm}$. Additional refinement was, however, applied near the breakwater model with slight variations for each layer composition. Layer composition A ($P = 0.10$) was modelled with an impermeable core by removing the cells within the core and creating a *wall* boundary, such as the one used for the bottom. The 2D model domain of both layer compositions A ($P = 0.10$) and E ($P = 0.50$) are shown in Figure 4.2a and 4.2b respectively.

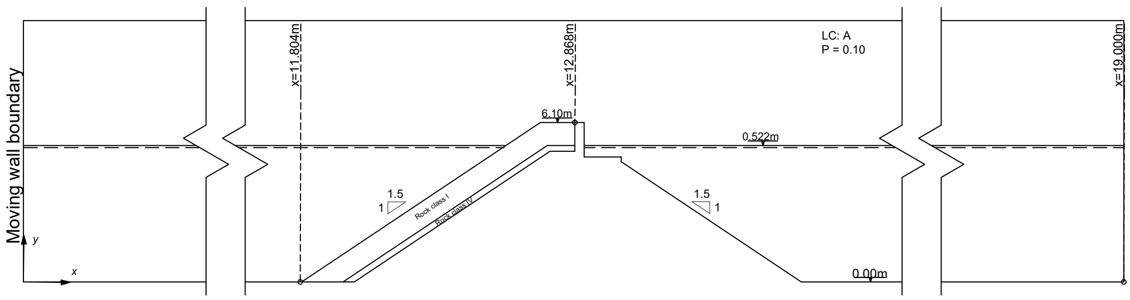

(a) 2D domain of layer composition A ($P = 0.10$).

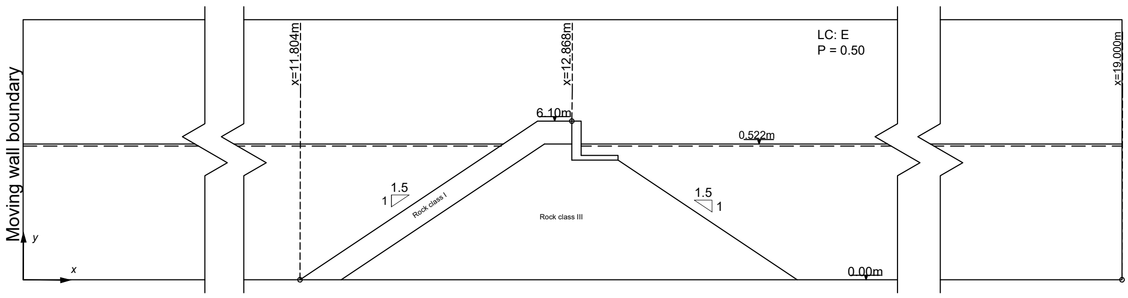

(b) 2D domain of layer composition E ($P = 0.50$).

Figure 4.2. Domain of breakwater models with layer composition and notional permeability P.

A refinement zone of refinement level three with a resolution of $0.23 \times 0.22\,\mathrm{cm}$ was added to capture the overtopping of the superstructure for both layer compositions. A boundary layer of thickness $0.15\,\mathrm{cm}$ (two cells) was added around the superstructure for both numerical models, with the boundary layer also applied to the front and back of layer composition A ($P = 0.10$).

Two regular waves are investigated in the numerical wave tank. Both paddle signals used for wave generation are from physical model tests in the flume on layer composition A. Examination of the reflection coefficient for layer composition A ($P = 0.10$) and E ($P = 0.50$) revealed a negligible influence of the permeability of the structure on the reflection coefficient. The paddle signal sampled from model tests on layer composition A ($P = 0.10$) is therefore assumed to be similar to a paddle signal sampled from tests with layer composition E ($P = 0.50$). The mesh characteristics in relation to the simulated sea states are listed in Table 4.2. Wave heights H in Table 4.2 are computed values from the selection analysis of the experimentally measured surface elevation from the wave flume.

Table 4.2. Discretization of the domain in relation to measured wave characteristics.

LC	P	h [m]	T_p [s]	H [m]	L_p [m]	$cells/L_p$	$cells/H$	Total cells
A	0.10	0.522	1.46	0.1505	2.856	617	34	612859
A	0.10	0.522	3.70	0.1694	8.703	1879	38	612859
E	0.50	0.522	1.46	0.1505	2.856	617	34	654913
E	0.50	0.522	3.70	0.1694	8.703	1879	38	654913

The computational mesh for layer composition A ($P = 0.10$) is shown in Figure 4.3a along with the discretization near the superstructure and toe in Figure 4.3b and 4.3c respectively.

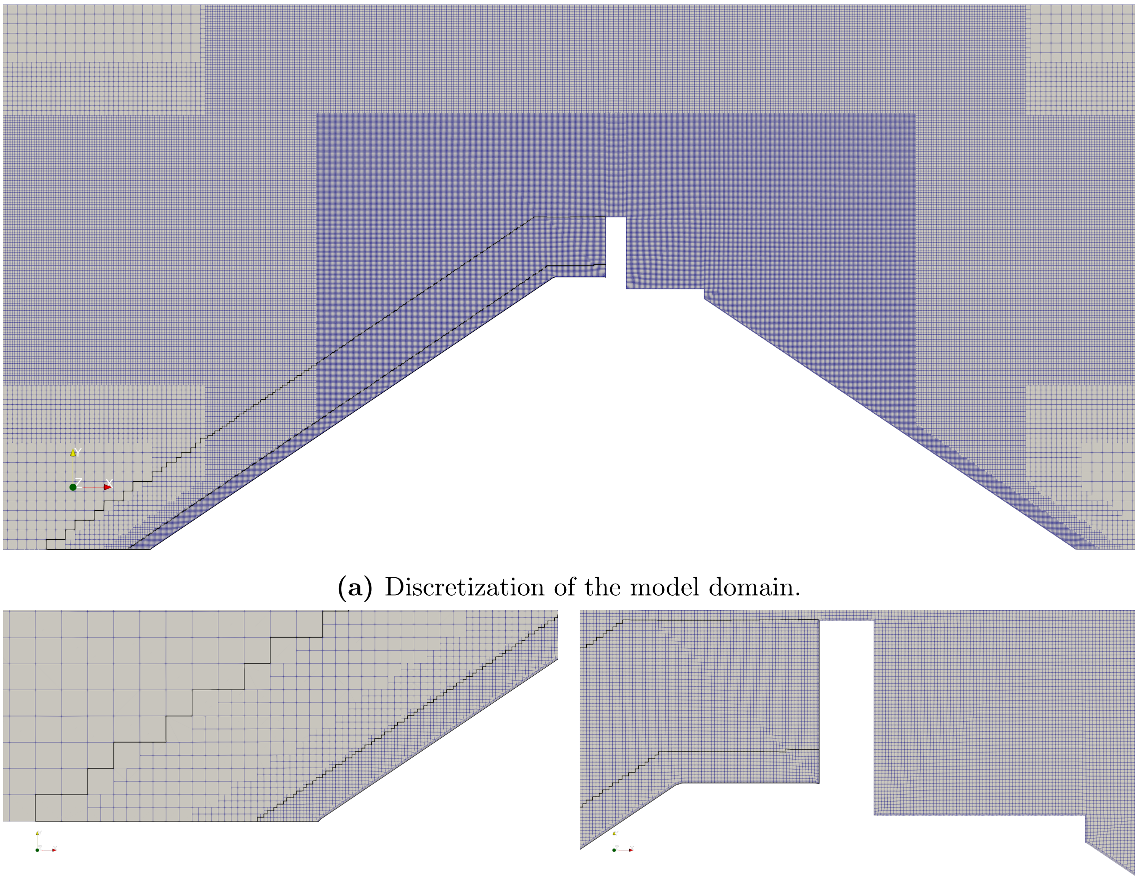

(a) Discretization of the model domain.

(b) Discretization near the toe.

(c) Discretization near the superstructure.

Figure 4.3. Discretization of layer composition A ($P = 0.10$). Cells marked for the porosity zones are outlined in black.

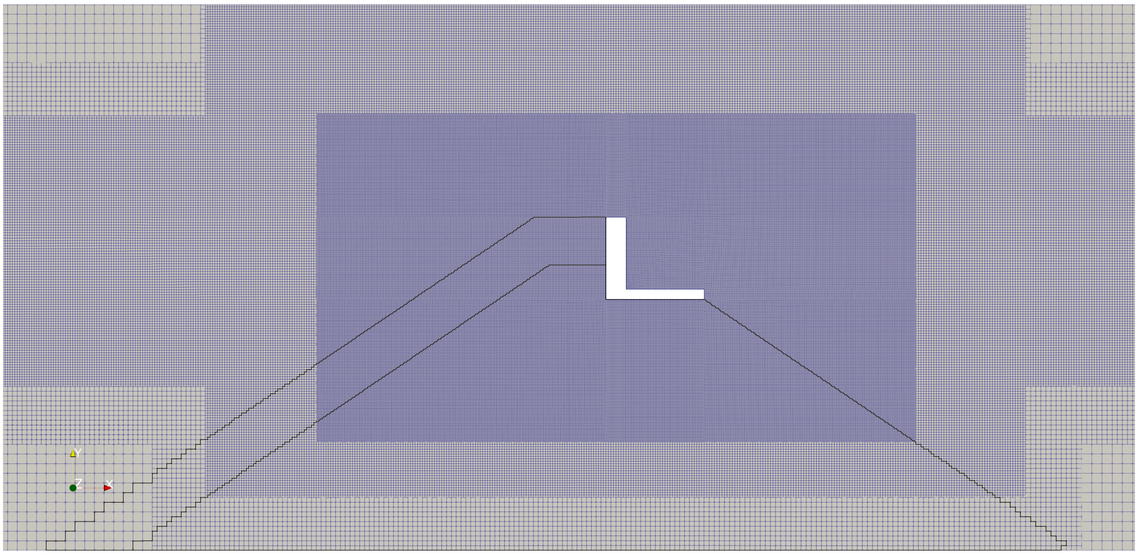

Figure 4.4. Discretization of layer composition E ($P = 0.50$). Cells marked for the porosity zones are outlined in black.

4.3 Results

The velocity flow field for the wave period of $T_p = 1.46\,\mathrm{s}$ and a wave height of $H = 0.1505\,\mathrm{m}$ is presented in Figure 4.5 for layer compositions A ($P = 0.10$) and E ($P = 0.10$), where *alpha.water* is the phase fraction α and *U Magnitude* indicates the magnitude of the velocity vectors. The wave is overtopping the structure in Figure 4.5a and 4.5b where the velocity vectors for layer composition E the flow within the core, whereas the impermeable core of layer composition A prevent any dissipation within the core and more energy is deflected on the slope.

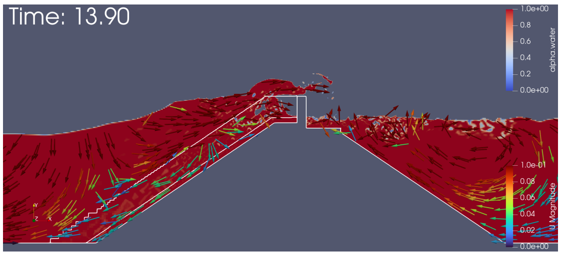

(a) Layer composition A ($P = 0.10$).

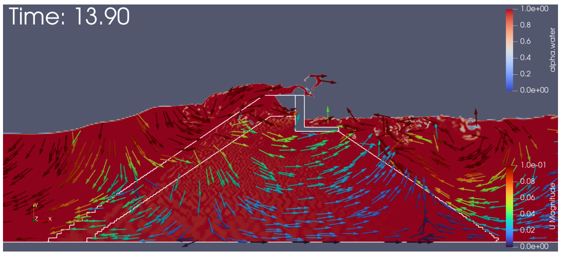

(b) Layer composition E ($P = 0.50$).

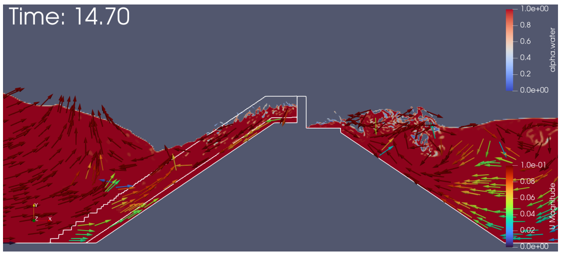

(c) Layer composition A ($P = 0.10$).

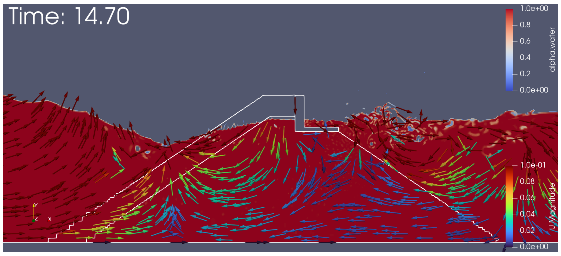

(d) Layer composition E ($P = 0.50$).

Figure 4.5. Snapshots of the velocity flow field for wave period of $T_p = 1.46\,\mathrm{s}$, with a wave height of $H = 0.1505\,\mathrm{m}$ for layer compositions A ($P = 0.10$) and E ($P = 0.50$).

The velocity flow velocity field is indicated by vectors. During the up-rush of the wave at $t = 13.9\,\mathrm{s}$ in Figure 4.5a, the flow field primarily follows the slope of the structure, indicating the upward direction of wave energy. When comparing the core interaction, it can be observed that for $P = 0.10$, the velocity flow in the armour layer is more aligned with the slope of the structure. In contrast, for $P = 0.50$, some of the flow is directed inward into the core, indicating that some of the wave energy is dissipated herein.

During the down-rush at $t = 14.7\,\mathrm{s}$ in Figure 4.5c and 4.5d, the velocity field is observed to be directed downwards along the slope, converging towards the surface. In the case of $P = 0.50$, the flow velocity in the core is observed to be directed outward throughout the armour layer. This observation corresponds to the reasoning behind why reshaping breakwaters attain S-profiles. Overall these observations correlate well with the physical processes of wave-structure interaction, discussed in section 1.1. However, it should be noted that no turbulence model was included, why the wave breaking on the slope may not be captured fully by the numerical model.

The measured surface elevation from the numerical and experiment are shown in Figure 4.6 and 4.7 for layer composition A ($P = 0.10$) for sea state with measured wave heights $H = 0.1505\,\mathrm{m}$ and $H = 0.1694\,\mathrm{m}$ with wave periods $T_p = 1.46\,\mathrm{s}$ and $T = 3.70\,\mathrm{s}$ respectively. The remaining measurements from the numerical model are included in appendix G along with additional times steps for the velocity fields shown in Figure 4.5. A shift in the signals for the surface elevation was observed but remains unexplained. The signals were aligned with the phase shift between the numerically and experimentally measured waves.

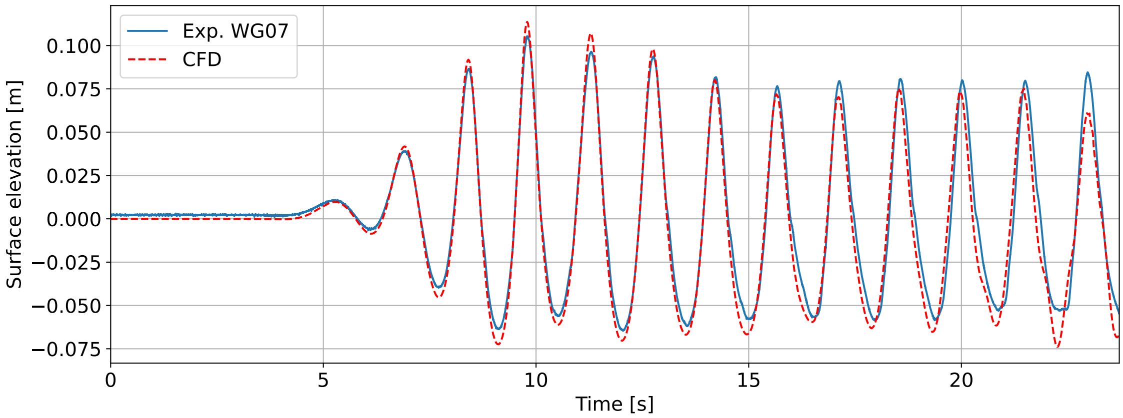

Figure 4.6. Numerical and experimental measurements of the surface elevation for layer composition A ($P = 0.10$) at WG07 ($x = 9.057\,\mathrm{m}$). $H = 0.1505\,\mathrm{m}$ and $T_p = 1.46\,\mathrm{s}$.

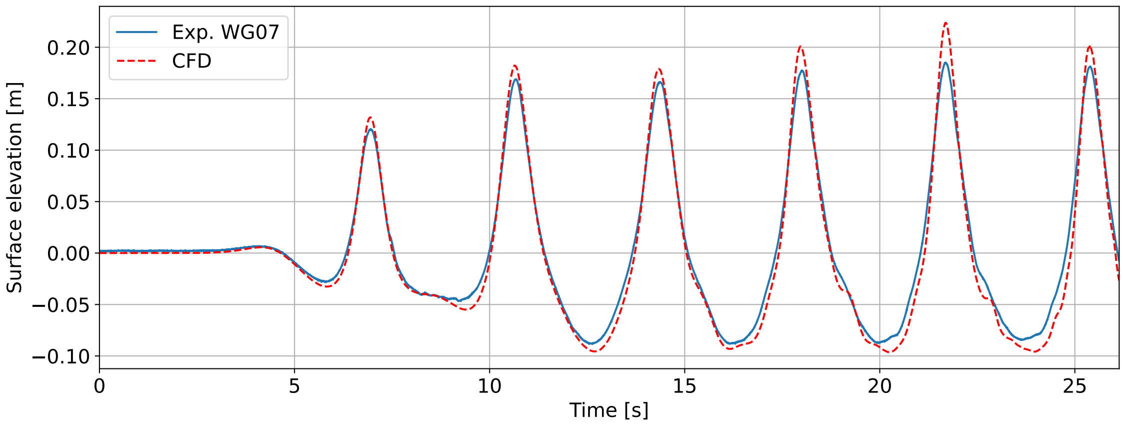

Figure 4.7. Numerical and experimental measurements of the surface elevation for layer composition A ($P = 0.10$) at WG07 ($x = 9.057\,\mathrm{m}$). $H = 0.1694\,\mathrm{m}$ and $T_p = 3.70\,\mathrm{s}$.

The numerically measured surface elevation shown in Figure 4.6 and 4.7 shows that the wave period is captured well by the numerical model. However, the crest is slightly higher for the first five wave periods for the CFD than for the experimental waves. This changes later, as the reflected waves interfere with the signal and the active absorption from the paddle signal starts to influence the incident wave. The trough is slightly lower for all measured waves of the CFD model.

Figure 4.7 also shows that the numerical model captures the generated waves well. The same tendency of the crest and trough is observed for both wave trains shown in Figure

4.6 and 4.7. The measured wave height is therefore expected to be slightly larger than that of the experiment. Though no wave height is determined from the surface elevation from the CFD, the computed incident wave height H from the experiment is used in further computations. Furthermore, the ramp-up wave generated from the wavemaker signal is captured very well for both surface elevations.

The measured overtopping of layer composition A ($P = 0.10$) for the wave trains shown in Figure 4.6 and 4.7 are provided in Figure 4.8 and 4.9. The yellow area marked in Figure 4.8 and 4.9 depicts the area used for computing the individual overtopping volume V of each wave. Note however that the last overtopping wave in Figure 4.9 is incomplete and is therefore disregarded.

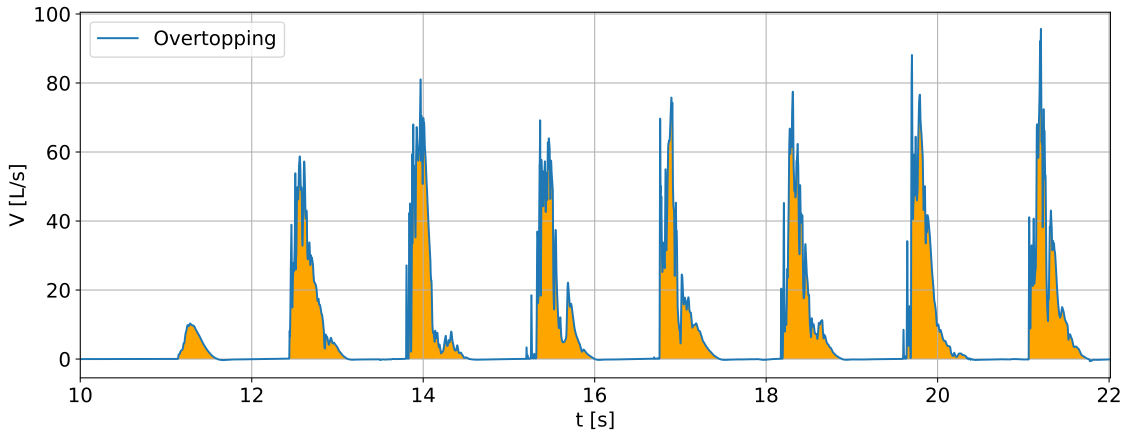

Figure 4.8. Numerical overtopping measurements for layer composition A ($P = 0.10$). $H = 0.1505\,\mathrm{m}$ and $T_p = 1.46\,\mathrm{s}$.

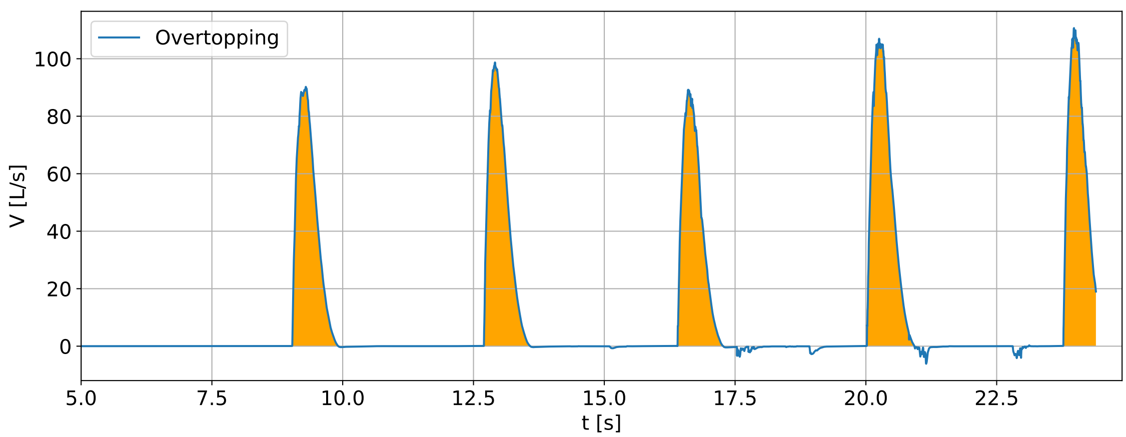

Figure 4.9. Numerical overtopping measurements for layer composition A ($P = 0.10$). $H = 0.1694\,\mathrm{m}$ and $T_p = 3.70\,\mathrm{s}$.

The overtopping signal of $H = 0.1505\,\mathrm{m}$ and $T_p = 1.46\,\mathrm{s}$ in Figure 4.8 is much more violent than that of $H = 0.1694\,\mathrm{m}$ and $T_p = 3.70\,\mathrm{s}$ in Figure 4.9. The difference may be because the wave with $H = 0.1505\,\mathrm{m}$ and $T_p = 1.46\,\mathrm{s}$, breaks on the slope of the structure causing more energy to dissipate through wave breaking and causing more dispersed or spray overtopping. On the contrary, the wave overtopping of $H = 0.1694\,\mathrm{m}$ and $T_p = 3.70\,\mathrm{s}$

is quite smooth and no energy appears to be dissipated through wave breaking. Some negative overtopping is observed, especially in Figure 4.9, this volume is excluded and most likely caused by the volatile disturbance on the rear side by the overtopping wave. This is considered numerical noise and is simply disregarded.

The average overtopping volume V and discharge q are listed in Table 4.3. Individual values for each wave are available in appendix G. The average overtopping discharge q is computed from the average volume V and wave period T_p of the wave. The interface of which the overtopping is sampled was 1 m wide.

LC	P	h [m]	T_p [s]	H [m]	V_{avg} [L]	q_{avg} [L/s/m]
A	0.10	0.522	1.46	0.1505	9.91	14.48
A	0.10	0.522	3.70	0.1694	14.45	53.47
E	0.50	0.522	1.46	0.1505	7.67	11.20
E	0.50	0.522	3.70	0.1694	11.46	42.39

Table 4.3. Measured overtopping parameters of the simulated models.

The data of Table 4.3 is depicted graphically in Figure 4.11 and 4.10 along with the wave overtopping measured in the wave flume of layer composition A ($P = 0.10$).

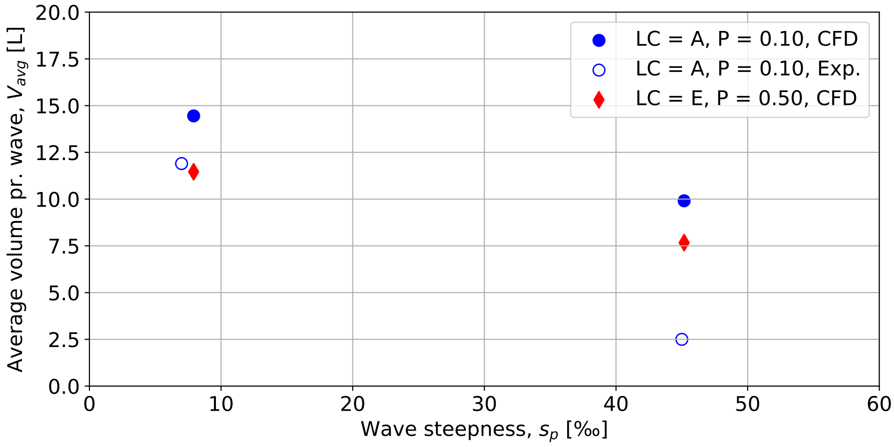

Figure 4.10. Average overtopping volumes V of the CFD and the experiment.

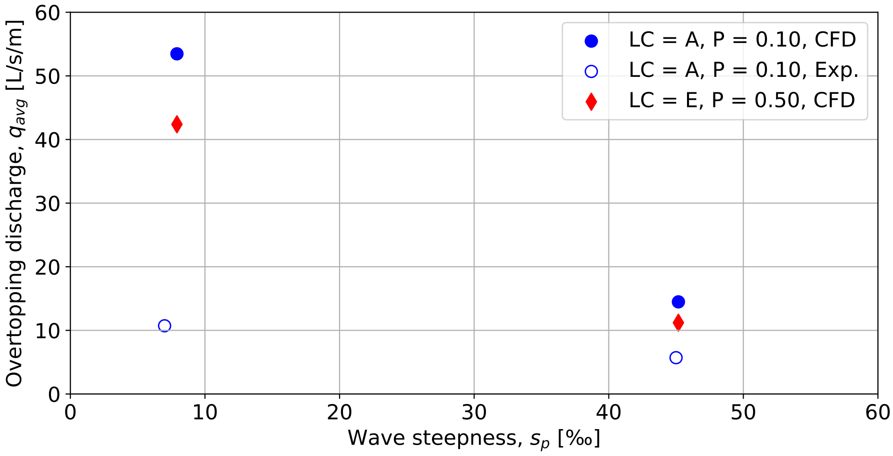

Figure 4.11. Average overtopping discharge q of the CFD and the experiment.

From Figure 4.10 the average overtopping volumes V_{avg} for layer composition A ($P = 0.10$) for the CFD and experiment approach the same value for wave period $T_p = 3.70\,\mathrm{s}$ ($s_p \approx$‰). The deviation V_{avg} between the CFD and the experiment is, however, higher for $T_p = 1.46\,\mathrm{s}$ ($s_p \approx 45$‰). Higher values for the overtopping volume V are generally measured in the numerical model. The average overtopping discharge q_{avg} in Figure 4.11 shows the reverse of Figure 4.10 as the agreement between the CFD and the experimental measurement of layer composition A ($P = 0.10$) is better for $T_p = 1.46\,\mathrm{s}$ ($s_p \approx 45$‰). The reason for the deviations between the CFD and experimental measurements is, however, unexplainable.

Nevertheless, it seems apparent that layer composition A ($P = 0.10$) with an impermeable core and layer composition E $P = 0.50$ form an upper and lower bound, respectively. This may indicate that there is a small influence of the permeability on the overtopping but it may be of significantly small proportions, making the influence difficult to quantify from experimental data with scatter as described in Section 3.3. The limited data set does not show any trend that may indicate a clear correlation between the wave overtopping and the permeability or the wave steepness s. Mapping these influences warrants further studies with a larger numerical dataset.

5 Discussion

This project investigated the influence of permeability and roughness of rubble mound breakwaters and its effect on wave overtopping. Through 491 separate tests, the conducted data analysis found that the influence of the permeability of structures was most significant at low wave steepness' but seemed to converge at high wave steepness'. Even though this was a similar observation as in the work by Van der Meer [1988] for roughness influence on wave run-up, when comparing the findings to the current guidelines of EurOtop [2018] or the improved guidelines by Eldrup et al. [2022], a significant difference was observed. These observations were attempted to be replicated through computational fluid dynamic (CFD) simulations, but failed to do so.

The data analysis in this study involved calculating the mean value of the influence of roughness, γ_{P*}, and its corresponding 90% confidence interval for all conducted tests, categorised based on the slope of the structure, $\cot(\alpha)$. Furthermore, the study determined the mean value and 90% confidence interval for both layer compositions A ($P = 0.10$) and E ($P = 0.50$) as five separate test campaigns were conducted for each. This establishes a stronger basis for the subsequent findings and serves to improve the reliability of the conclusions drawn.

The final recommendation did not involve changing the formulae of the current guidelines, but only removing the differentiation in γ_f-values between a permeable and impermeable core. However, as the results from the data analysis suggested, this led to the Eq. 2.12 being both in the upper and lower part of the 90% confidence interval. If assuming the calculated confidence intervals are representative, a certain amount of precaution may need to be taken into account, in order to not inaccurately estimate γ_{P*}. This may be done by fitting a new function to the mean values of the confidence intervals.

However, it would still be beneficial to discuss, what might affect the calculated confidence band, beyond rearrangement of armour layers, even though some of this has already been discussed in appendix D. When studying the confidence band of the influence of roughness, the conducted test was primarily focused on varying the armour layer as the sole variable, from one test campaign to another. This also included some small inevitable changes in the filter layer or the core, but due to the small grain size, compared to the armour layer, this is not expected to significantly alter the deviation of the results in any way. However, due to the randomness of waves, the repeatability of the test might have caused an additional deviation in the results, even though the same wave trains were used. This was not investigated in this project, however, Geeraerts et al. [2009] did research on this topic on similar test set-ups and found that for the measured overtopping, the coefficient of variance (COV $= \sigma/\mu$) may reach up to 13%. This was, however, conducted on breakwaters with carefully placed Antifer cubes as armour layer, so the COV due to repeatability for the present study might take on another value due to the inherent randomness in the arrangement of the armour rocks.

The 90% confidence intervals presented in this project supports the argument for recommending a change in the current guidelines specified EurOtop [2018, Table 6.2] for γ_f, (specifically for Rocks 2 layer, impermeable core). Given that, the confidence intervals where quite significant for the tested type of armour layer, it might be worthwhile to delve into the discussion surrounding the γ_f-values for the remaining types of armour layer. A recap of the calculated 90% for this project confidence intervals is shown in Figure 5.1 along with the values of γ_f from EurOtop [2018, Table 6.2]. Note that only the confidence bands for $\cot(\alpha) = 1.5$ is displayed, since γ_f is tested for rubble mound structures with a slope of 1:1.5.

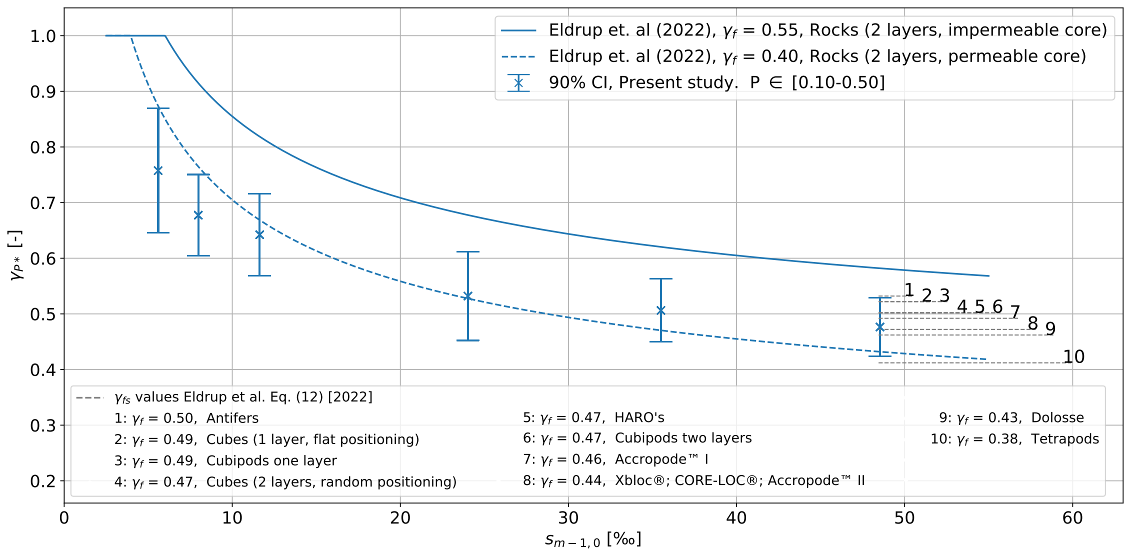

Figure 5.1. Calculated confidence bands for γ_{P*} along with the γ_{fS}-value calculated by the recommended values of γ_f for numerous types of armour layer.

Figure 5.1 demonstrates that the confidence interval calculated in this study, encompasses almost all types of armour layers, with the exception of 2 types, whereas the γ_f for Rocks (two layer impermeable core) was in this study suggested as being overestimated. This observation is noteworthy as it may raise questions about the accuracy of the current γ_f values. However, whether or not the same deviation of γ_{P*} would be observed for the other types of armour layer, has not been investigated in this project. However, Geeraerts et al. [2009] did research on this topic, regarding rearranging the armour layer, consisting of Antifer cubes. Geeraerts et al. [2009] found that a COV of 53% was observed. This may indicate that the same deviation of γ_{P*} might be observable for all types of armour layers.

In an effort to further quantify the influence of the permeability a numerical model based on computational fluid dynamics was developed to enhance the reliability of the test data. The results indicated the presence of an upper and lower bound for the permeability of the core. The results are, however, limited and warrant a larger dataset consisting of more wave steepness and layer compositions. The use of regular waves does seem sufficient to capture the effect of the permeability for numerical purposes. The experimental data is associated with the highest credibility, compared to the numerical data. Based on the numerical results the influence of the core permeability appears to be quite small and may be difficult to capture in experimental investigation due to the scatter of the empirical data. To better compare the numerical and experimental findings, implementing irregular wave series, using the same paddle movements as those in the wave flume or implementing turbulence modelling, may be advantageous.

6 Conclusion

A review of the design tools for wave overtopping prediction found that the current guidelines of EurOtop [2018] offers no intermediate level of core permeability. Instead, the guidelines distinguished the permeability in absolute terms (permeable and impermeable) by the parameter γ_f, potentially leading to the overestimation of wave overtopping. Data from Eldrup et al. [2022] indicated an influence of the permeability of the structure but the available data did not show a consistent trend.

Through intensive experimental tests, this project studied the effects of permeability on the influence of roughness factor γ_{P*} by testing small-scale breakwater models with permeable and impermeable cores. Five different layer compositions with notional permeability factors P ranging from 0.10 to 0.50 were tested. To further study the deviation of γ_{P*} multiple test campaigns were conducted on layer composition A ($P = 0.10$) and E ($P = 0.50$), creating deviation by rearranging the armour layer.

A rather significant extent of the scatter of γ_{P*} was observed. The scatter was found to encapsulate the majority of the similar test data from Eldrup et al. [2022]. Furthermore, the scatter seemed to cover the influence of roughness for nearly all armour unit types in EurOtop [2018]. The associated data analysis concluded that applying $\gamma_f = 0.55$ for impermeable cores in the case of two layered rock armoured breakwaters results in an overestimation of the wave overtopping when used in correlation with the improved guidelines of Eldrup et al. [2022]. The final conclusion of the data analysis was a recommendation to remove the differentiation in γ_f between permeable and impermeable cores. Instead, it was suggested to apply a common value of $\gamma_f = 0.40$, regardless of core permeability.

A numerical model based on computational fluid dynamics was developed to support the empirical data. The model used the wavemaker signal to reproduce the wave trains from regular wave trains sampled in the physical wave flume. The results of the numerical model indicated that layer composition A ($P = 0.10$) and E ($P = 0.50$) may form an upper and lower bound for wave overtopping. The results were, however, limited in describing any correlation between the wave overtopping and the permeability of the core or in displaying a reliable dependency of wave overtopping on wave steepness'.

Bibliography

Aalborg University, 2023a. Aalborg University. *AwaSys7*, 2023a. URL `https://www.hydrosoft.civil.aau.dk/awasys/`.

Aalborg University, 2023b. Aalborg University. *WaveLab3*, 2023b. URL `https://www.hydrosoft.civil.aau.dk/wavelab`.

Besley, 1999. P Besley. *Wave Overtopping of Seawalls Design and Assessment Manual*, Environment Agency, 1999. URL `https://repository.tudelft.nl/islandora/object/uuid:0cd1c50d-0957-4599-aa37-e6328da73988?collection=research`.

Bruce et al., 2009. T. Bruce, J.W. Van der Meer, L. Franco and J.M. Pearson. *Overtopping performance of different armour units for rubble mound breakwaters.* Coastal Engineering, 56(2), 166–179, 2009. ISSN 0378-3839. doi: https://doi.org/10.1016/j.coastaleng.2008.03.015. URL `https://www.sciencedirect.com/science/article/pii/S0378383908000756`. The CLASH Project.

Burcharth et al., 1999. H. F. Burcharth, Z. Liu and P. Troch. *Scaling of Core Material in Rubble Mound Breakwater Model Tests*, 1999.

CIRIA et al., 2007. CIRIA, CUR and CETMEF. *The Rock Manual: The Use of Rock Hydraulic Engineering.* C683, 1(2), 15–62, 2007.

Dai and Kamel, 1969. Y. B. Dai and A. M. Kamel. *Scale effects tests for rubble-mound breakwaters*, U.S. Army Corps of Engineers, 1969.

De Meyere et al., 2017. Goele De Meyere, Lieselot Vantomme, Koen Van Doorslaer, Andreas Kortenhaus and Peter Troch. *The Influence of Crown Walls on Wave Overtopping over Rubble Mound Structures. Experimental Modelling.*, 2017.

Eldrup and Andersen, 09 2017. Mads Eldrup and Thomas Andersen. *Recalibration of Overtopping Roughness Factors of Different Armour Types*, 2017.

Eldrup and Lykke Andersen, 2019a. Mads Røge Eldrup and Thomas Lykke Andersen. *Estimation of Incident and Reflected Wave Trains in Highly Nonlinear Two-Dimensional Irregular Waves.* Journal of Waterway, Port, Coastal, and Ocean Engineering, 145(1), 2019a. ISSN 0733-950X. doi: 10.1061/(ASCE)WW.1943-5460.0000497.

Eldrup and Lykke Andersen, January 2019b. Mads Røge Eldrup and Thomas Lykke Andersen. *Applicability of Nonlinear Wavemaker Theory.* Journal of Marine

Science and Engineering, 7, 2019b. ISSN 2077-1312. doi: 10.3390/jmse7010014. Special Issue "Selected Papers from Coastlab18 Conference"; Coastlab18 : 7th International Conference on the Application of Physical Modelling in Coastal and Port Engineering and Science ; Conference date: 22-05-2018 Through 26-05-2018.

Eldrup et al., **Dec. 2018**. Mads Røge Eldrup, Thomas Lykke Andersen, Jonas Bjerg Thomsen and Hans Falk Burcharth. *Overtopping on breakwaters with a permeable crest*. Coastal Engineering Proceedings, 1(36), papers.17, 2018. doi: 10.9753/icce.v36.papers.17. URL `https://icce-ojs-tamu.tdl.org/icce/article/view/8333`.

Eldrup et al., **May 2019**. Mads Røge Eldrup, Thomas Lykke Andersen and Hans F. Burcharth. *Stability of Rubble Mound Breakwaters—A Study of the Notional Permeability Factor, Based on Physical Model Tests*. Water, 11(5), 2019. ISSN 2073-4441. doi: 10.3390/w11050934.

Eldrup et al., **September 2022**. Mads Røge Eldrup, Thomas Lykke Andersen, Koen Van Doorslaer and Jentsje Van der Meer. *Improved guidance on roughness and crest width in overtopping of rubble mound structures along EurOtop*. Coastal Engineering, 176, 2022. ISSN 0378-3839. doi: 10.1016/j.coastaleng.2022.104152.

Engelund, **1953**. F. Engelund. *On the Laminar and Turbulent Flows of Ground Water Through Homogenous Sand*. Danish Academy of Technical Sciences, 1953.

EurOtop, **2007**. EurOtop. *Manual on wave overtopping of sea defences and related structures. An overtopping manual largely based on European research, but for worldwide application*, Pullen, T. and Allsop, N.W.H. and Bruce, T. and Kortenhaus, A. and Schüttrumpf, H. and Van der Meer, J.W., 2007. URL `www.overtopping-manual.com`.

EurOtop, **2018**. EurOtop. *Manual on wave overtopping of sea defences and related structures. An overtopping manual largely based on European research, but for worldwide application*, Van der Meer, J.W. and Allsop, N.W.H. and Bruce, T. and De Rouck, J. and Kortenhaus, A. and Pullen, T. and Schüttrumpf, H. and Troch, P. and Zanuttigh, B, 2018. URL `www.overtopping-manual.com`.

EurOtop, **2023**. EurOtop. *EurOtop*, 2023. URL `http://overtopping-manual.com/`. Last accessed 30 of May 2023.

Fuhrman et al., **2006**. David R. Fuhrman, Per A. Madsen and Harry B. Bingham. *Numerical simulation of lowest-order short-crested wave instabilities*. Journal of Fluid Mechanics, 563, 415–441, 2006. doi: 10.1017/S0022112006001236.

G. Jacobsen et al., **2011**. Niels G. Jacobsen, David R. Fuhrman and Jørgen Fredsøe. *A wave generation toolbox for the open-source CFD library: OpenFoam*, 2011.

Gaving, **2022**. Henri P. Gaving. *The Levenberg-Marquardt algorithm for nonlinear least squares curve-fitting problems*, 2022. URL `https://people.duke.edu/~hpgavin/ExperimentalSystems/lm.pdf`.

Geeraerts and Willems, 2004. J Geeraerts and M Willems. *Final report on laboratory measurements on the Ostia case.* CLASH WP4 D35, 2004.

Geeraerts et al., 2009. J. Geeraerts, A. Kortenhaus, J.A. González-Escrivá, J. De Rouck and P. Troch. *Effects of new variables on the overtopping discharge at steep rubble mound breakwaters — The Zeebrugge case.* Coastal Engineering, 56(2), 141–153, 2009. ISSN 0378-3839. doi: https://doi.org/10.1016/j.coastaleng.2008.03.013. URL `https://www.sciencedirect.com/science/article/pii/S0378383908000732`. The CLASH Project.

Jacobsen, 08 2017. Niels Jacobsen. *waves2Foam Manual*, 2017.

Jensen et al., 2014a. Bjarne Jensen, Niels Gjøl Jacobsen and Erik Damgaard Christensen. *Investigations on the porous media equations and resistance coefficients for coastal structures.* Coastal Engineering, 84, 56–72, 2014a. ISSN 0378-3839. doi: 10.1016/j.coastaleng.2013.11.004.

Jensen et al., 2014b. Bjarne Jensen, Niels Gjøl Jacobsen and Erik Damgaard Christensen. *Investigations on the porous media equations and resistance coefficients for coastal structures.* Coastal Engineering, 84, 56–72, 2014b. ISSN 0378-3839. doi: https://doi.org/10.1016/j.coastaleng.2013.11.004. URL `https://www.sciencedirect.com/science/article/pii/S0378383913001816`.

Lowe, 1991. J.P. Lowe. *Report EX2310*, 1991.

Lykke Andersen, 2006. Thomas Lykke Andersen. *Hydraulic Response of Rubble Mound Breakwaters: scale effects - berm breakwaters*, 2006. PDF of Ph.D Thesis for print: 253 pp. Appendix A-H is also published on a CD : available in the institutes reference library.

Lykke Andersen et al., 2016. Thomas Lykke Andersen, M. Clavero, Peter Bak Frigaard, M. Losada and J. I. Puyol. *A new active absorption system and its performance to linear and non-linear waves.* Coastal Engineering, 114(August 2016), 47–60, 2016. ISSN 0378-3839. doi: 10.1016/j.coastaleng.2016.04.010.

Muttray et al., 01 2006. Markus Muttray, Hocine Oumeraci and Erik ten Oever. *Wave reflection and wave run-up at rubble mound breakwaters*, 2006.

Schäffer, 1996. Hemming A. Schäffer. *Second-order wavemaker theory for irregular waves.* Ocean Engineering, 23(1), 47–88, 1996. ISSN 0029-8018. doi: https://doi.org/10.1016/0029-8018(95)00013-B. URL `https://www.sciencedirect.com/science/article/pii/002980189500013B`.

USACE, 2002. USACE. *COASTAL ENGINEERING MANUAL*, U.S. Army Corps of Engineers, 2002.

Van der Meer, 1988. J.W. Van der Meer. *Deterministic and Probabilistic Design of Breakwater Armor Layers.* Journal of Waterway Port Coastal and Ocean Engineering-asce, 114, 66–80, 1988.

Van der Meer, 1988. J.W Van der Meer. *Rock slopes and gravel beaches under wave attack*, 1988.

van Gent, 1995. Marcel R.A. van Gent. *Wave Interaction with Permeable Coastal Structures*. International Journal of Rock Mechanics and Mining Sciences & Geomechanics Abstracts, 6, 1995.

wiki, 2023. OpenFOAM wiki. *OpenFOAM, DarcyForchheimer Class Reference*, 2023. URL https://openfoamwiki.net/index.php/DarcyForchheimer. Last accessed 06 of June 2023.

Zhang et al., 2007. Haiwen Zhang, Hemming A. Schäffer and Kim P. Jakobsen. *Deterministic combination of numerical and physical coastal wave models*. Coastal Engineering, 54(2), 171–186, 2007. ISSN 0378-3839. doi: https://doi.org/10.1016/j.coastaleng.2006.08.009. URL https://www.sciencedirect.com/science/article/pii/S0378383906001268.

Estimation of the notional permeability factor A

The stability formulae by Van der Meer [1988] features the notional permeability factor P. It describes the influence of the permeability of the layer composition of the rubble mound breakwater. The selection of P has previously been left to the judgement of the engineer, guided by the tested layer compositions of Van der Meer [1988]. Eldrup et al. [2019] established an empirical formula for estimating P based on tests of several different layer compositions and data from previous work, such as Van der Meer [1988], covering a wide range of P.

The notional permeability factor P was found to be a function of the material size and distance from the armour surface to the underlying layers. All tests in Eldrup et al. [2019] were conducted with a narrow grading of $D_{n85}/D_{n15} < 2.25$ meaning the influence of a very wide grading is not accounted for. The new formula incorporates the known range of P covered in Van der Meer [1988] with a minimum of 0.1 and a maximum of 0.6. The empirical formula for estimating P is given in Eq. (A.1). The maximum value of Eq. (A.1) is 0.57. However, a comparison of the fitted and estimated P showed a typical deviation of 0.03. [Eldrup et al., 2019, Eq. 7]

$$P = \max \begin{cases} 0.1 \\ 1.72 \cdot k - 1.58 \end{cases} \tag{A.1}$$

Here k is an integration function combining the influence of the relative rock size and relative layer depth through functions f and g respectively. The integration function k is given in Eq. (A.2). [Eldrup et al., 2019, Eq. 5]

$$k = \int_0^{z^*_{max}} f(z^*) \cdot g(z^*) \; dz^* \tag{A.2}$$

Here $z^* = z/D_{n50A}$ describes the relative distance from the armour layer to each layer where z is the distance perpendicular to the front slope. z^*_{max} is the maximum depth of the integration taken as the value of z^* for an impermeable layer, if present, but with a maximum value of 13 in all cases. The functions f and g are provided in Eq. (A.3) and Eq. (A.4) respectively. [Eldrup et al., 2019, Eq. 4]

$$f = 0.79 \cdot \left(1 - \exp\left(-4.1 \cdot \frac{D_{n50,z^*}}{D_{n50A}}\right)\right) \qquad \text{for} \qquad \frac{D_{n85}}{D_{n15}} < 2.5 \tag{A.3}$$

$$g = \exp(-0.62 \cdot z^*) \tag{A.4}$$

Here D_{n50,z^*} is the nominal stone size in the layer at relative depth z^*. The integration function k in Eq. (A.2) can be rewritten into Eq. (A.5) for a composition of N permeable layers. [Eldrup et al., 2019, Eq. 6]

$$k = \sum_{i=1}^{N} \left(0.79 - 0.79 \exp\left(-4.1 \frac{D_{n50,i}}{D_{n50A}}\right)\right) \left(\frac{\exp\left(-0.62 z_1^*\right) - \exp\left(-0.62 z_2^*\right)}{0.62}\right) \quad \text{(A.5)}$$

Here $D_{n50,i}$ is the nominal stone size in layer i. An example showcasing the definitions of Eq. (A.5) is shown in Figure A.1.

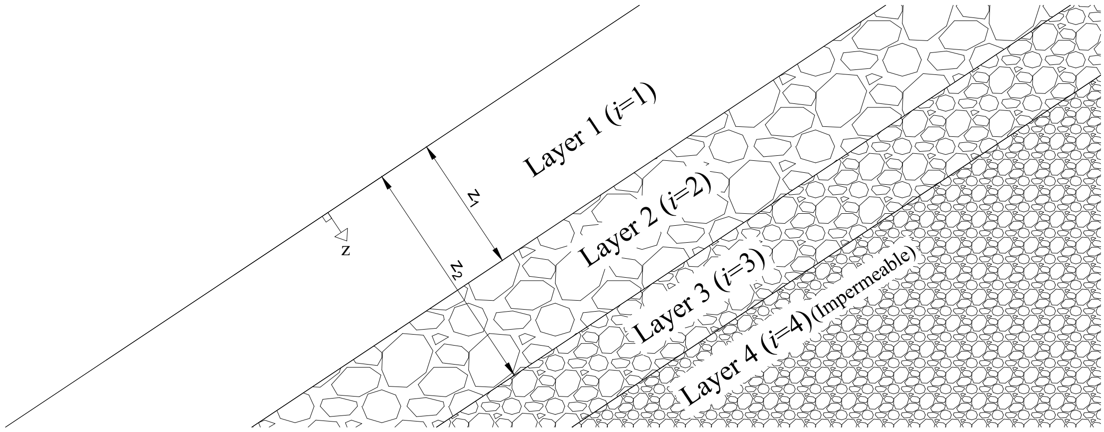

Figure A.1. Sketch of parameter definitions. [Eldrup et al., 2019]

Fitting of influence of roughness factor B

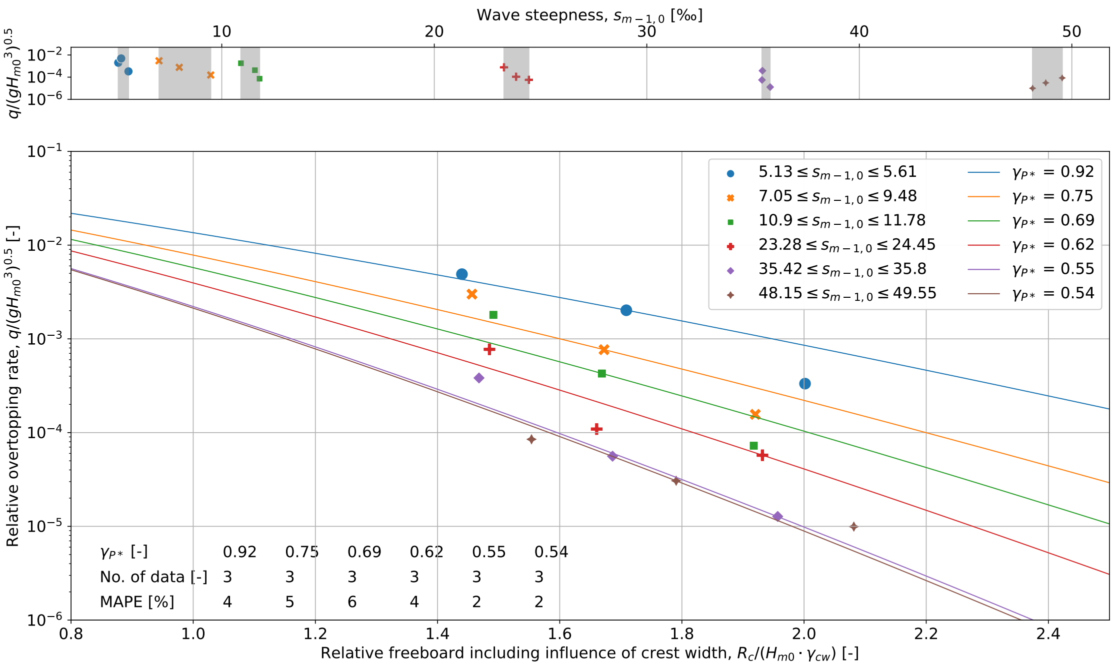

Figure B.1. $P = 0.10, \cot(\alpha) = 1.5, h = 0.480\,\mathrm{m}$, test no. 0

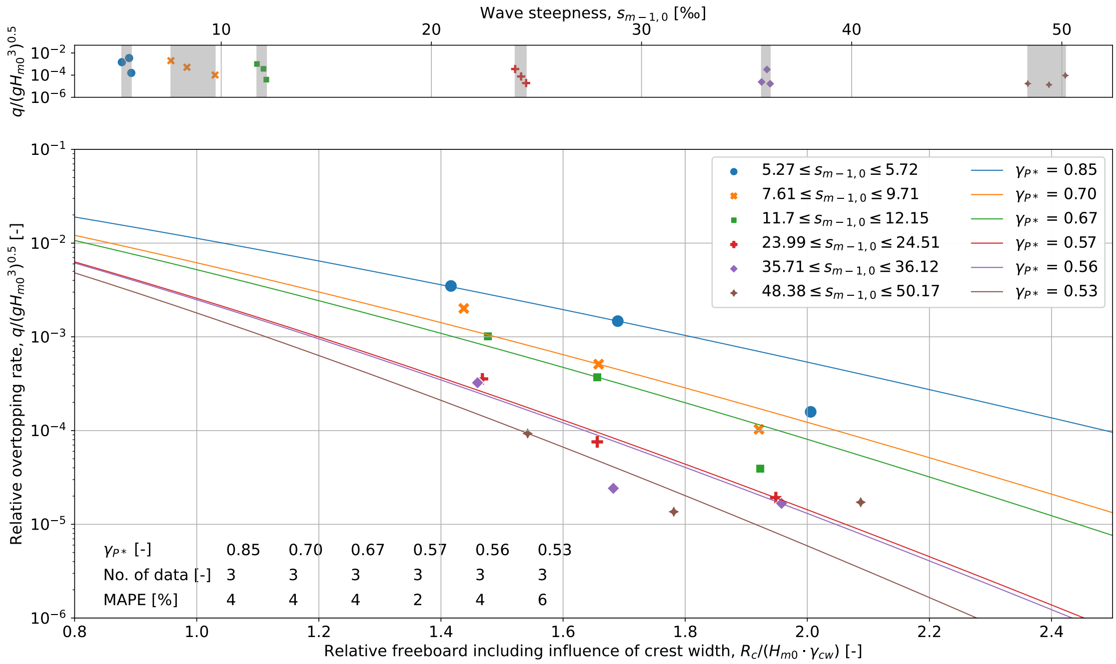

Figure B.2. $P = 0.10, \cot(\alpha) = 1.5, h = 0.480\,\mathrm{m}$, test no. 1

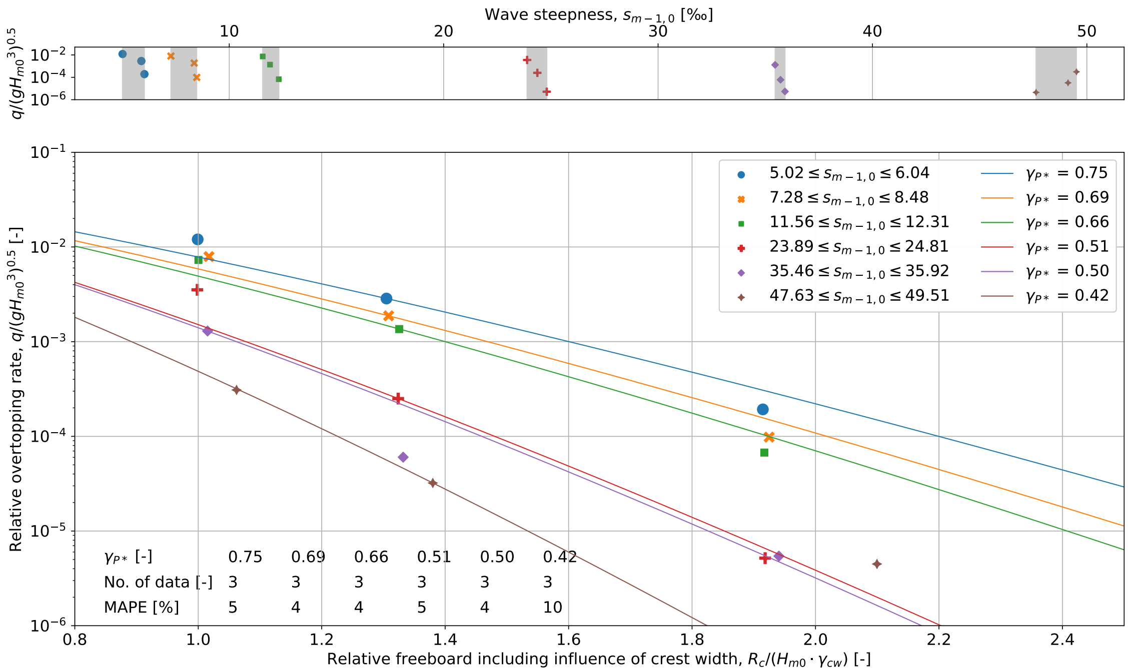

Figure B.3. $P = 0.10, \cot(\alpha) = 1.5, h = 0.522\,\mathrm{m}$, test no. 0

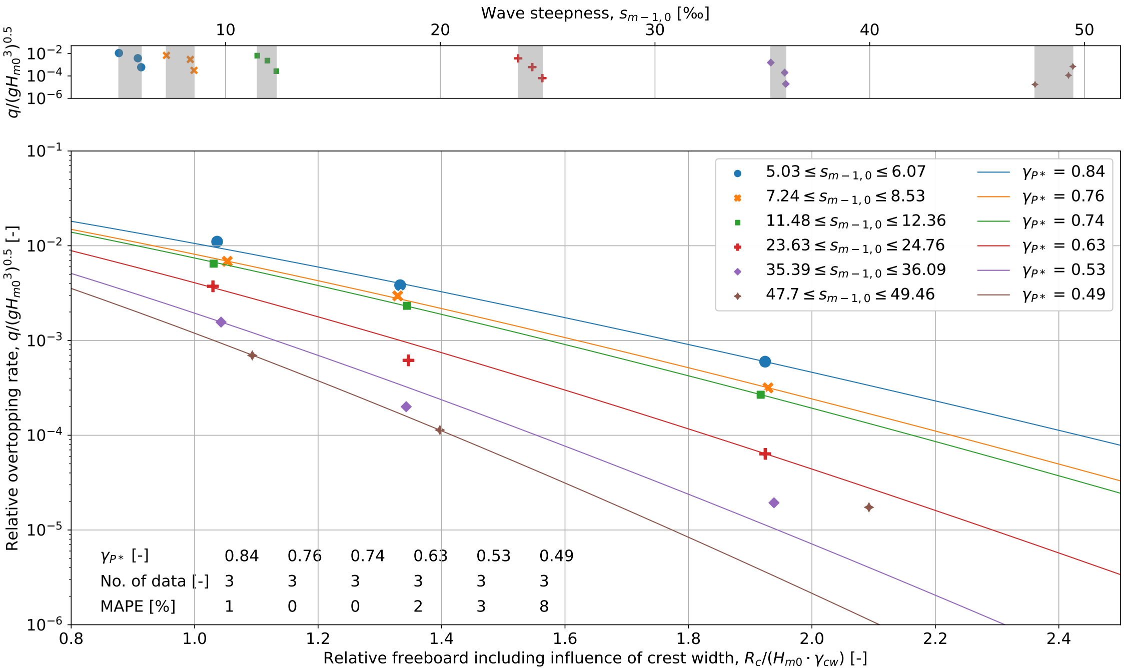

Figure B.4. $P = 0.10, \cot(\alpha) = 1.5, h = 0.522\,\text{m}$, test no. 1

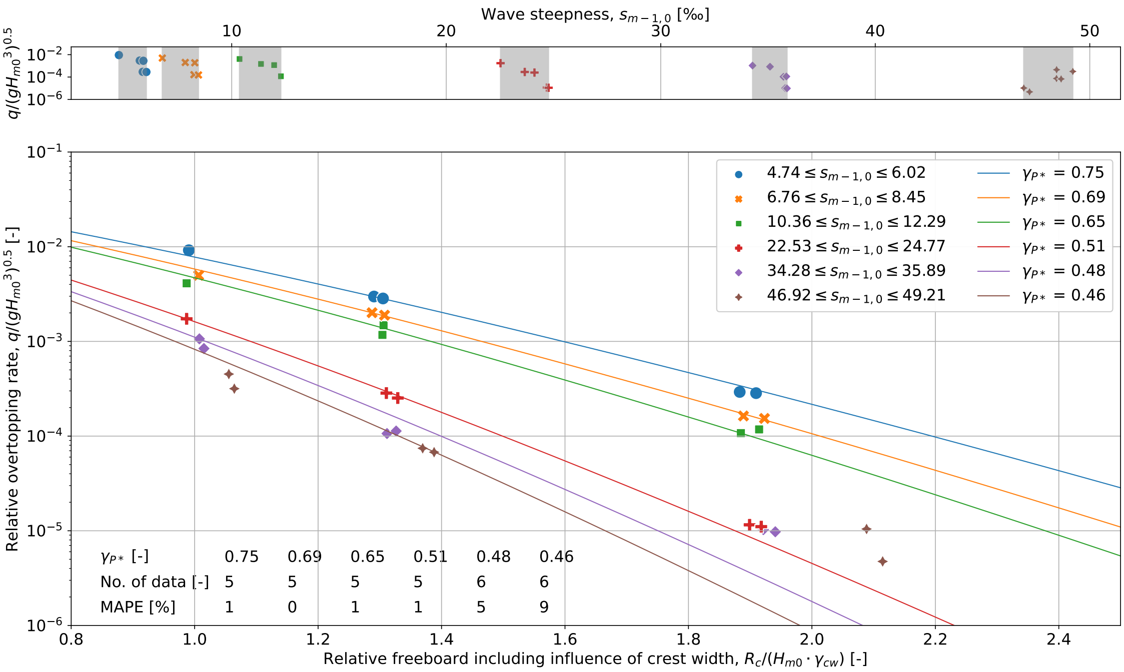

Figure B.5. $P = 0.10, \cot(\alpha) = 1.5, h = 0.522\,\text{m}$, test no. 2

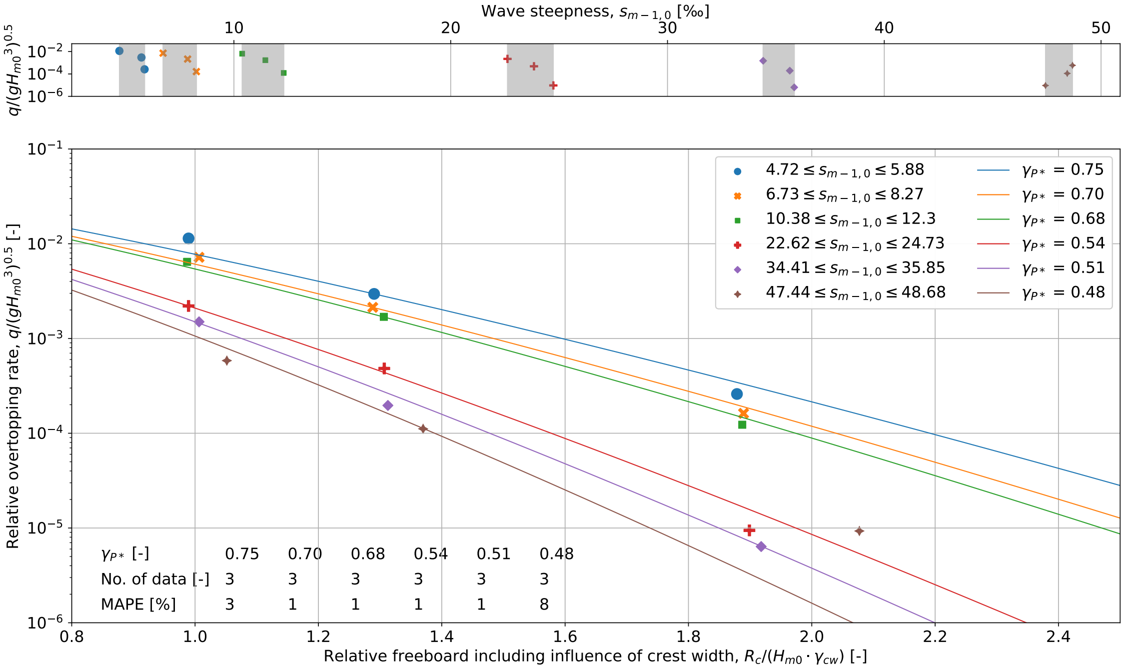

Figure B.6. $P = 0.10, \cot(\alpha) = 1.5, h = 0.522\,\mathrm{m}$, test no. 3

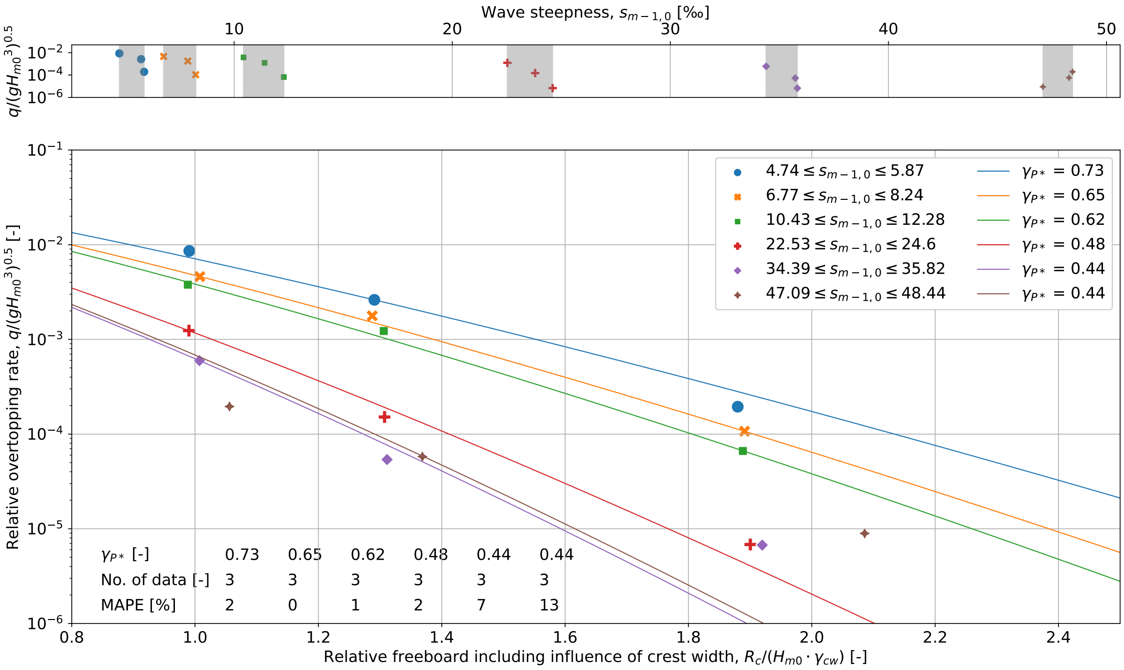

Figure B.7. $P = 0.10, \cot(\alpha) = 1.5, h = 0.522\,\mathrm{m}$, test no. 4

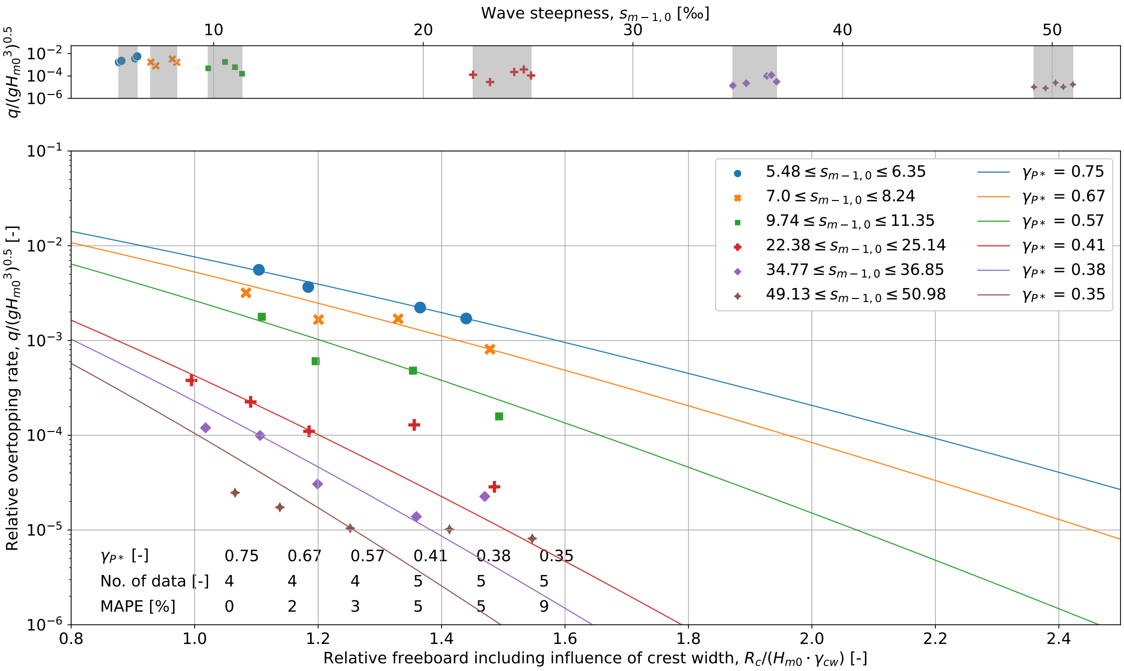

Figure B.8. $P = 0.10, \cot(\alpha) = 3.0, h = 0.480\,\mathrm{m}$, test no. 0

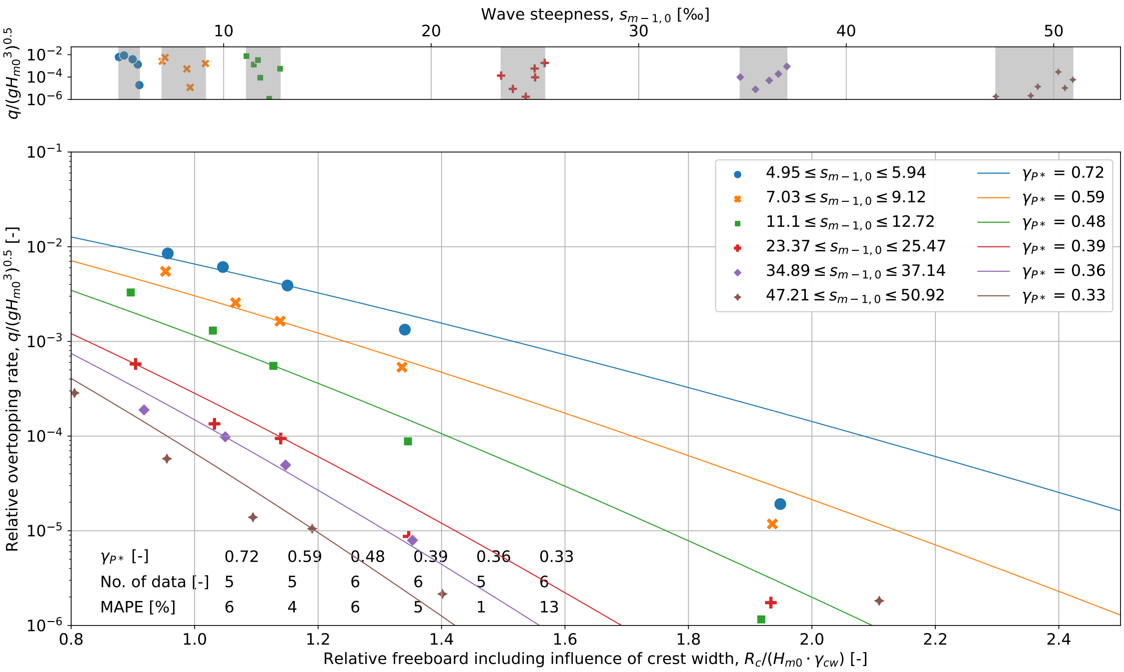

Figure B.9. $P = 0.10, \cot(\alpha) = 3.0, h = 0.522\,\mathrm{m}$, test no. 0

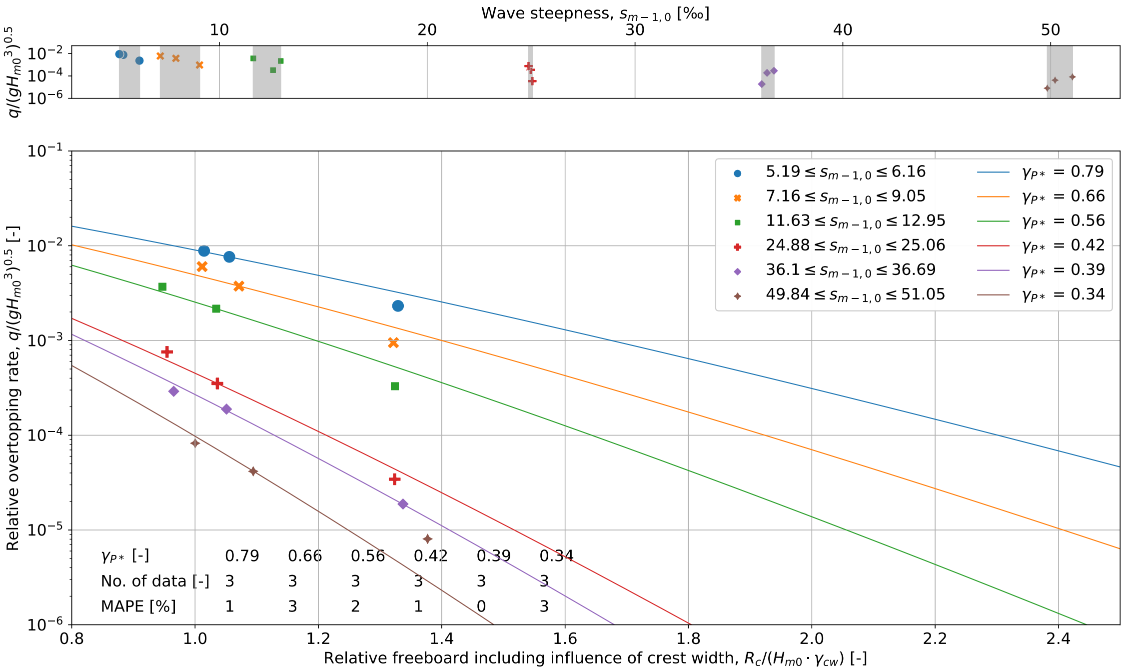

Figure B.10. $P = 0.10, \cot(\alpha) = 3.0, h = 0.522\,\mathrm{m}$, test no. 1

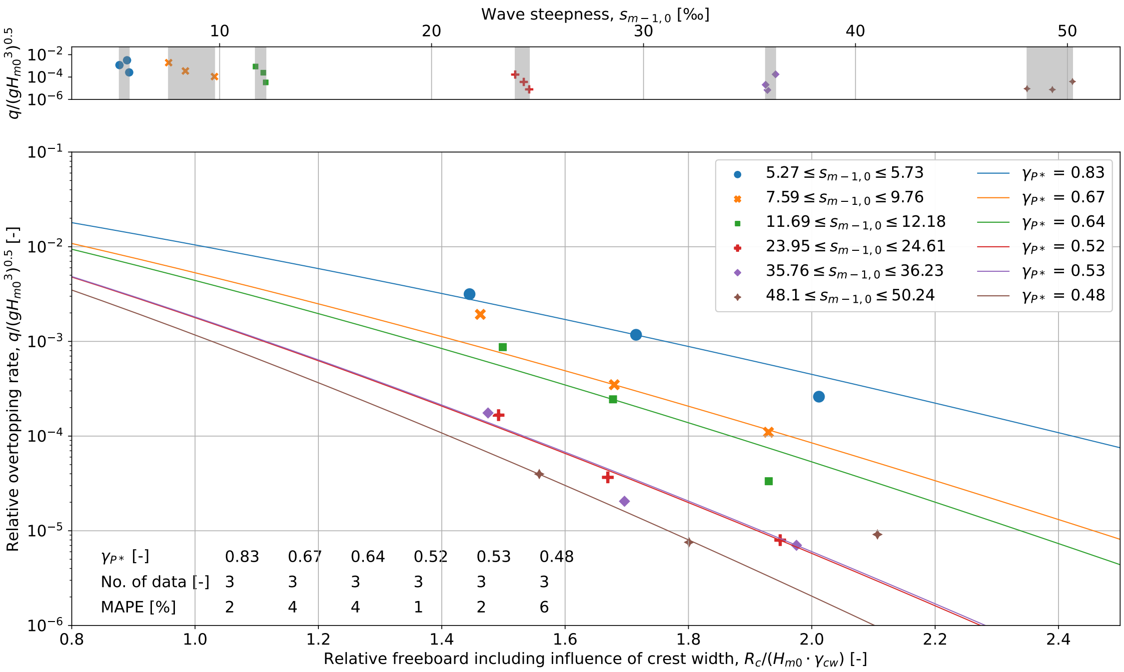

Figure B.11. $P = 0.24, \cot(\alpha) = 1.5, h = 0.480\,\mathrm{m}$, test no. 0

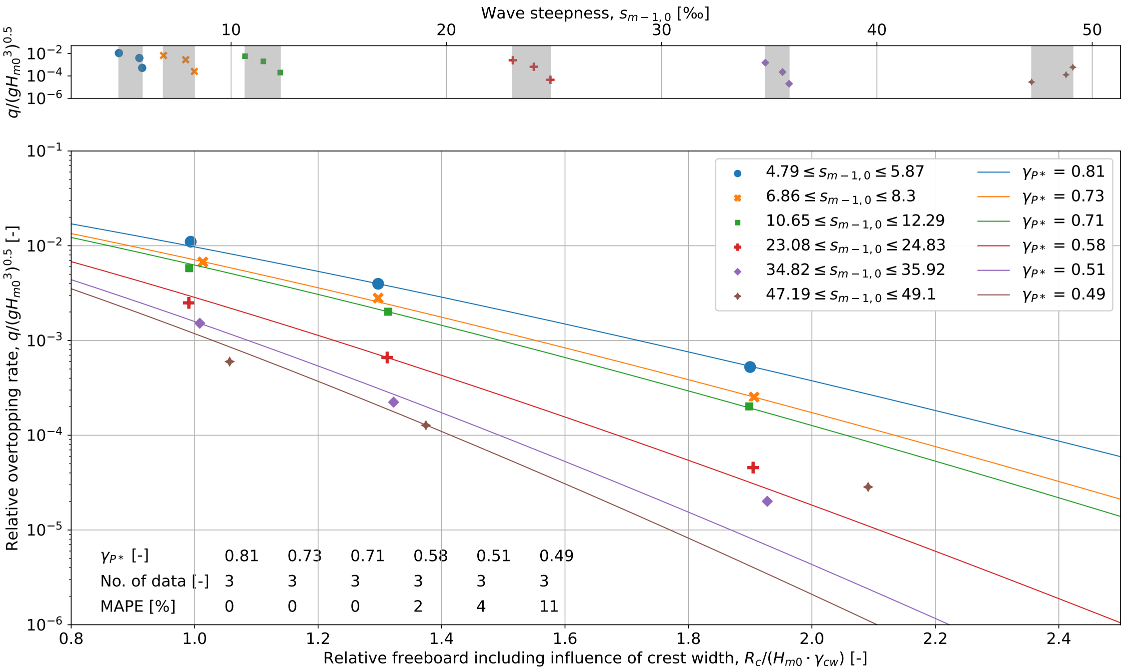

Figure B.12. $P = 0.24, \cot(\alpha) = 1.5, h = 0.522\,\text{m}$, test no. 0

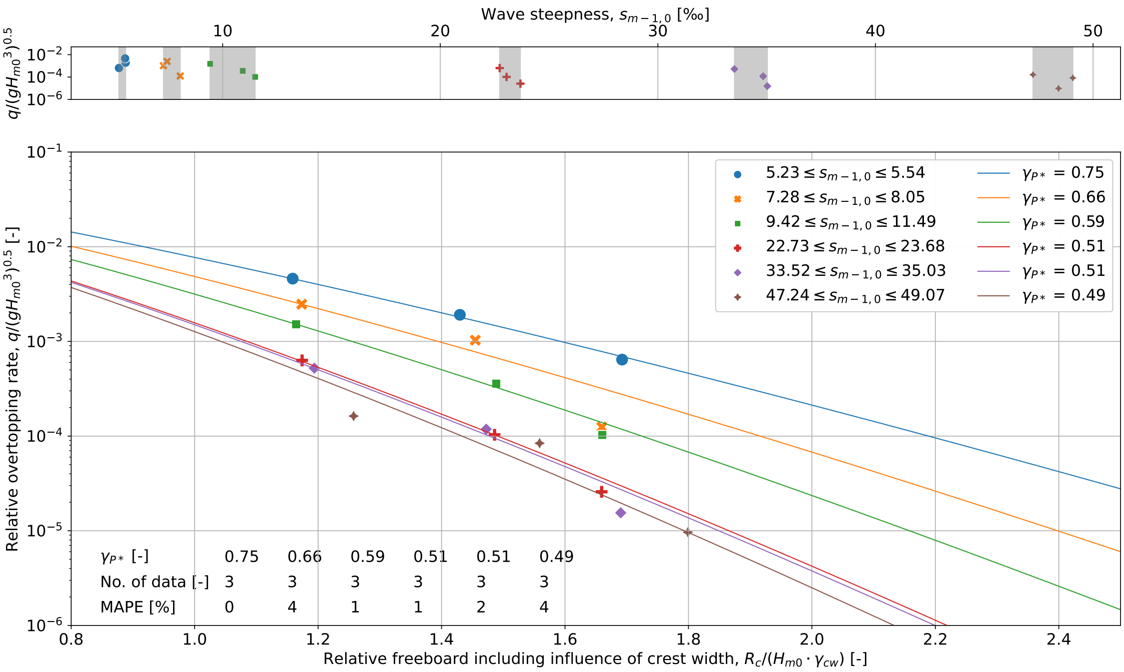

Figure B.13. $P = 0.38, \cot(\alpha) = 1.5, h = 0.480\,\text{m}$, test no. 0

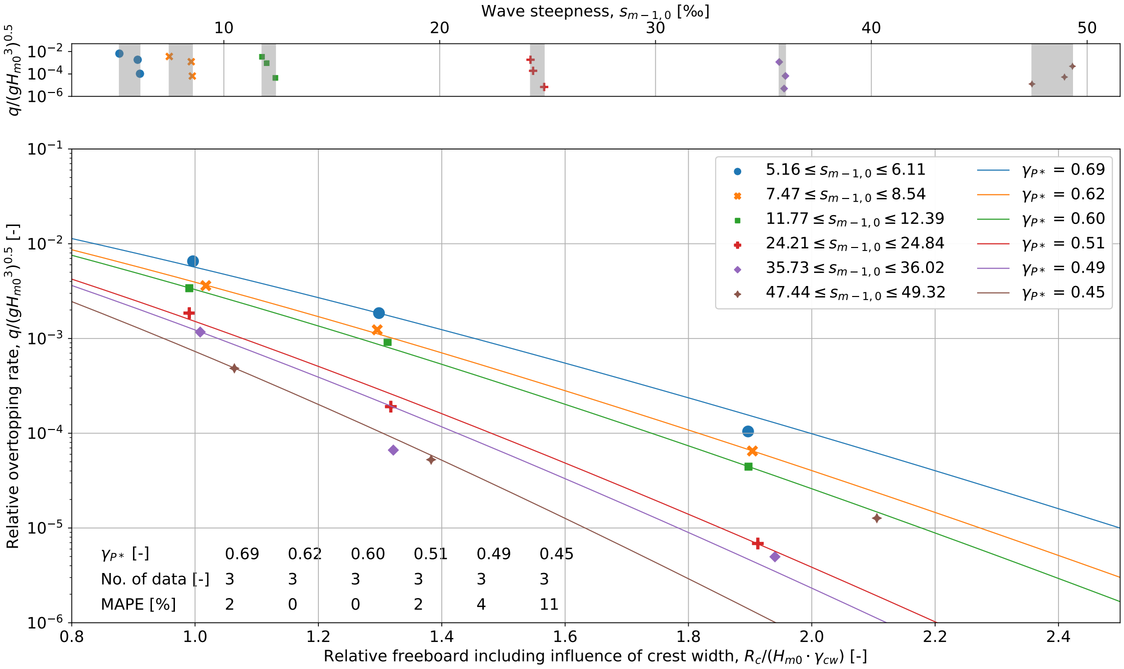

Figure B.14. $P = 0.38, \cot(\alpha) = 1.5, h = 0.522\,\mathrm{m}$, test no. 0

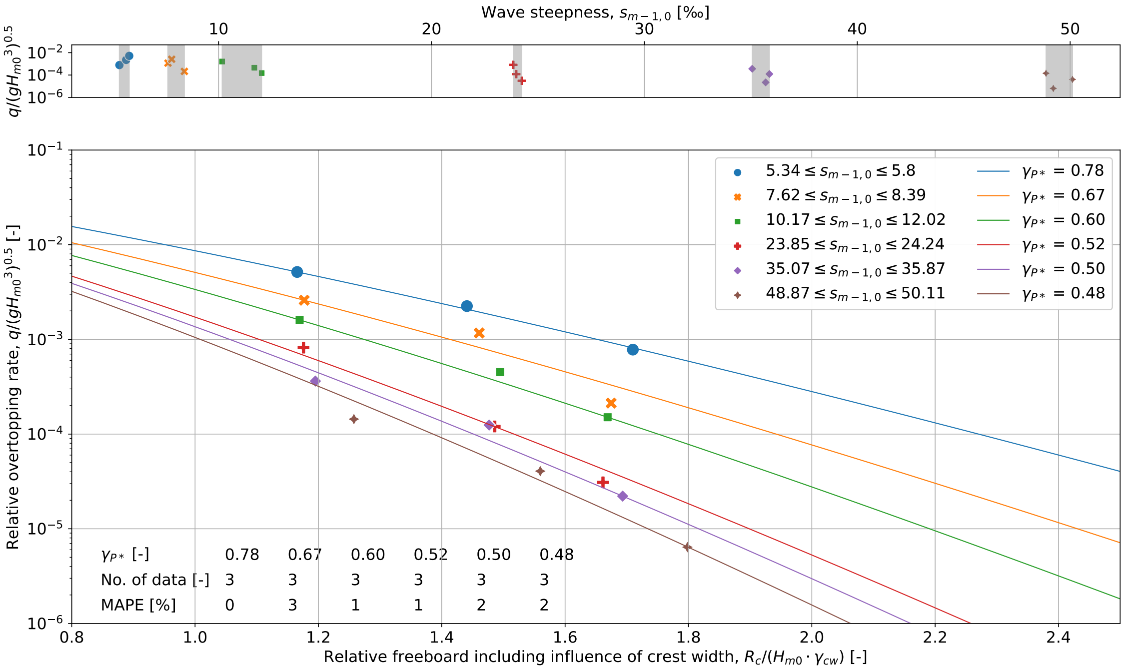

Figure B.15. $P = 0.39, \cot(\alpha) = 1.5, h = 0.480\,\mathrm{m}$, test no. 0

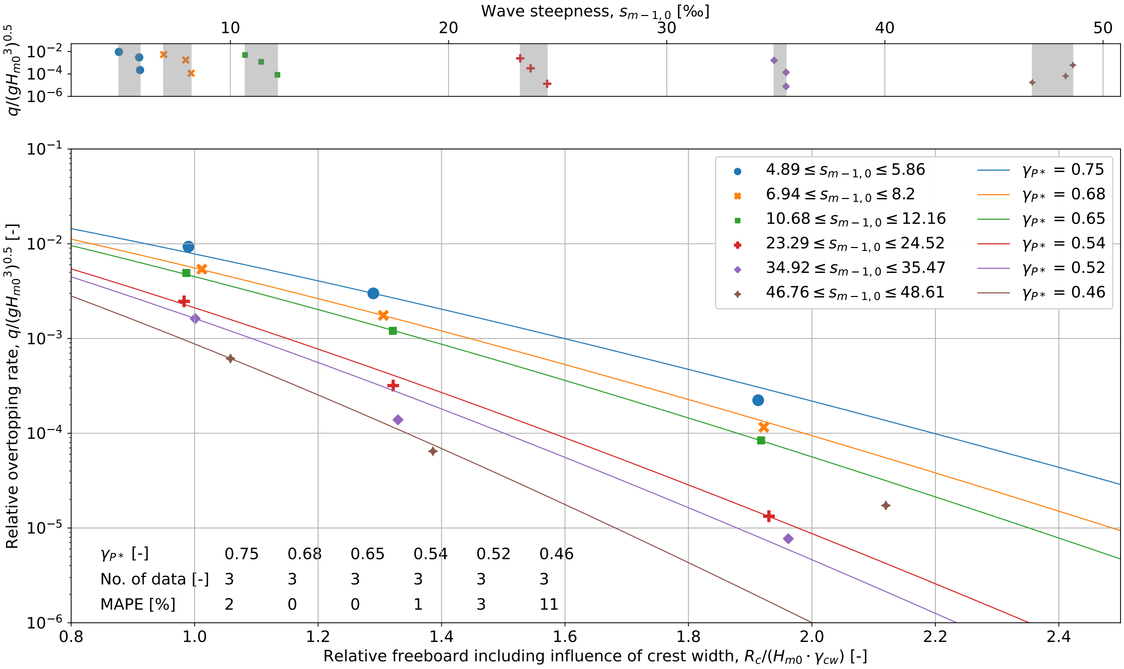

Figure B.16. $P = 0.39, \cot(\alpha) = 1.5, h = 0.522\,\mathrm{m}$, test no. 0

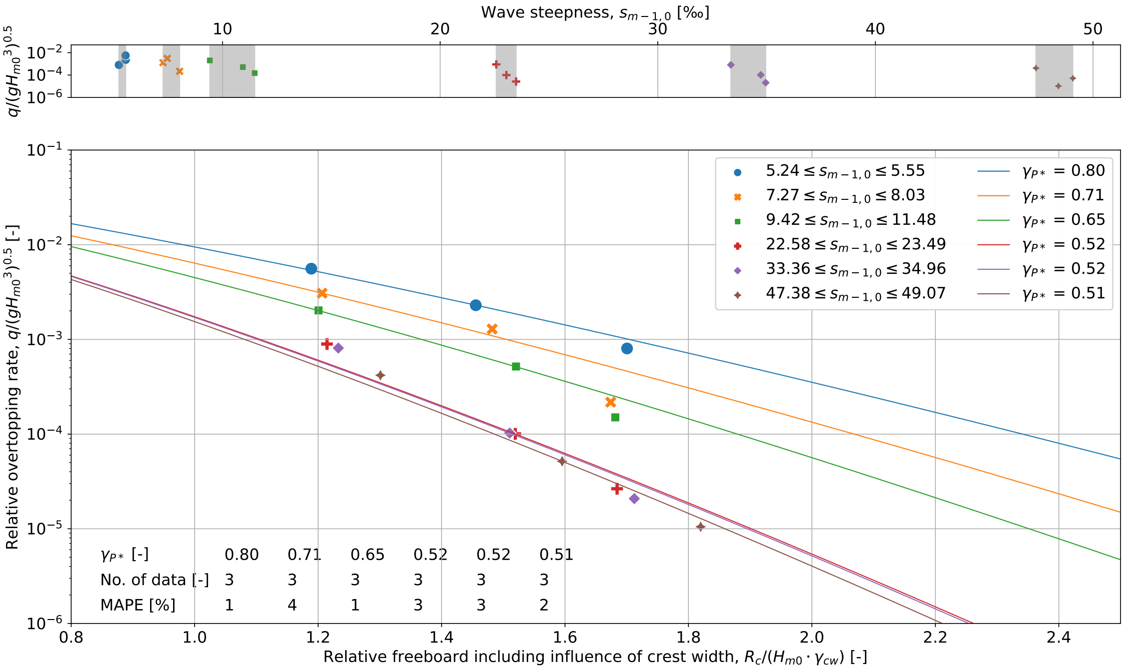

Figure B.17. $P = 0.50, \cot(\alpha) = 1.5, h = 0.480\,\mathrm{m}$, test no. 0

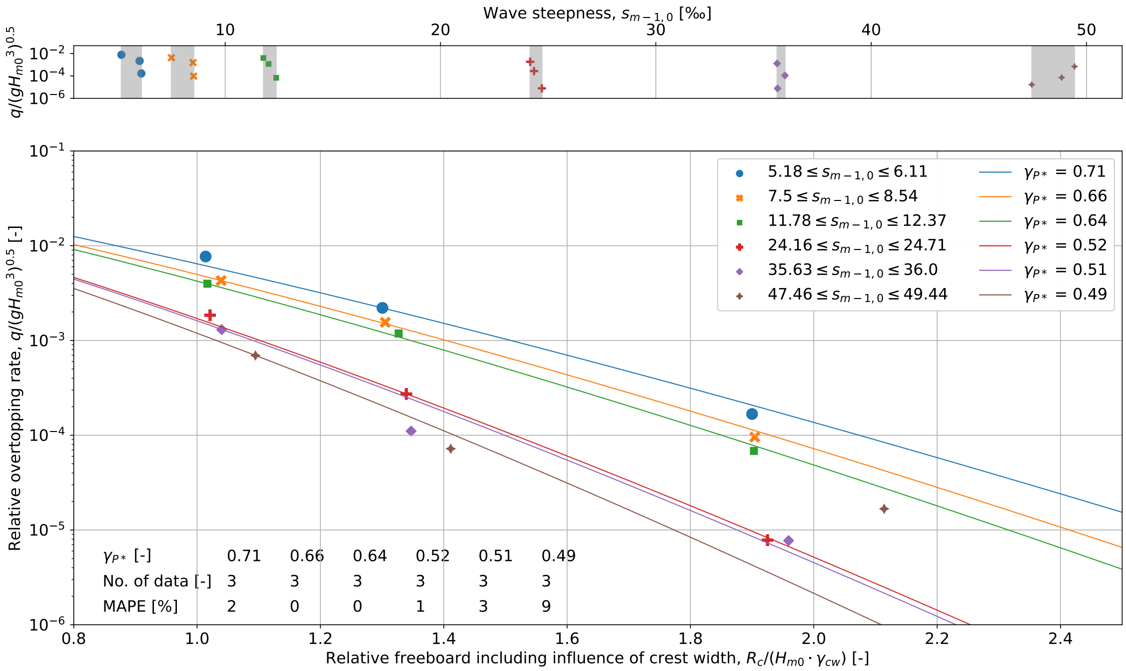

Figure B.18. $P = 0.50, \cot(\alpha) = 1.5, h = 0.522\,\mathrm{m}$, test no. 0

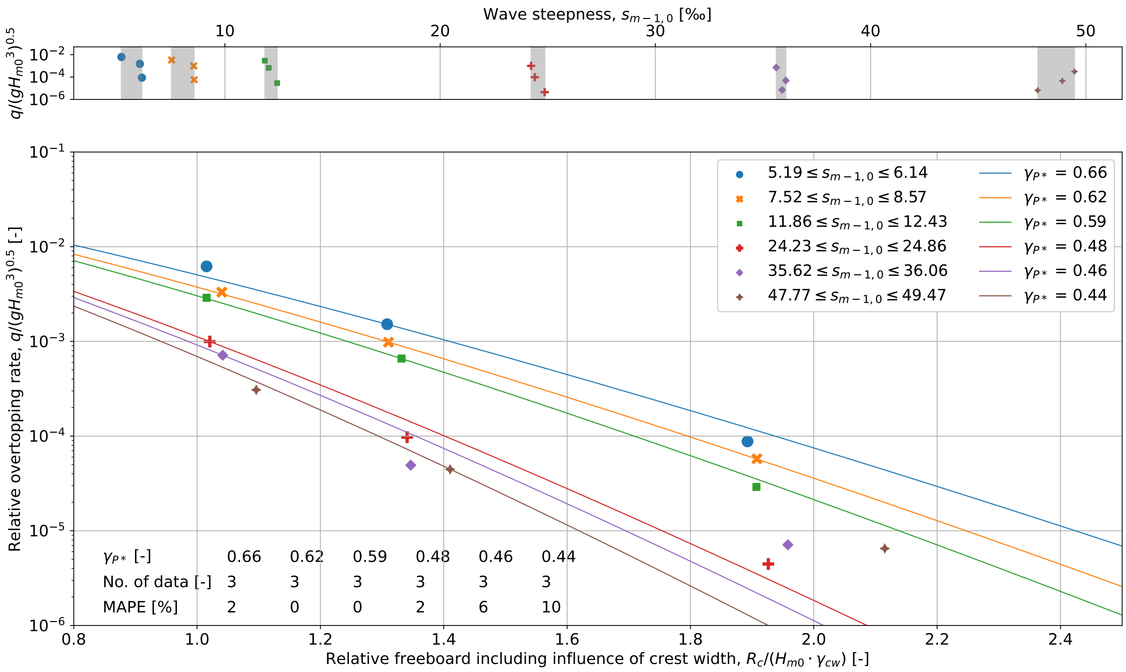

Figure B.19. $P = 0.50, \cot(\alpha) = 1.5, h = 0.522\,\mathrm{m}$, test no. 1

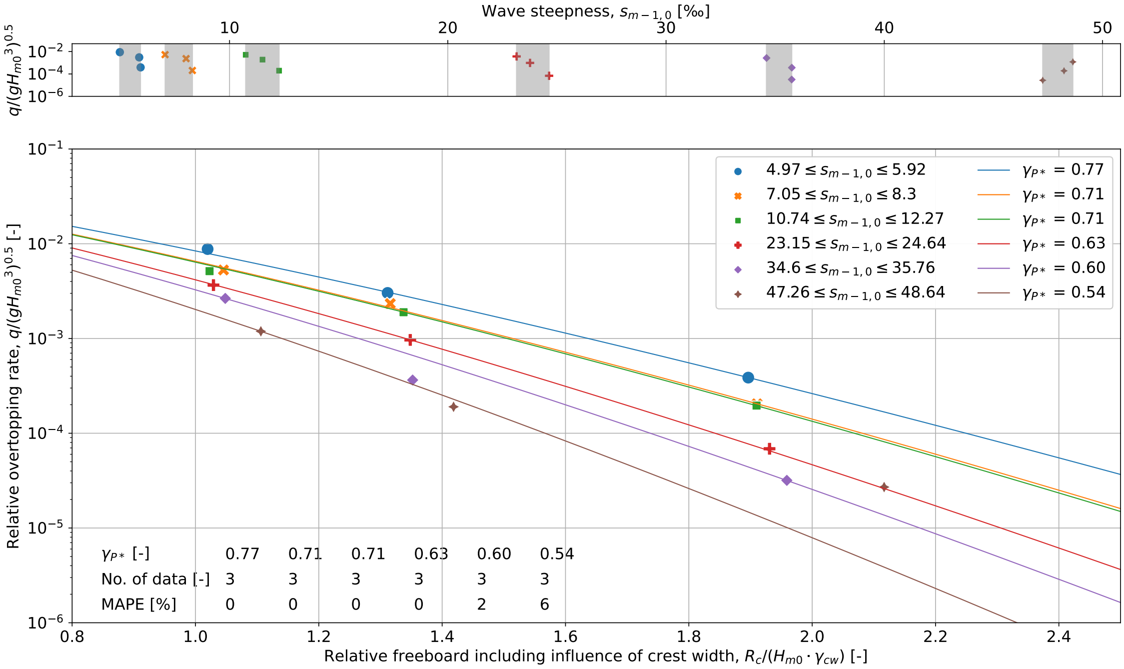

Figure B.20. $P = 0.50, \cot(\alpha) = 1.5, h = 0.522\,\text{m}$, test no. 2

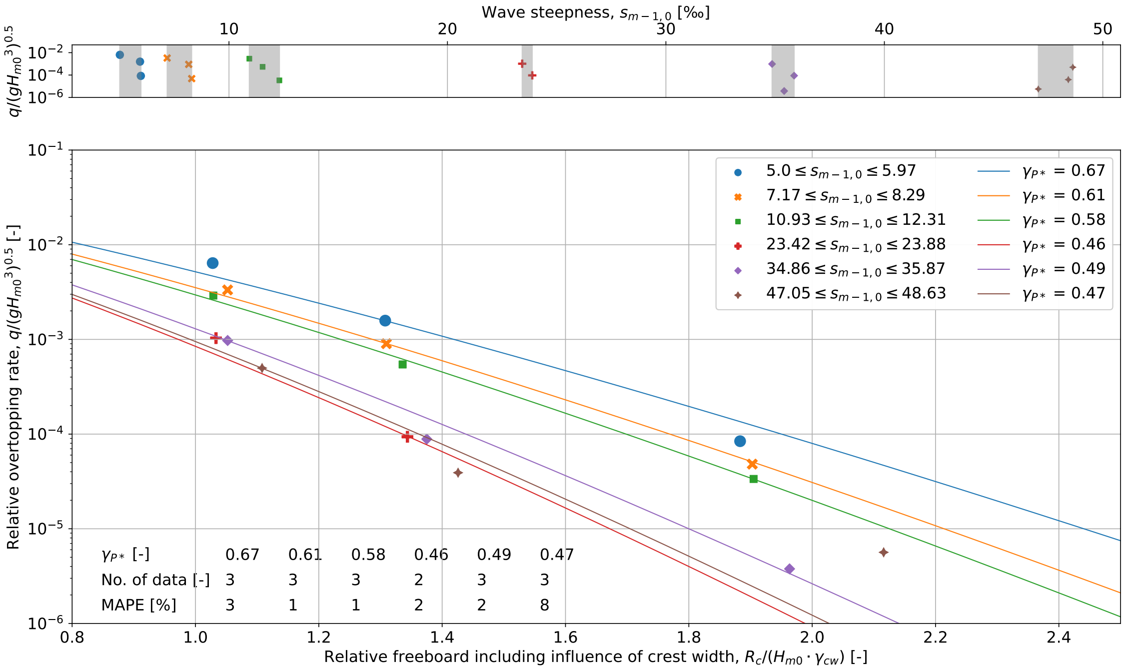

Figure B.21. $P = 0.50, \cot(\alpha) = 1.5, h = 0.522\,\text{m}$, test no. 3

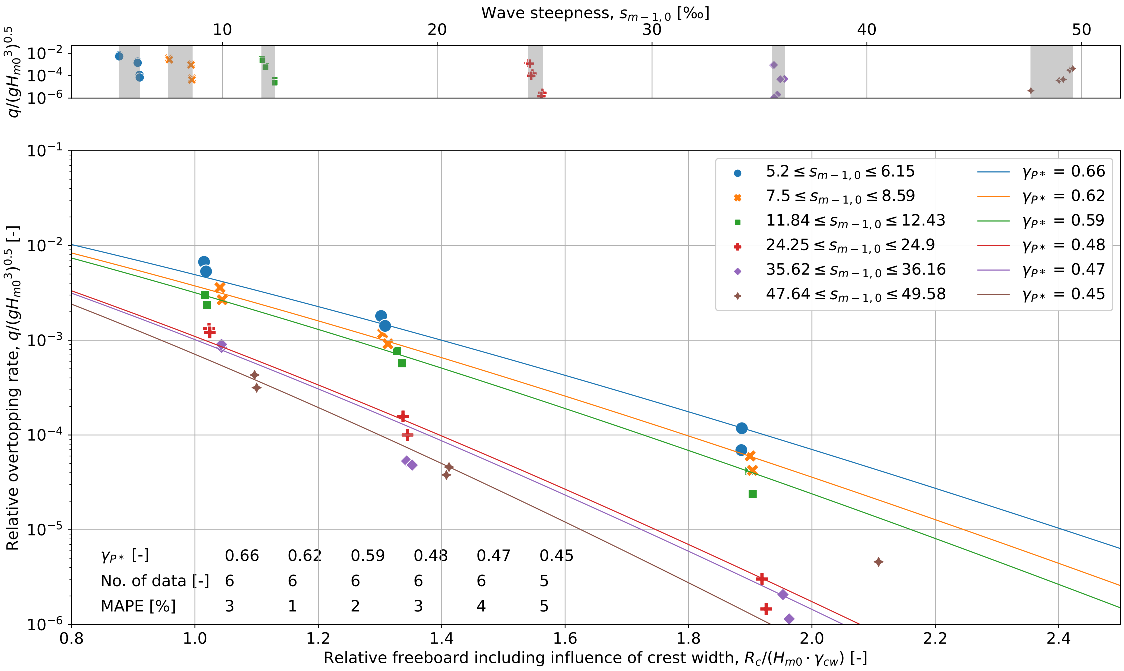

Figure B.22. $P = 0.50, \cot(\alpha) = 1.5, h = 0.522\,\text{m}$, test no. 4

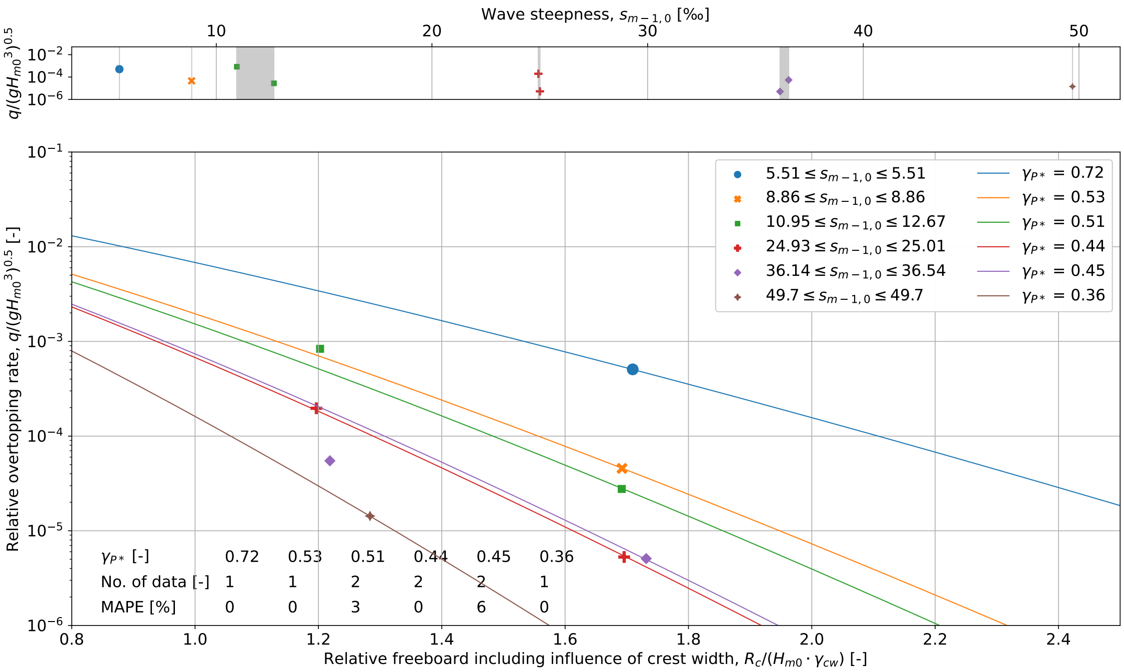

Figure B.23. $P = 0.50, \cot(\alpha) = 3.0, h = 0.480\,\text{m}$, test no. 0

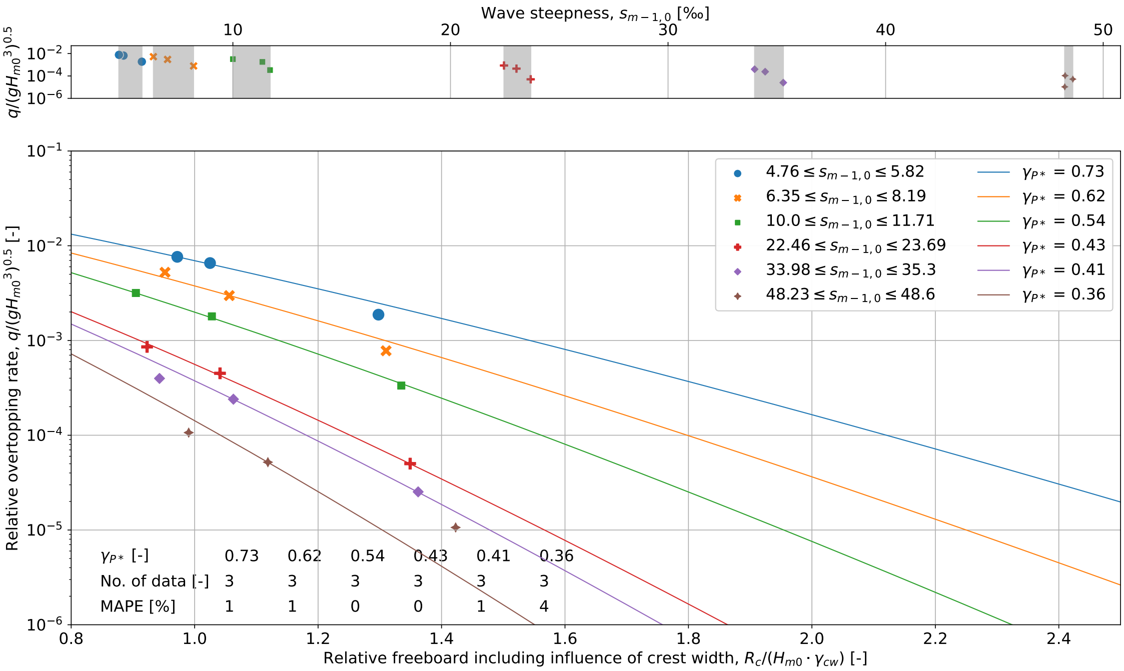

Figure B.24. $P = 0.50, \cot(\alpha) = 3.0, h = 0.522\,\mathrm{m}$, test no. 0

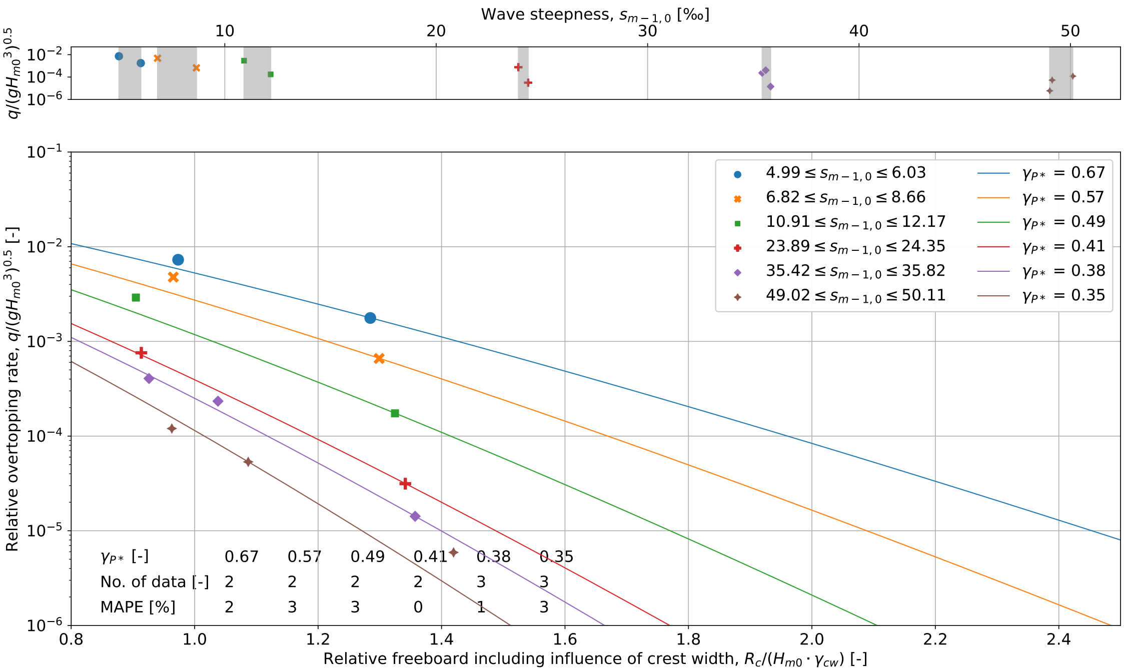

Figure B.25. $P = 0.50, \cot(\alpha) = 3.0, h = 0.522\,\mathrm{m}$, test no. 1

Hydraulic resistance C

The inclusion of a porous structure in the numerical model requires the specification of resistance coefficients for the chosen resistance formulation. The chosen resistance formulation is the *nativeOF* where porous media is modelled by use of the Darcy-Forchheimer porosity model given by Eq. (C.1). [wiki, 2023]

$$S = (\mu d + \frac{1}{2}\rho|u|f)u \tag{C.1}$$

Here S is the source term, U is the discharge velocity, μ is the dynamic viscosity of the fluid, ρ is the density of the fluid, d is the Darcy coefficient and f is the Fochheimer coefficient. The laminar d and turbulent f resistance coefficients are incorporated as vectors, meaning that the coefficients are directionally dependent. However, for a homogeneous media, the resistance is the same in all directions.

The source term S can be expressed as a pressure gradient ∇p whereby Eq. (C.1) is rewritten into Eq. (C.2).

$$\nabla p = \mu d u + \frac{1}{2}\rho f u^2 \tag{C.2}$$

From Eq. (C.2) the resistance coefficients d and f can be derived from the quadratic formulation for the Darcy-Forchheimer expression in Eq. (C.3).

$$\frac{\Delta p}{\Delta x} = \nabla p = Au + Bu^2 \tag{C.3}$$

Where Δp is the pressure drop, Δx is the length of the porous zone and coefficients A and B can be determined from the curve-fitting of a second-order polynomial. Comparison of Eq. (C.1) and Eq. (C.3) coefficients d and f resolves as stated in Eq. (C.4) and Eq. (C.5) respectively.

$$A = \mu d \qquad \Leftrightarrow \qquad d = \frac{A}{\mu} \tag{C.4}$$

$$B = \frac{1}{2}\rho f \qquad \Leftrightarrow \qquad f = 2\frac{B}{\rho} \tag{C.5}$$

The resistance formulation in Jacobsen [2017] requires the specification of these parameters, as well as an added mass coefficient, incorporating the inertia term. The added mass coefficient is presented in Eq. (C.6). [Jacobsen, 2017, Eq. 2.14]

$$C_m = \gamma_p \frac{1-n}{n} \tag{C.6}$$

Where $\gamma_p = 0.34$ is a closure coefficient making C_m solely dependent on the porosity n of the material. Estimation of the resistance coefficients is done by measurements of pressure drop Δp over the length of a tube Δx.

The purpose of these tests is to obtain the permeability parameters for describing the porous flow inside the rubble mound breakwater for the numerical model. The permeability of the rock material was measured using the setup shown in Figure C.1.

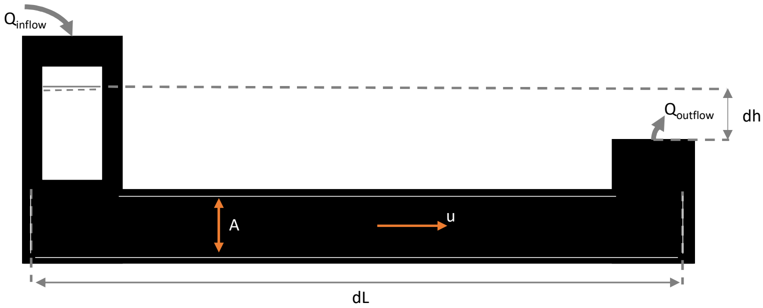

Figure C.1. Test setup for measuring material permeability.

The difference between two hydraulic heads of the inlet and outlet dh used to determine the hydraulic gradient $I = dh/dL$ and pressured drop $\Delta p = \rho_{water} \cdot g \cdot dh$ was measured using a ruler, as shown in Figure C.2c. The discharge velocity was determined based on the cross-section of the tube and the flow Q applied. The tube was lined with a sponge layer on the inside to reduce any boundary effects. The flow Q was measured using a flow meter shown in Figure C.2a and C.2c. The porosity n was determined by measuring the volume of water added to a known volume of rock material, as shown in Figure C.2d.

(a) Setup of permeability tests.

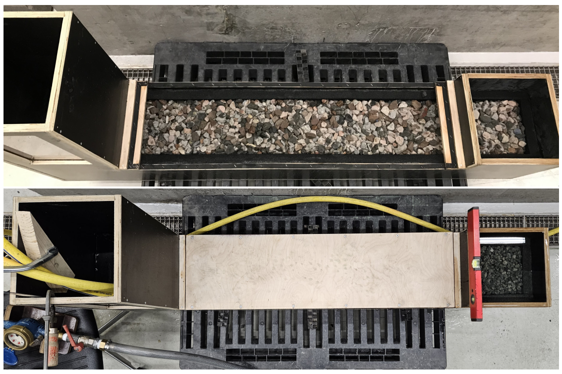

(b) Tube lined with Class III rocks.

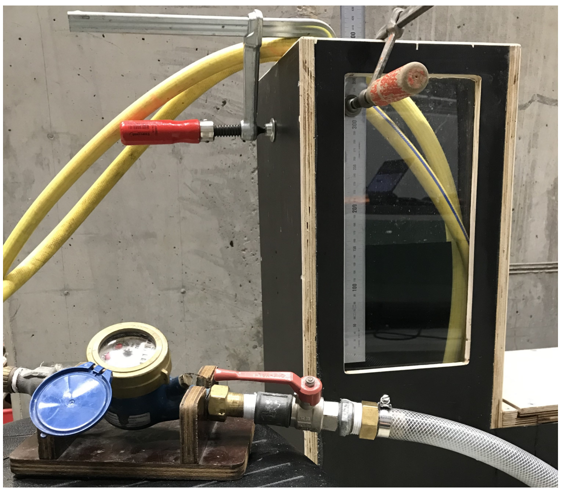

(c) Reading of flow Q and pressure drop dh.

(d) Measuring porosity for Class I rocks.

Figure C.2. Setup for measuring permeability coefficients for each rock material.

Readings of the hydraulic gradient I and the discharge velocity u are shown in Figure C.3 along with a fitted 2^{nd} order polynomial.

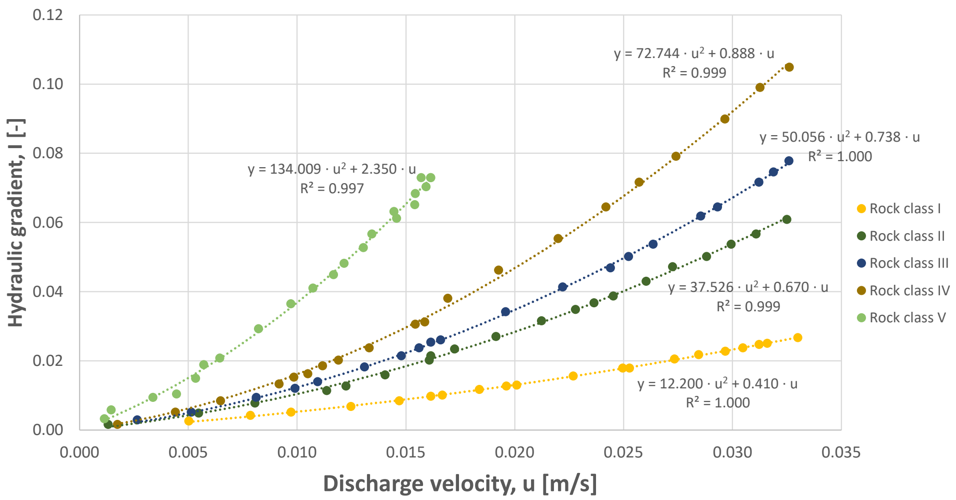

Figure C.3. Measured test data for each rock material with fitted 2^{nd} order polynomial.

The resistance coefficients A and B are determined by fitting a 2^{nd} order polynomial to the readings of the pressure gradient $\nabla p = \frac{\Delta p}{\Delta x}$ and the discharge velocity u. Readings of the pressure gradient ∇p and the discharge velocity u are shown in Figure C.3 along with the fitted 2^{nd} order polynomial.

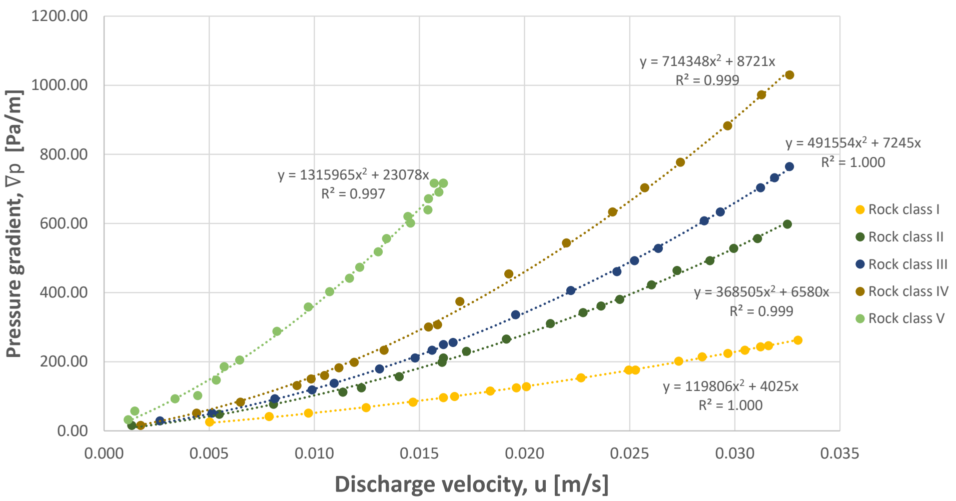

Figure C.4. Measurements of ∇p and u for each rock material with fitted 2^{nd} order polynomial.

The permeability and porosity parameters are listed in Table C.1 based on the fitted polynomial in Figure C.4.

Table C.1. Material and permeability parameters for each rock material.

	Median weight	Nominal diameter	Grading	Mass density	Darcy coef.	Forchheimer coef.	Porosity
Rock class	W_{n50} [g]	D_{n50} [m]	D_{n85}/D_{n15} [-]	ρ [kg/m^3]	d [1/m^2]	f [1/m]	n [-]
I	221.00	0.044	1.296	2620	4.02×10^6	239.61	0.43
II	30.00	0.022	1.115	2658	6.57×10^6	737.01	0.43
III	9.00	0.015	1.357	2768	7.23×10^6	983.11	0.43
IV	5.15	0.012	1.298	2713	8.70×10^6	1428.70	0.41
V	0.65	0.006	1.360	2936	23.03×10^6	2631.93	0.39

Uncertainties of empirical data D

This sections seeks to cover the main project specific uncertainties, regarding the significant wave height, H_{m0} and the freeboard height, R_c. Due to some challenges, some of the used laboratory equipment, may have produced more uncertainties and therefore it is vital to disclose these and asses the impact on the final conclusion.

D.1 Significant wave height

The resistant type wave gauges were used to separate incident waves from the reflected and therefore acts as a crucial role in determining the significant wave height H_{m0}. As mentioned in chapter 3.1.2, a build-up of limescale and dirt on these gauges, could have induced falsely measured H_{m0}. Therefore, this section seeks to cover the uncertainty in the measured significant wave heights.

The wave gauges measures the resistance in the water between two parallel rods, and by the use of a calibration function converts the measured signal in volts into a surface elevation in meters. The used calibration functions follows a linear relation between surface elevation and measured voltage as shown in (D.1).

$$\eta = a \cdot V + b \tag{D.1}$$

where η is the surface elevation, V is the measured resistance in voltage, a is the calibration coefficient and b is the measured offset. The coefficient a and offset b were determined by a 5-point calibration, where the resistance of the water would be measured at 5 different water levels. Each wave gauge was calibrated using the WaveLab software package by Aalborg University [2023b]. An arbitrary calibration of a wave gauge is shown in Figure D.1.

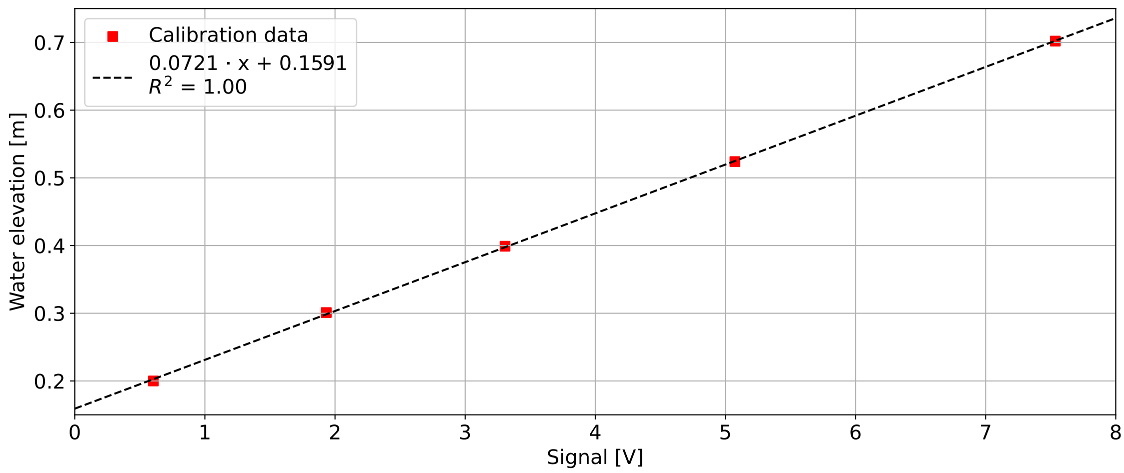

Figure D.1. 5-Point calibration of an arbitrary test campaign.

where R^2 is the coefficient of determination. Due to the change in temperature, resistance in the water can change along with the calibration coefficient a. Therefore, after multiple test campaigns, all wave gauge was calibrated again, to follow the change in calibration coefficient. A significant wave height, H_{m0} and spectral wave period, $T_{m-1,0}$ for each test can be calculated with two different calibration coefficients a and the change can then be interpreted as uncertainty on the wave heights. Figure D.2 shows the incident wave height H_{m0} and $T_{m-1,0}$ computed based on the calibration coefficients from calibration of the wave gauges before and after the test campaign.

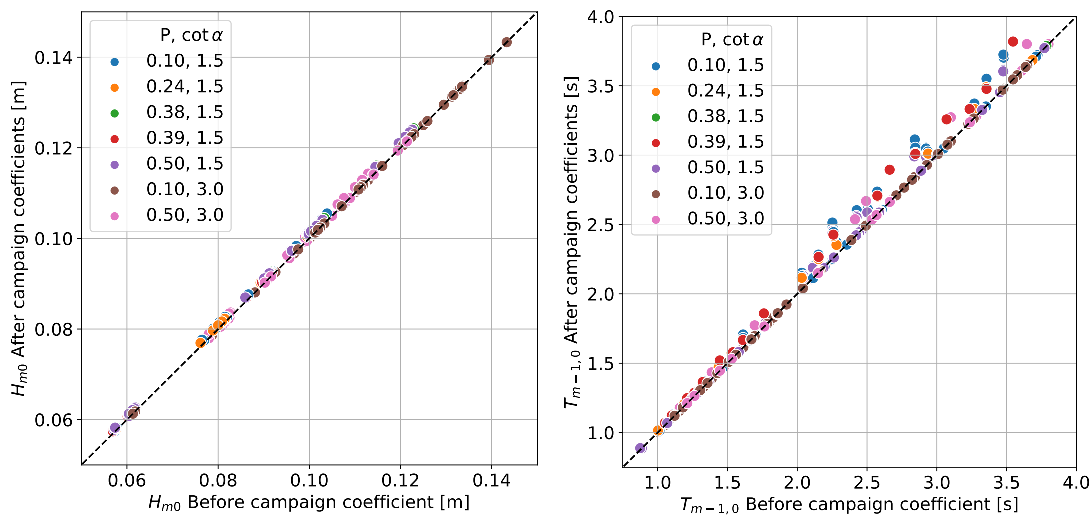

(a) H_{m0}. **(b)** $T_{m-1,0}$.

Figure D.2. Calculated parameters, H_{m0} and $T_{m-1,0}$, based on calibration coefficient before and after test campaign.

Figure D.2 shows very little difference between H_{m0} and $T_{m-1,0}$ from before and after the test campaign, which entails that the uncertainty is low. The maximum difference between H_{m0} in percentage was calculated to be 1.54 % and for $T_{m-1,0}$, 11.6 %. To decrease this uncertainty, a mean value of H_{m0} and $T_{m-1,0}$ is used in the fitting of γ_{P*}. Therefore the uncertainty regarding the measured H_{m0} and $T_{m-1,0}$ is estimated to be approximately 0.8% and 5.8 % respectively. The main reason for this low uncertainty is due to the continuous cleaning of every wave gauge, which is highly recommended in future tests performed in the wave flume at Aalborg University.

D.2 Measured freeboard height

Another highly important factor in the data analysis was the freeboard R_c used for calculating the relative freeboard R_c/H_{m0}. Due to evaporation and air trapped in the hydraulic system, a change in water level was observed in most test campaigns. Therefore, it would be incorrect to use the target freeboard, $R_{c,\text{target}}$, as a constant in the data analysis. The calibration coefficient affects the measured surface elevation, and the wave gauges were deemed inappropriate for accurately measuring the correct freeboard, $R_{c,\text{measured}}$. However, the wave flume at Aalborg University is equipped with a pressure gauge at the bottom plate, which provides water elevation measurements. This information allowed for the correction of the freeboard in some of the tests. Unfortunately, for some of the tests, data from the pressure gauge was unavailable, giving rise to uncertainties for these. The number of tests where data was available for correcting the freeboard is listed in Table D.1.

Table D.1. Number of tests where data was available to correct the freeboard, R_c.

LC	P	cot(α) [-]	n [-]	No. corrected R_c [-]	Percentage [%]
A	0.10	1.5	140	18	12.9
A	0.10	3.0	78	77	98.7
B	0.24	1.5	36	0	0
C	0.38	1.5	36	0	0
D	0.39	1.5	36	0	0
E	0.50	1.5	124	124	100
E	0.50	3.0	41	41	100
Total			491	260	53.0

Table D.1 indicates that approximately half of the tests had the freeboard corrected, while the other half did not. To assess the uncertainty in the remaining data, the difference Δ between the target freeboard $R_{c,\text{target}}$ and the measured freeboard $R_{c,\text{measured}}$ is presented in Table D.2 for the number of tests mentioned in Table D.1.

Table D.2. Percentage error, Δ, between the measured-, $R_{c,\text{measured}}$ and target freeboard, $R_{c,\text{target}}$.

Interval	n [-]	Percentage [%]
$0\% < \Delta < 3\%$	189	72.69
$3\% < \Delta < 4\%$	41	15.77
$4\% < \Delta < 5\%$	21	8.08
$5\% < \Delta < 6\%$	2	0.77
$6\% < \Delta < 7\%$	2	0.77
$7\% < \Delta < 8\%$	2	0.77
$8\% < \Delta < 9\%$	2	0.77
$9\% < \Delta <$	1	0.39
Total	260	100

Table D.2 shows that the vast majority of the data points, which has a corrected freeboard, lies around the 0-4% difference from the target freeboard. The mean percentage difference for all corrected freeboards is calculated to be 2.25 %. The impact on the final conclusion for this, will be discussed in the following section.

D.2.1 Uncertainty on $\gamma_{\mathbf{P}*}$

The uncertainty in the calculated γ_{P*} can be estimated based on the uncertainties in the significant wave height, H_{m0}, and the freeboard, R_c. The uncertainty associated with H_{m0} is determined by considering two different wave heights. As mentioned previously, a mean value of H_{m0} was used for all calculations. The uncertainty is assessed by comparing the difference in γ_{P*} when using the initial H_{m0} based on the first calibration coefficient instead of the mean value. Figure D.3 illustrates the changes in the mean value and 90% confidence interval for all P-values. Note that Figure D.3 only displays the results for $\cot(\alpha) = 1.5$ since no calibration was performed for $\cot(\alpha) = 3.0$ after the test campaigns.

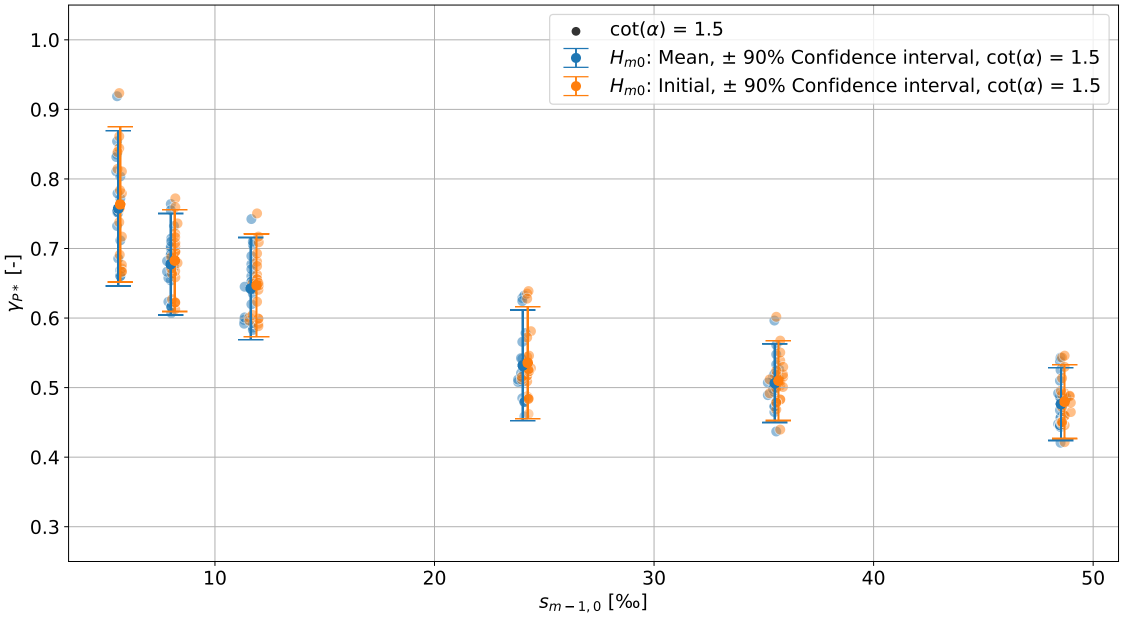

Figure D.3. Change in calculated γ_{P*} based on initially measured H_{m0} and mean value of H_{m0}.

Figure D.3 shows a minimal effect on the mean value and confidence interval of the test data. Therefore, it is not expected to have a significant impact on the final conclusion of the data analysis. Regarding the freeboard, a mean difference of 2.25 % was calculated between the target and corrected R_c. To study the effect of a change in R_c, a conservative value of a 3.5% increment has been applied to the target $R_{c,\text{target}}$ for every test where the freeboard has not been corrected. The results for the 90% confidence interval and mean value for all P-values are shown in Figure D.4

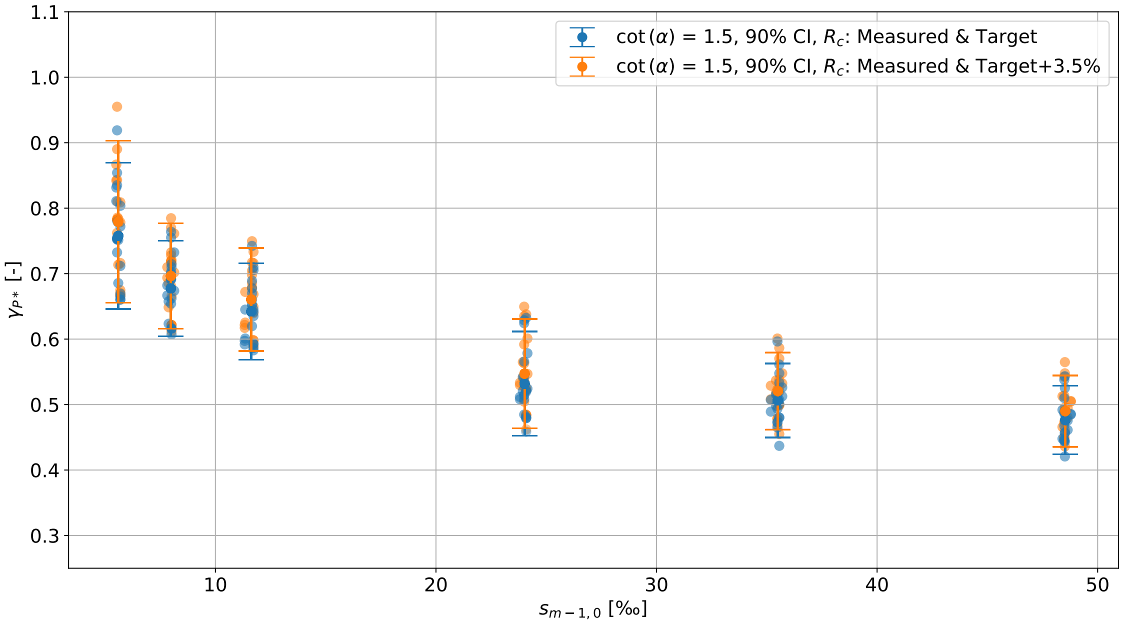

Figure D.4. Change in mean value and 90% confidence interval for all P-values, when adding a 3.5% increment to target $R_{c,\text{target}}$.

Figure D.4 shows a small vertical shift in the confidence interval and mean value. The main reason for the change is the missing correction data for the 140 tests conducted on $P = 0.10$, $\cot(\alpha) = 1.5$, as only 13% of those tests have been corrected (see Table D.1). To further analyse the effect of $P = 0.10$, $\cot(\alpha) = 1.5$, Figure D.5 shows the change in mean value and 90% confidence interval.

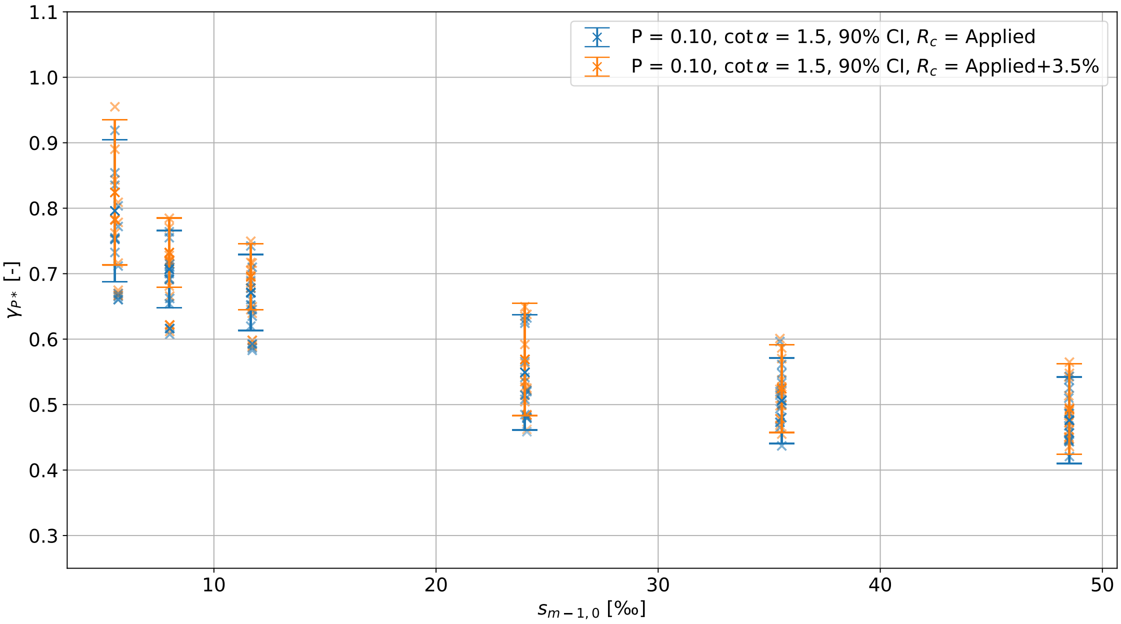

Figure D.5. Change in mean value and 90% confidence interval for $P = 0.10$, $\cot(\alpha) = 1.5$, when adding a 3.5% increment to target $R_{c,\text{target}}$.

Figure D.5 shows a general change in the mean value of approximately 0.025. This is still deemed a small change when tested with a relatively conservative increment. Therefore, the uncertainty regarding the freeboard would not affect the final conclusion of the data analysis. However, since a few data points experienced a difference in target- and measured freeboard of more than 5%, the uncertainty still needs to be taken into consideration with great care and acknowledgement.

D.3 Different wave generation files

Due to the random nature of waves, different wave trains (time series), might cause additional deviation of the results. Geeraerts et al. [2009] tested the COV for varying wave generation files on the same structure. In this present study, the same wave generation file for the respective sea states was repeated for each test campaign, minimising the scatter of data due to different wave trains. However, different wave trains may still be contributing to more scatter of the data and Geeraerts et al. [2009] found that for different wave generation files a COV of 33% can be achieved in the measured overtopping rates. However, in the present study, 5 different wave generation time series for each of the six wave steepness' were tested on the layer composition E, $\cot(\alpha) = 1.5$, to investigate the influence on γ_{P*}. A wave height of $H_{m0} = 0.08$ m was used for every wave steepness, resulting in a total of 30 different wave generation files. The results are depicted in

Figure D.6 and the non-transparent marker (file number 0) indicates the γ_{P*} for the wave generation file used for every other layer composition.

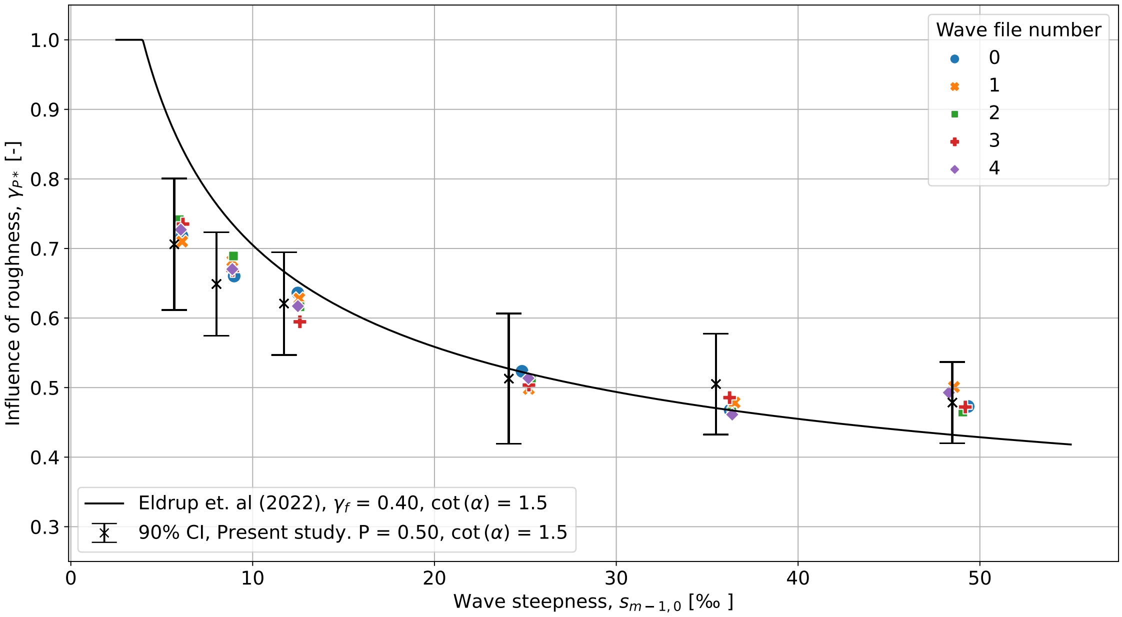

Figure D.6. Mean value and corresponding 90% confidence interval on γ_{P*} for different wave generation time series.

A general scatter of approximately 0.05 for γ_{P*} can be observed, due to different wave generation files. This scatter is mainly due to the difference in measured overtopping as the maximum COV in the present study reached a value of 22% for the high steepness waves. For the measured wave parameters, only a maximum COV of 0.74% and 0.22% was observed for the significant wave height, H_{m0} and spectral wave period, $T_{m-1,0}$, respectively. These observations suggest, that care should be taken, despite the availability of a 90% confidence interval in the present study, as numerous factors can influence its interpretation, however is not expected to alter the final conclusion of the data analysis.

Validation of numerical wave generation E

Wave generation in the numerical wave tank was done by the use of a moving wall boundary, with boundary conditions based on the wavemaker position sampled during the testing of regular wave trains in the wave flume at Aalborg University. To facilitate the check of the numerical wave generation the regular waves were generated in the wave flume without the breakwater model. Figure E.1 shows the wave flume with installed wave gauges (WG) and their respective position. The gauges are numbered such that the gauge closest to the wavemaker ($x = 2.179\,\mathrm{m}$) is numbered 1 (WG1) and the gauge closest to the passive absorber ($x = 14.188\,\mathrm{m}$) is numbered 14 (WG14).

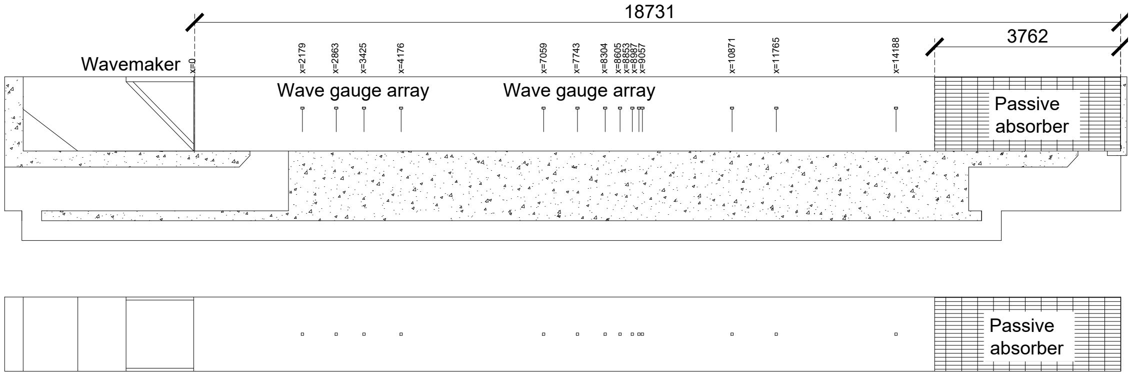

Figure E.1. Wave flume setup verification of numerical wave generation.

To verify the paddle motion and generated waves a simple numerical wave tank was developed. The size and boundaries of the domain are shown in Figure E.2 along with the name of each boundary.

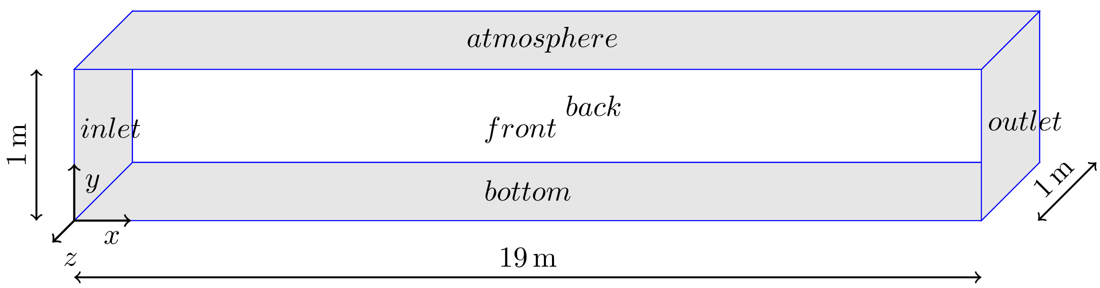

Figure E.2. Size of the computational domain and boundary names.

The boundary type is shown in Figure E.3. Boundary conditions and numerical settings are listed in appendix F. A relaxation zone is implemented for wave absorption near the outlet boundary, illustrated in Figure E.3 by an orange square.

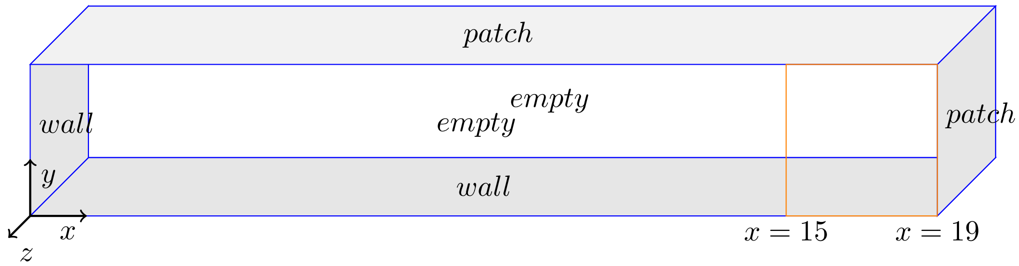

Figure E.3. Boundary types.

Two refinement zones were introduced to increase the resolution around the free surface. The water depth h used for the verification of the wave generation was 0.522 m. The mesh is composed of mainly hexahedral cells with aspect ratio 1 generated using the *blockMesh* utility in OpenFOAM. Refinement of the refinement zones is governed by the refinement level (RL) where cells created with *blockMesh* are referred to as refinement level 0 (RL0). A sketch of the refinement zones is shown in Figure E.4.

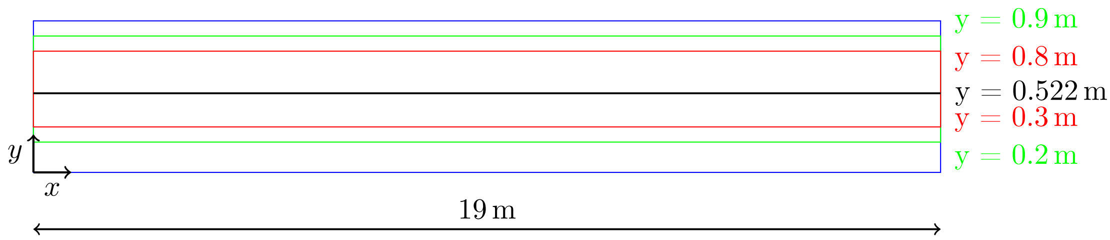

Figure E.4. Mesh refinement of the computational domain.

Cells within a refinement zone are subdivided into two cells in the x and y directions, no subdivision is performed in the z direction. Consequently, a cell from RL0 refined to RL2 (inner red zone in Figure E.4) is subdivided into 64 cells.

The mesh near the moving wall boundary (*inlet* in Figure E.2) is shown in Figure E.5 for the three global mesh sizes explored in the spatial convergence for the wave generation. The cell size is provided as ($dx \times dy$) where the cell measures 100 cm in the z-direction in all three mesh sizes.

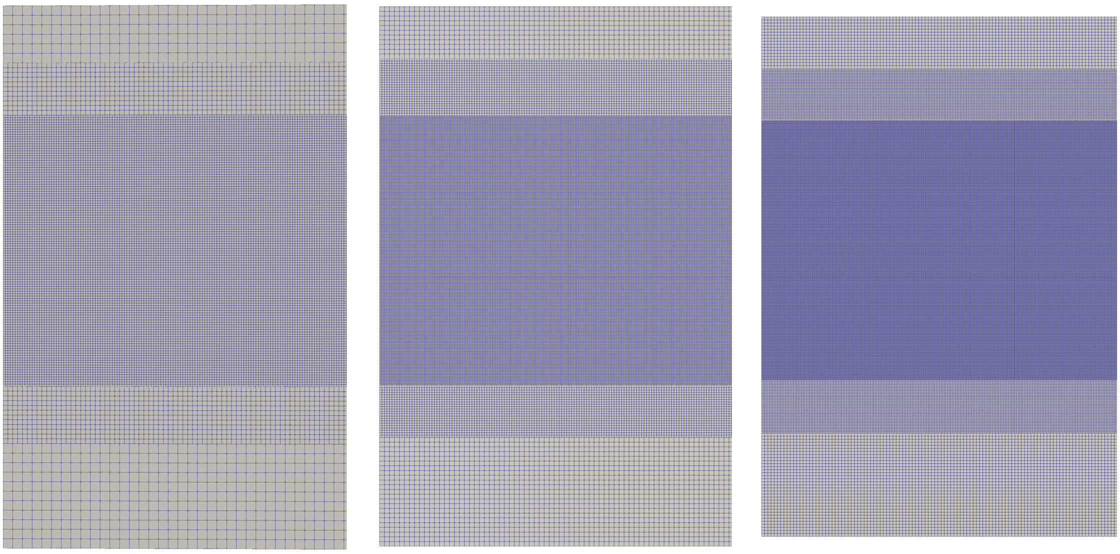

(a) Global cell size 1.85×1.75 cm.

(b) Global cell size 0.83×0.89 cm.

(c) Global cell size 0.62×0.59 cm.

Figure E.5. Discetazation of the computational domain.

Mesh characteristics in relation to the regular wave case used for checking spacial convergence is provided in Table E.1.

Table E.1. Discretization of the domain in relation to wave characteristics.

Global cell size ($dx \times dy$) [cm]	T_p [-]	H [m]	L_p [m]	$cells/L_p$	$cells/H$	Total cells
1.85×1.75	1.46	0.15	2.856	617	34	533013
0.83×0.88	1.46	0.15	2.856	1234	68	2132052
0.62×0.59	1.46	0.15	2.856	1851	103	4797117

The surface elevation measured in the wave flume and the numerical wave tank at $x = 2.179\,\text{m}$ is shown in Figure E.6. A small difference in water depth is present for the numerically generated wave and the generated wave in the flume, this difference was however deemed insignificant. The available resources limited the numerical wave propagation of the two finest cell sizes of $0.83 \times 0.89\,\text{cm}$ and $0.62 \times 0.59\,\text{cm}$, why their signal stops early.

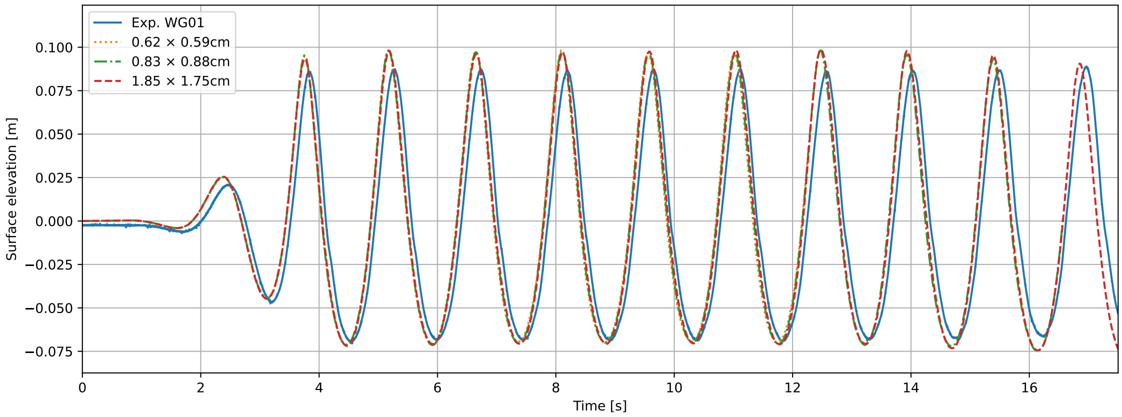

Figure E.6. Measured surface elevation comparison of CFD model and empirical data from wave flume. Signal shown for $x = 2.179\,\text{m}$.

The three global mesh sizes are difficult to distinguish as the surface elevation of all three meshes are approximately equal. However, the crest of the numerical surface elevation is a bit higher than the one measured in the wave flume, the trough is agreeing well with the measured though. A shift in the numerical and the measured signal was also found but the cause of this shift remains inexplicable. The numerical signal was simply adjusted to the measured signal from the flume as shown in Figure E.6. The wave period of the numerical wave also agrees well with the measured data. Therefore, a mesh constructed with a global cell size of $1.85 \times 1.75\,\text{cm}$ with refinement zones and levels as shown in Figure E.4 is deemed sufficient for further computation. The signal for WG13 at position $x = 11.765\,\text{m}$ corresponding to the approximate position of the toe for breakwater model $\cot(\alpha) = 1.5$ is shown in Figure E.7.

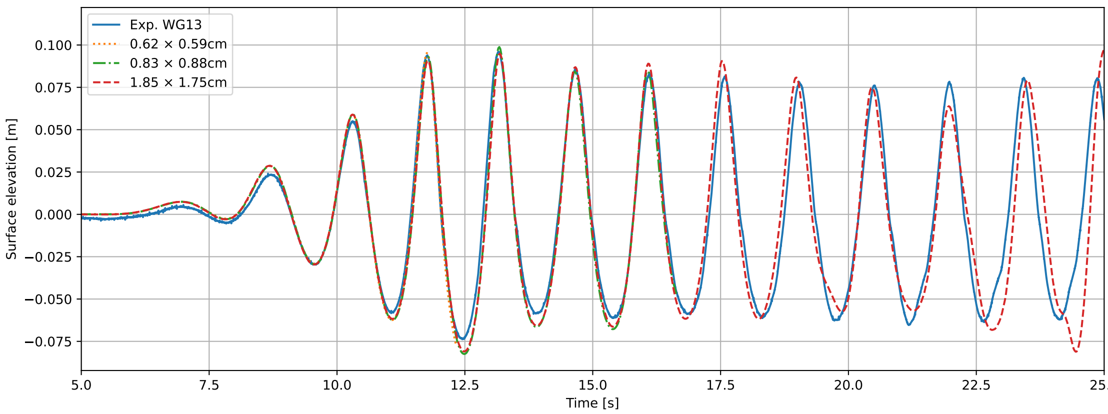

Figure E.7. Measured surface elevation comparison of CFD model and empirical data from wave flume. Signal shown for $x = 11.765\,\text{m}$.

The CFL condition should be investigated to confirm that the simulation is stable for a given Courant-Friedrichs-Lewy (CFL) condition. However no temporal convergence has been checked, the simulations were simply performed with a CFL condition of 0.5. An analysis of the influence of the CFL condition and the time step should be carried out to confirm a stable simulation. This was not confirmed for a CFL condition of 0.5 due to the limitations of the available resources. The time step for a CFL condition of 0.5 at each global mesh size, is shown in Figure E.8 and the maximum CFL value for the simulation time is shown in Figure E.9.

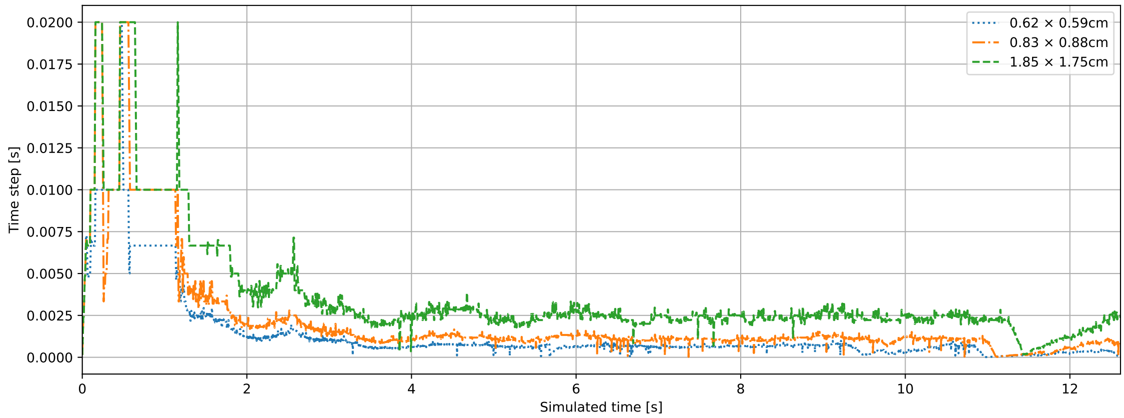

Figure E.8. Time step during the simulated time.

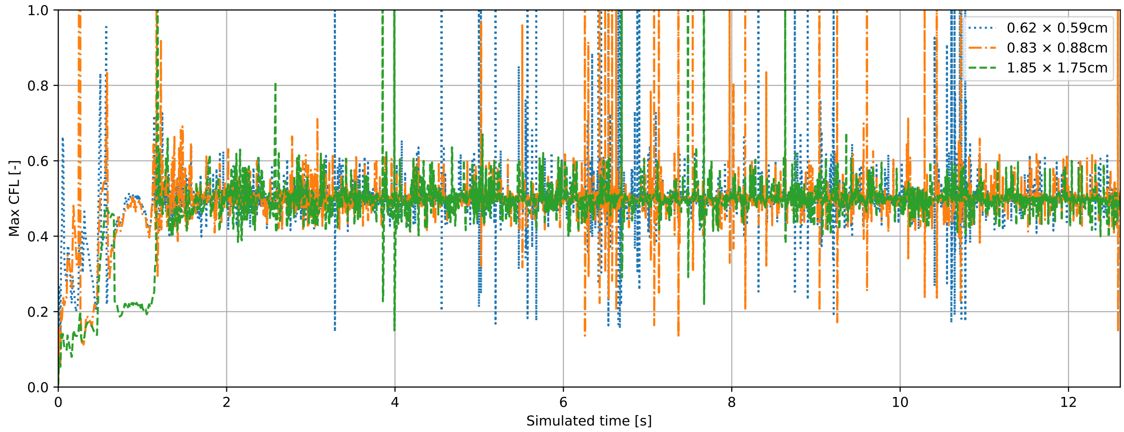

Figure E.9. Maximum CFL value logged during simulation.

F Numerical settings

This appendix contains the general settings, numerical schemes and solvers used for computing the results for the numerical wave tank.

Table F.1. Computational settings.

Solver	interFoam
Turbulence model	laminar

Table F.2. Fluid properties.

	ρ [kg/m^3]	ν [m^2/s]
water	1000	1×10^{-6}
air	1	1.46×10^{-5}

Table F.3. FvSchemes.

Keyword	Schemes	
ddtSchmes	default	Euler
gradSchemes	default	cellLimited Gaus liear 1
divSchemes	div((rhoPhi|interpolate(porosity)),U)	Gauss limitedLinearV 1
	div(phi,alpha)	Gauss vanLeer01
	div((muEff*dev(T(grad(U)))))	Gauss linear
	div(((rho*nuEff)*dev2(T(grad(U)))))	Gauss linear
laplacianSchemes	default	Gauss linear limited 0.5
interpolationSchemes	default	linear
snGradSchemes	default	limited 0.5
fluxRequired	default	no
		p_rgh
		pcoor
		alpha

Table F.4. FvSolution.

Keyword	Setting	
"(cellDisplacement|cellDisplacementFinal)"		
	solver	GAMG
	tolerance	1e-7
	relTol	0
	smoother	GaussSeidel
	cacheAgglomeration	true
	nCellsInCoarsestLevel	10
	agglomerator	faceAreaPair
	mergeLevels	1
"alpha.water.*"	nAlphaCorr	3
	nAlphaSubCycles	1
	cAlpha	1
	icAlpha	0
	MULESCorr	no
	nLimiterIter	6
	alphaApplyPrevCorr	yes
	solver	smoothSolver
	smoother	symGaussSeidel
	tolerance	1×10^{-8}
	relTol	0
	minIter	1
"(pcorr|pcorrFinal)"	solver	PCG
	preconditioner	DIC
	tolerance	1×10^{-6}
	relTol	0
p_rgh	solver	PCG
	preconditioner	DIC
	tolerance	1×10^{-7}
	relTol	0.01
p_rghFinal	$p_rgh	
	tolerance	1×10^{-7}
	relTol	0.01
	minIter	1
U	solver	smoothSolver
	smoother	GaussSeidel
	tolerance	1×10^{-7}
	relTol	0
	minIter	1
UFinal	solver	smoothSolver
	smoother	GaussSeidel
	tolerance	1×10^{-7}
	relTol	0
	minIter	1
PIMPLE	momentumPredictor	no
	nOuterCorrectors	1
	nCorrectors	1
	nNonOrthogonalCorrectors	3
	correctPhi	yes

Table F.5. Boundary conditions.

Boundary	Component	Condition	
inlet	U	type	movingWallVelocity
		value	uniform (0 0 0)
	alpha.water	type	zeroGradient
	p_rgh	type	fixedFluxPressure
		value	uniform 0
	pointDisplacement	type	tabulatedDisplacement
		rotationPoint	(0 0 0)
		timeDataFileName	<paddle input>
		value	uniform (0 0 0)
bottom	U	type	fixedValue
		value	uniform (0 0 0)
	alpha.water	type	zeroGradient
	p_rgh	type	fixedFluxPressure
		value	uniform 0
	pointDisplacement	type	slip
		value	uniform (0 0 0)
superstructure	U	type	fixedValue
		value	uniform (0 0 0)
	alpha.water	type	zeroGradient
	p_rgh	type	fixedFluxPressure
		value	uniform 0
	pointDisplacement	type	fixedValue
		value	uniform (0 0 0)
outlet	U	type	fixedValue
		value	uniform (0 0 0)
	alpha.water	type	zeroGradient
	p_rgh	type	zeroGradient
		value	uniform 0
	pointDisplacement	type	fixedValue
		value	uniform (0 0 0)
atmosphere	U	type	pressureInletOutletVelocity
		value	uniform (0 0 0)
	alpha.water	type	inletOutlet
		inletValue	uniform 0
		value	uniform 0
	p_rgh	type	totalPressure
		U	U
		phi	phi
		gamma	1
		p0	uniform 0
		value	uniform 0
	pointDisplacement	type	fixedNormalSlip
		n	(0 1 0)
		value	uniform (0 0 0)

Table F.6. Boundary conditions (continued).

Boundary	Component	Condition	
front	U	type	empty
	alpha.water	type	empty
	p_rgh	type	empty
	pointDisplacement	type	empty
back	U	type	empty
	alpha.water	type	empty
	p_rgh	type	empty
	pointDisplacement	type	empty
coreFrontCOTA150	U	type	fixedValue
		value	uniform (0 0 0)
	alpha.water	type	zeroGradient
	p_rgh	type	fixedFluxPressure
		value	uniform 0
	pointDisplacement	type	fixedValue
		value	uniform (0 0 0)
coreBack	U	type	fixedValue
		value	uniform (0 0 0)
	alpha.water	type	zeroGradient
	p_rgh	type	fixedFluxPressure
		value	uniform 0
	pointDisplacement	type	fixedValue
		value	uniform (0 0 0)

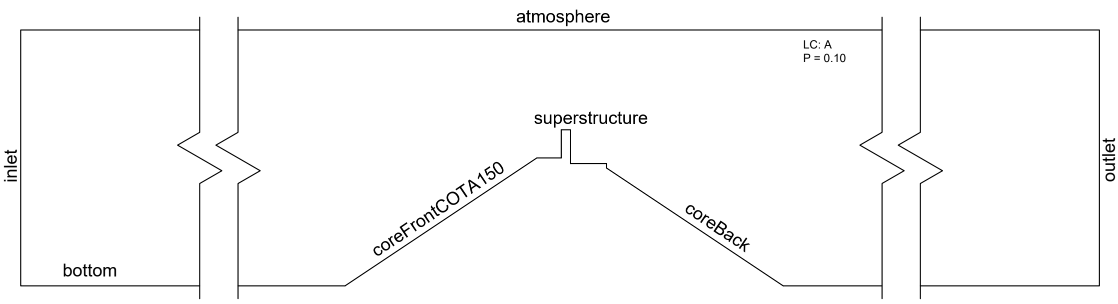

Figure F.1. Boundary names for layer composition A ($P = 0.10$).

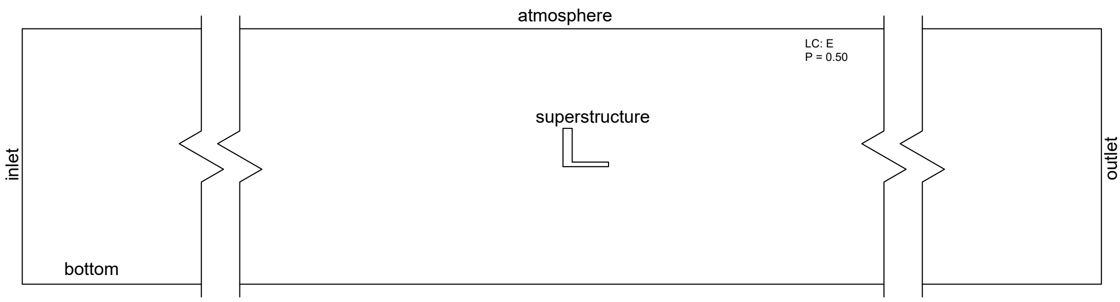

Figure F.2. Boundary names for layer composition E ($P = 0.50$).

Numerical results G

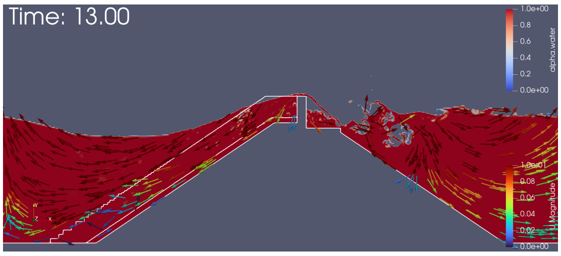

(a) Layer composition A $P = 0.10$.

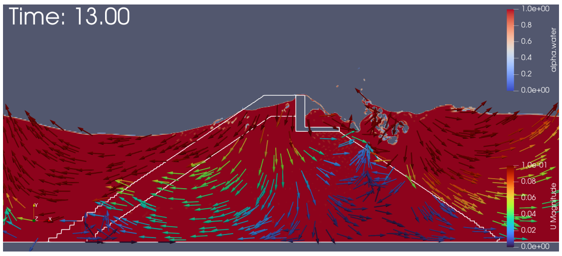

(b) Layer composition E $P = 0.50$.

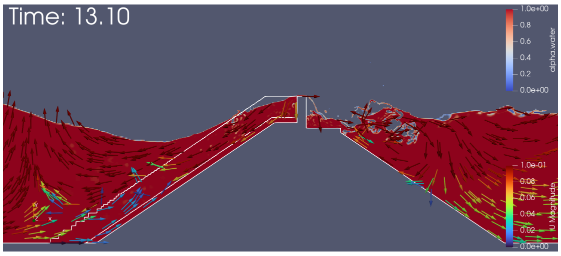

(c) Layer composition A $P = 0.10$.

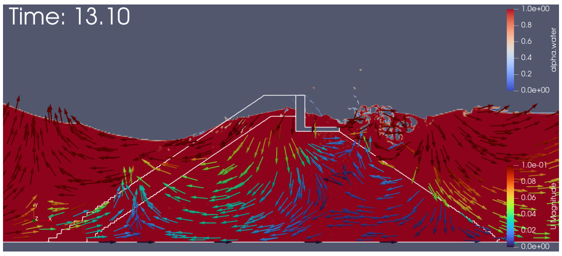

(d) Layer composition E $P = 0.50$.

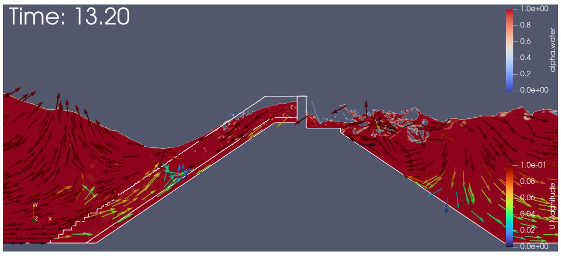

(e) Layer composition A $P = 0.10$.

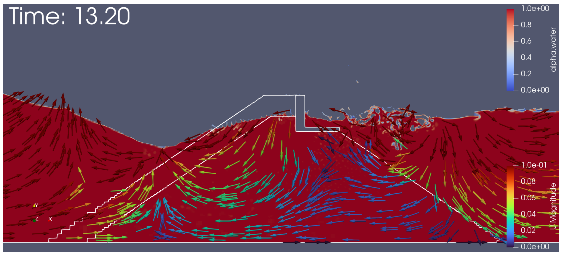

(f) Layer composition E $P = 0.50$.

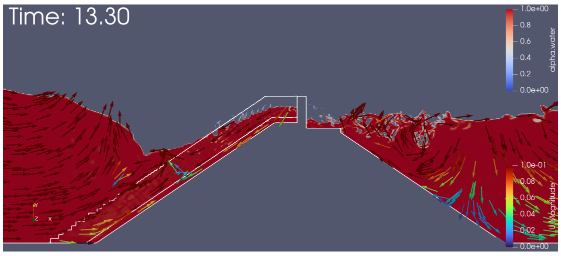

(g) Layer composition A $P = 0.10$.

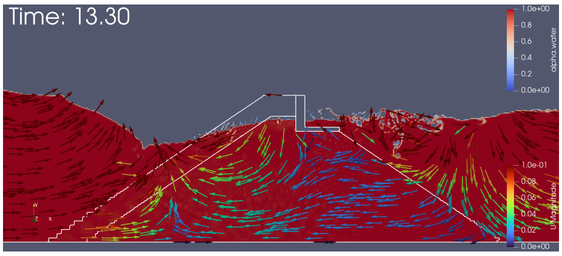

(h) Layer composition E $P = 0.50$.

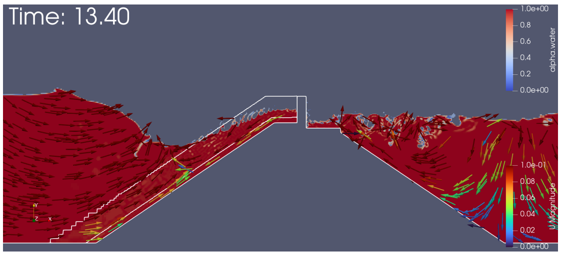

(i) Layer composition A $P = 0.10$.

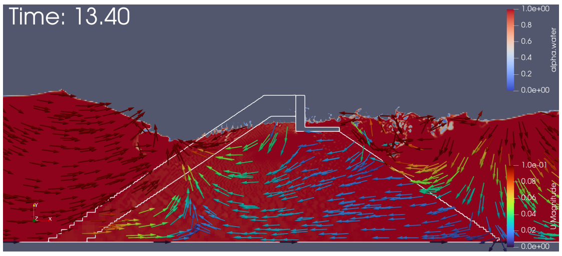

(j) Layer composition E $P = 0.50$.

Figure G.1. Results from numerical wave tank with $h = 0.522\,\text{m}$, $H = 0.15\,\text{m}$ and $T_p = 1.46\,\text{s}$.

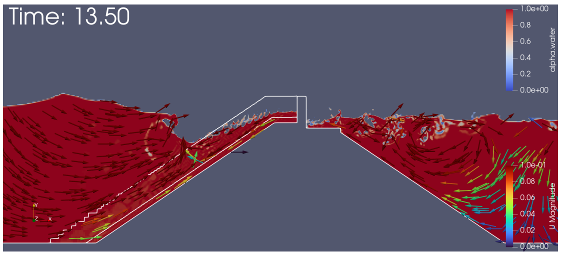

(a) Layer composition A $P = 0.10$.

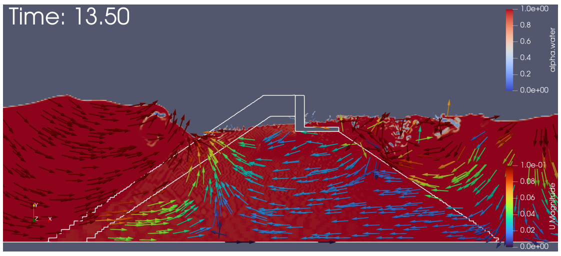

(b) Layer composition E $P = 0.50$.

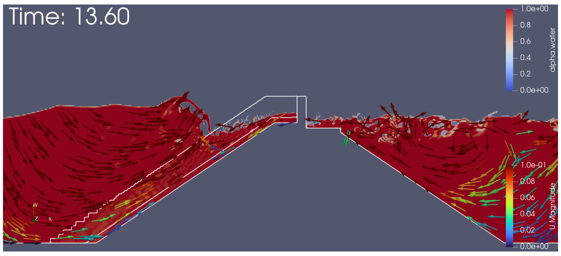

(c) Layer composition A $P = 0.10$.

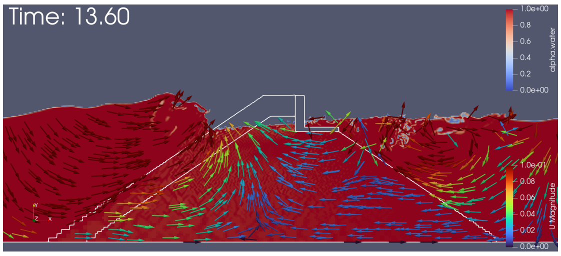

(d) Layer composition E $P = 0.50$.

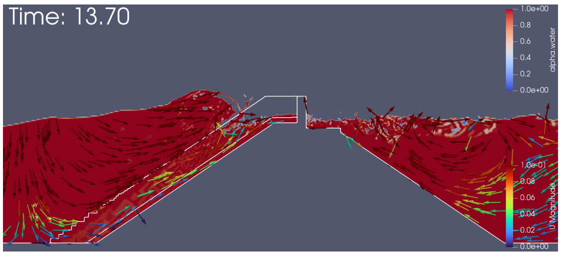

(e) Layer composition A $P = 0.10$.

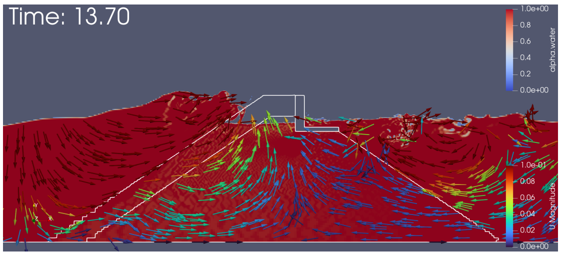

(f) Layer composition E $P = 0.50$.

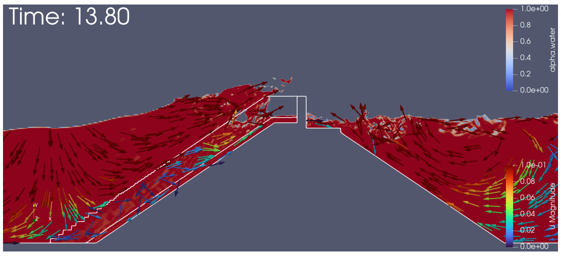

(g) Layer composition A $P = 0.10$.

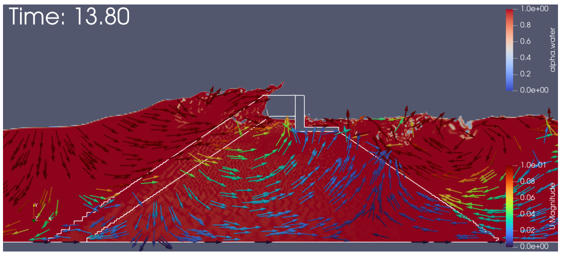

(h) Layer composition E $P = 0.50$.

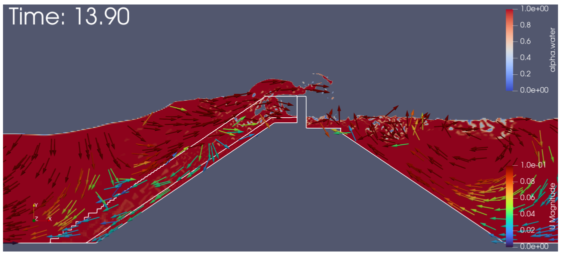

(i) Layer composition A $P = 0.10$.

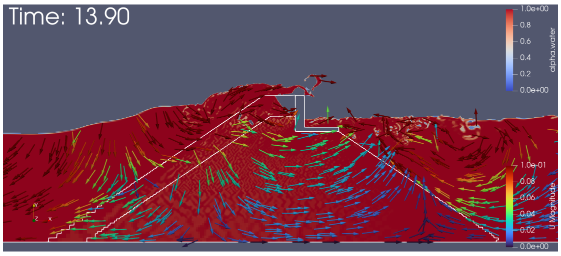

(j) Layer composition E $P = 0.50$.

Figure G.2. Results from numerical wave tank with $h = 0.522\,\mathrm{m}$, $H = 0.15\,\mathrm{m}$ and $T_p = 1.46\,\mathrm{s}$.

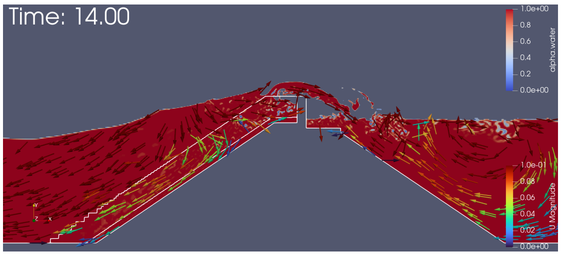

(a) Layer composition A $P = 0.10$.

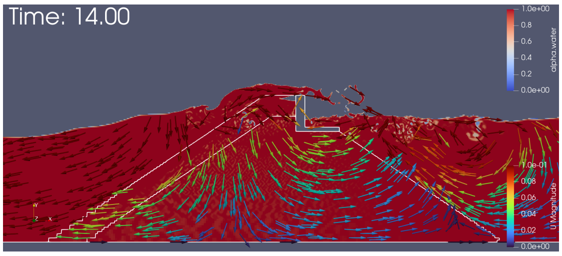

(b) Layer composition E $P = 0.50$.

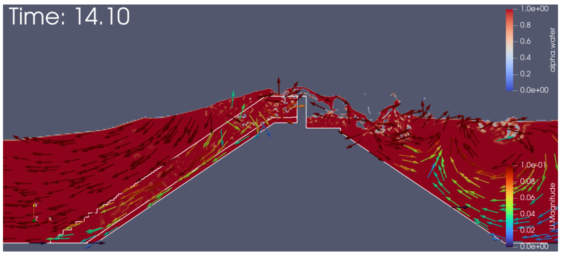

(c) Layer composition A $P = 0.10$.

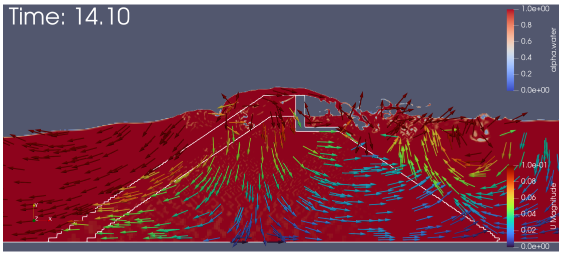

(d) Layer composition E $P = 0.50$.

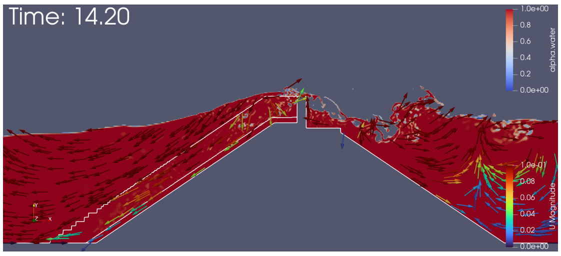

(e) Layer composition A $P = 0.10$.

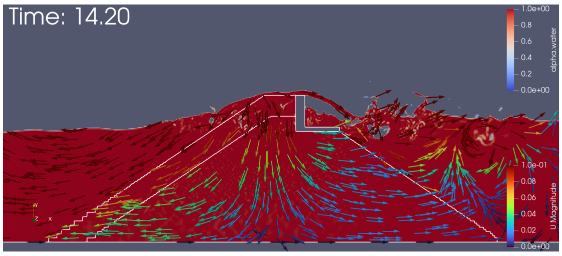

(f) Layer composition E $P = 0.50$.

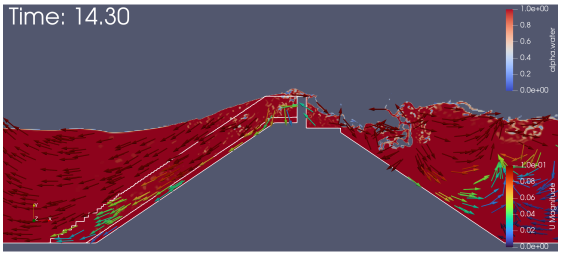

(g) Layer composition A $P = 0.10$.

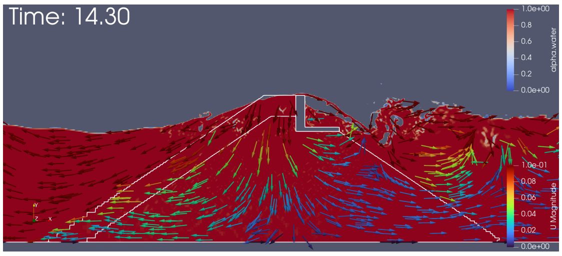

(h) Layer composition E $P = 0.50$.

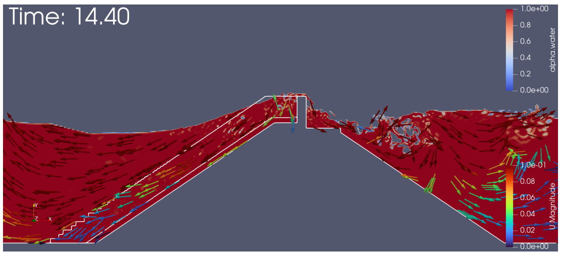

(i) Layer composition A $P = 0.10$.

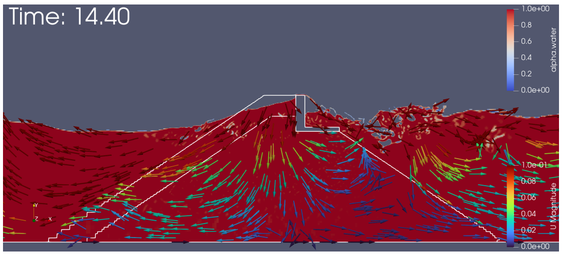

(j) Layer composition E $P = 0.50$.

Figure G.3. Results from numerical wave tank with $h = 0.522\,\mathrm{m}$, $H = 0.15\,\mathrm{m}$ and $T_p = 1.46\,\mathrm{s}$.

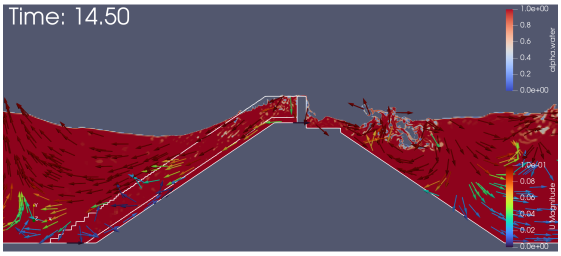

(a) Layer composition A $P = 0.10$.

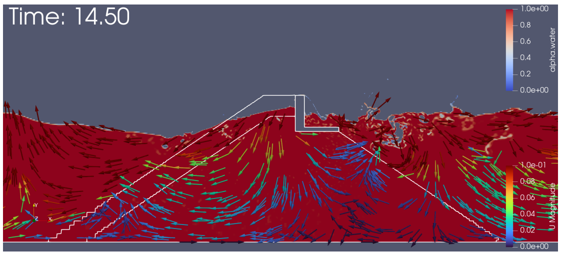

(b) Layer composition E $P = 0.50$.

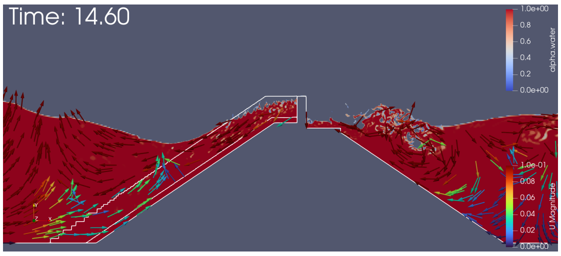

(c) Layer composition A $P = 0.10$.

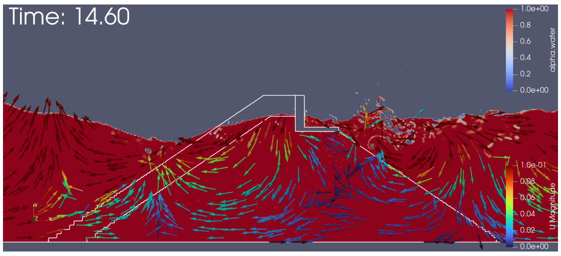

(d) Layer composition E $P = 0.50$.

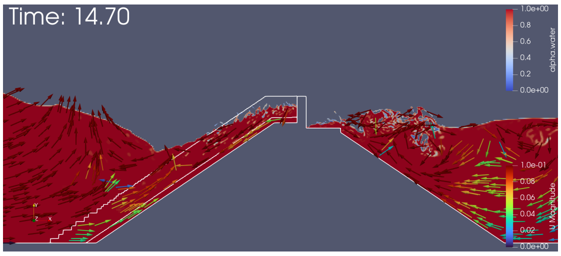

(e) Layer composition A $P = 0.10$.

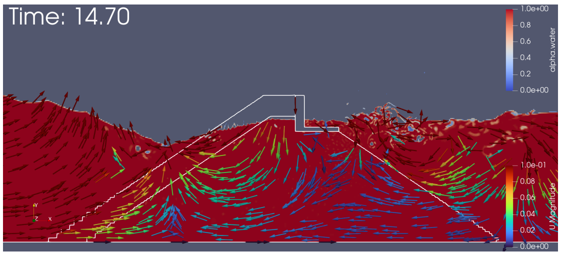

(f) Layer composition E $P = 0.50$.

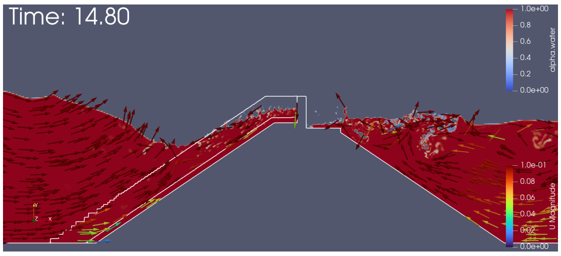

(a) Layer composition A $P = 0.10$.

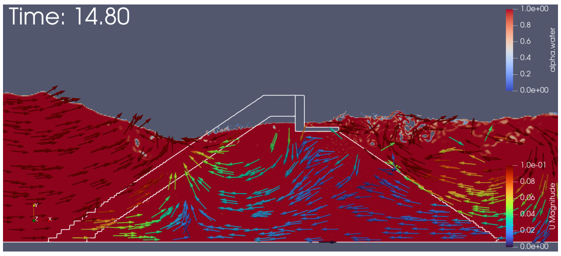

(b) Layer composition E $P = 0.50$.

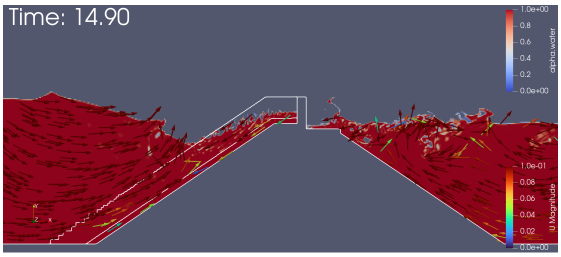

(c) Layer composition A $P = 0.10$.

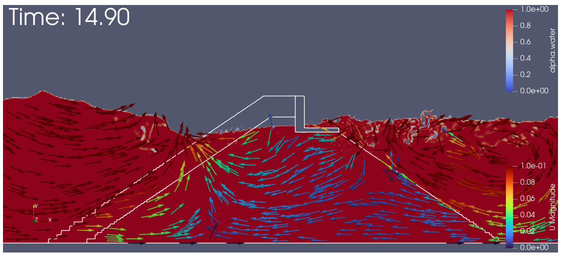

(d) Layer composition E $P = 0.50$.

Figure G.5. Results from numerical wave tank with $h = 0.522\,\mathrm{m}$, $H = 0.15\,\mathrm{m}$ and $T_p = 1.46\,\mathrm{s}$.

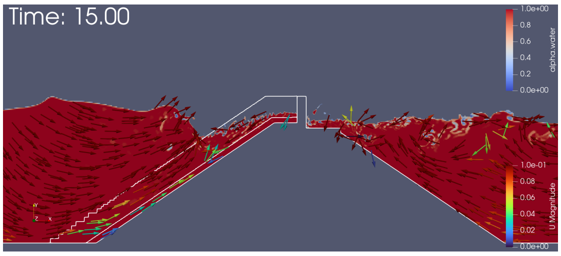

(a) Layer composition A $P = 0.10$.

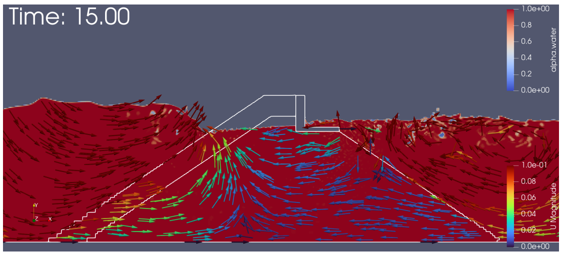

(b) Layer composition E $P = 0.50$.

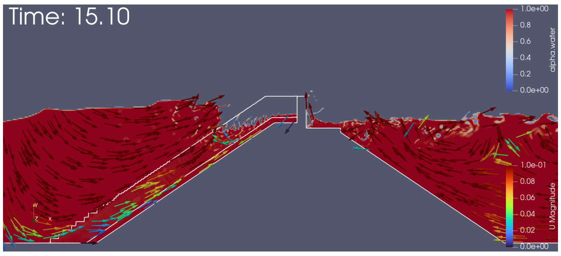

(c) Layer composition A $P = 0.10$.

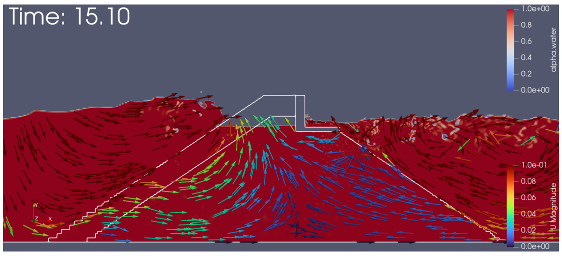

(d) Layer composition E $P = 0.50$.

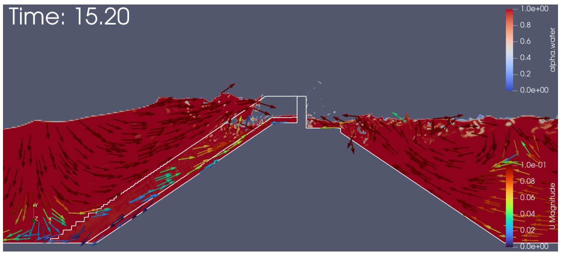

(e) Layer composition A $P = 0.10$.

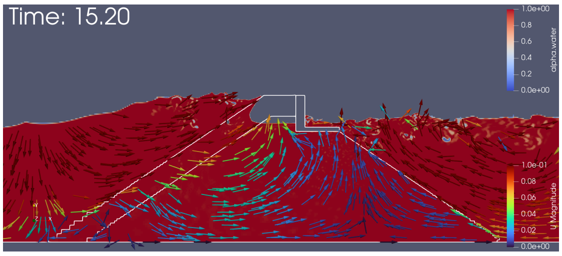

(f) Layer composition E $P = 0.50$.

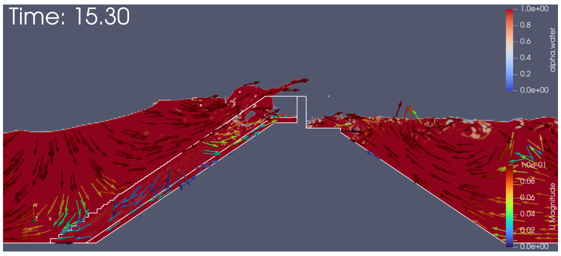

(g) Layer composition A $P = 0.10$.

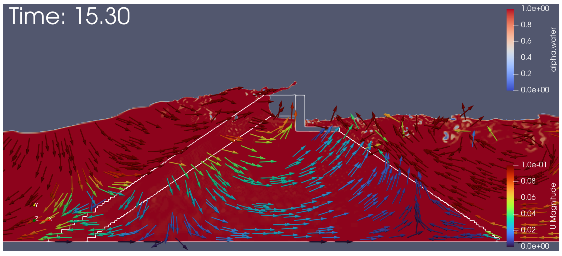

(h) Layer composition E $P = 0.50$.

Figure G.6. Results from numerical wave tank with $h = 0.522\,\mathrm{m}$, $H = 0.15\,\mathrm{m}$ and $T_p = 1.46\,\mathrm{s}$.

G.1 Numerical overtopping measurements.

The discharge q is determined from the overtopping volume of the wave V and the wave period T_p and the domain spans 1 m in the z-direction. The average values for V and q are determined from the overtopping of the last five waves for $T_p = 1.46\,\text{s}$ and 2-3 waves for $T_p = 3.70\,\text{s}$ as shown in the figures of each numerical model.

G.1.1 Sea state $h = 0.522\,\text{m}$, $H = 0.1505\,\text{m}$ and $T_p = 1.46\,\text{s}$

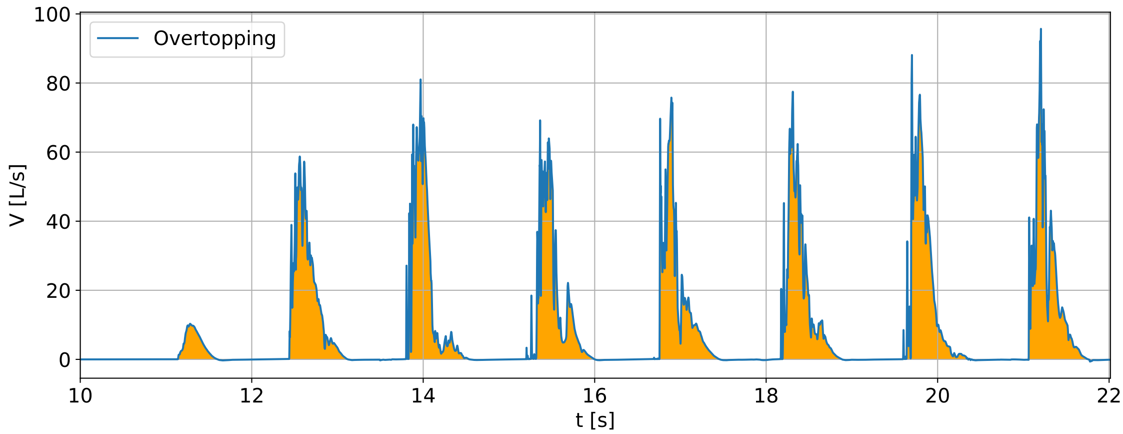

Figure G.7. Numerical overtopping measurements for layer composition A ($P = 0.10$).

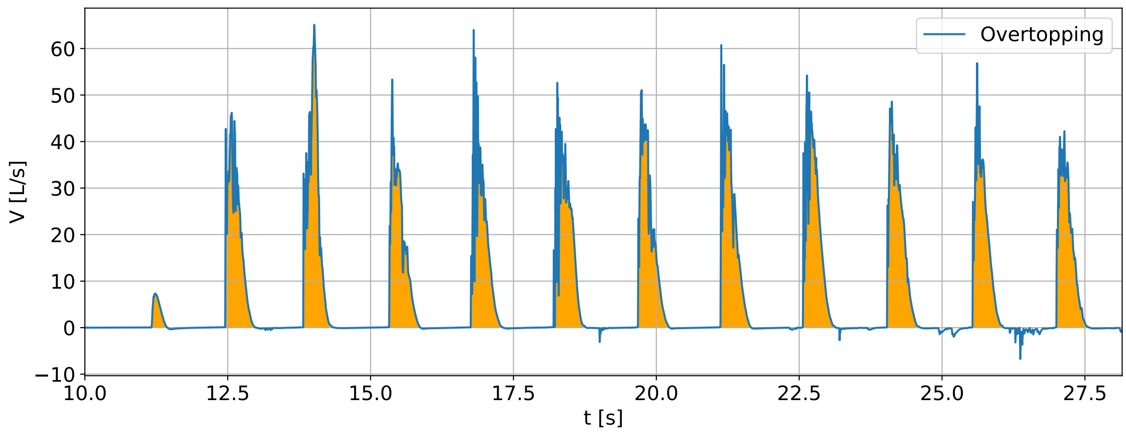

Figure G.8. Numerical overtopping measurements for layer composition E ($P = 0.50$).

Table G.1. Individual overtopping volumes V and discharges q from the numerical model of layer composition A ($P = 0.10$).

Wave no.	1	2	3	4	5	6	7	8	avg.
V [L]	2.25	13.22	14.82	13.62	13.86	14.10	14.99	15.81	14.48
q [L/s/m]	1.54	9.06	10.15	9.33	9.49	9.66	10.27	10.83	9.91

Table G.2. Individual overtopping volumes V and discharges q from the numerical model of layer composition E ($P = 0.50$).

Wave no.	1	2	3	4	5	6	7	8	9	10	11	avg.
V [L]	1.09	10.50	12.77	10.16	10.43	11.31	11.31	12.10	11.60	10.64	10.29	11.20
q [L/s/m]	0.74	7.19	8.75	6.96	7.14	7.75	7.74	7.77	7.95	7.29	7.05	7.67

G.1.2 Sea state $h = 0.522\,\text{m}$, $H = 0.1694\,\text{m}$ and $T_p = 3.70\,\text{s}$

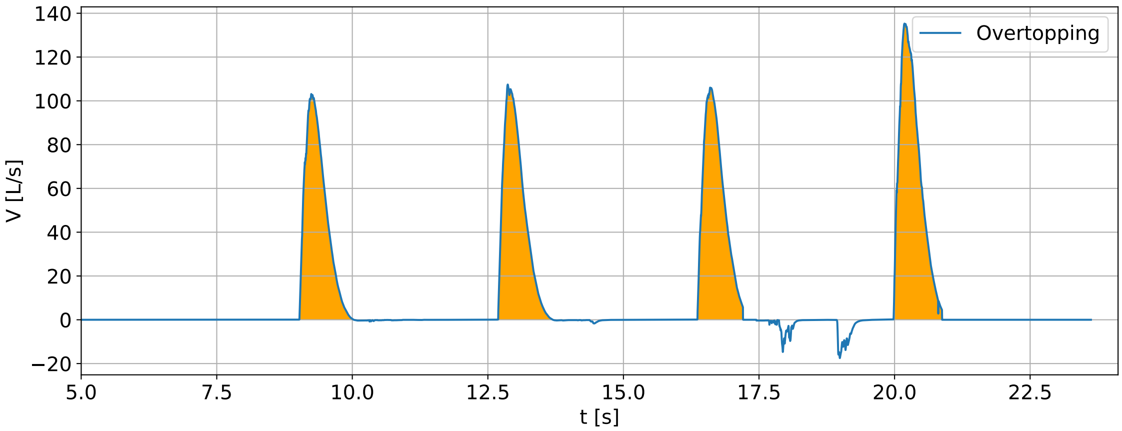

Figure G.9. Numerical overtopping measurements for layer composition A ($P = 0.10$).

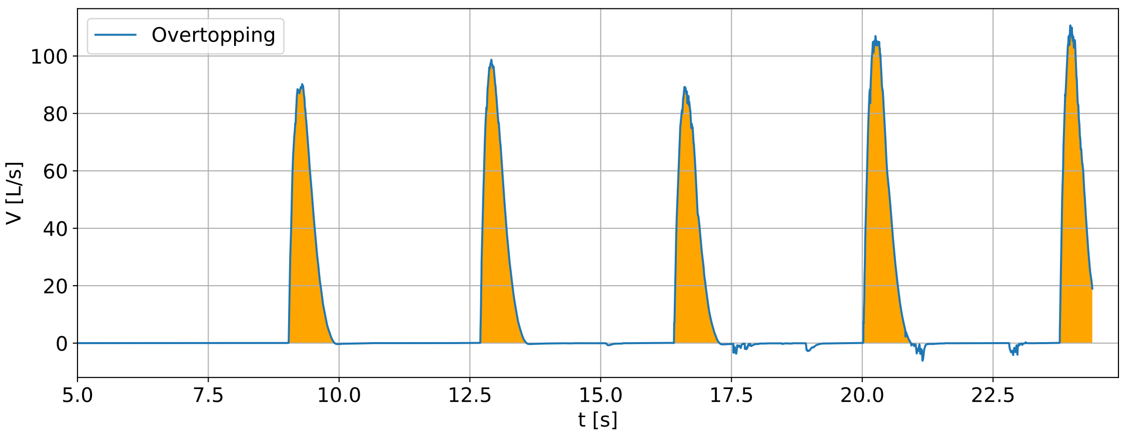

Figure G.10. Numerical overtopping measurements for layer composition E ($P = 0.50$).

Table G.3. Individual overtopping volumes V and discharges q from the numerical model of layer composition A ($P = 0.10$).

Wave no.	1	2	3	4	avg.
V [L]	45.61	47.06	47.36	59.58	53.47
q [L/s/m]	12.33	12.72	12.80	16.10	14.45

Table G.4. Individual overtopping volumes V and discharges q from the numerical model of layer composition E ($P = 0.50$).

Wave no.	1	2	3	4	5	avg.
V [L]	38.73	40.97	37.62	47.16	-	42.39
q [L/s/m]	10.47	11.07	10.17	12.75	-	11.46

G.1.3 Numerical surface elevation measurements.

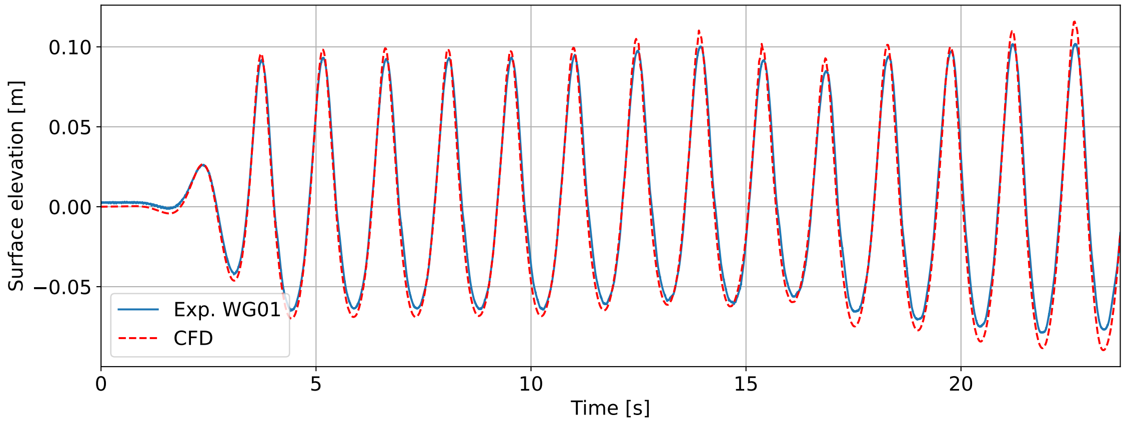

Figure G.11. Numerical and experimental measurements of the surface elevation for layer composition A ($P = 0.10$) at WG01 ($x = 2.179\,\mathrm{m}$).

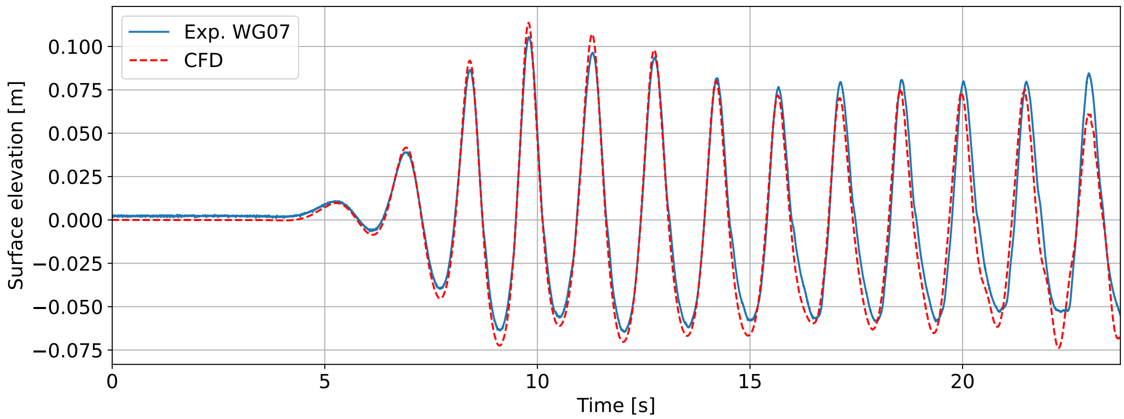

Figure G.12. Numerical and experimental measurements of the surface elevation for layer composition A ($P = 0.10$) at WG07 ($x = 9.057\,\mathrm{m}$).

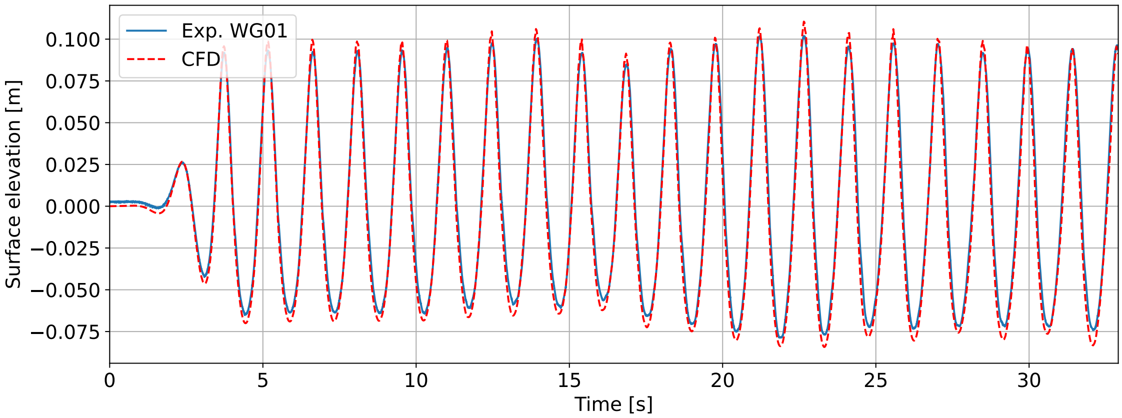

Figure G.13. Numerical and experimental measurements of the surface elevation for layer composition E ($P = 0.50$) at WG01 ($x = 2.179$ m).

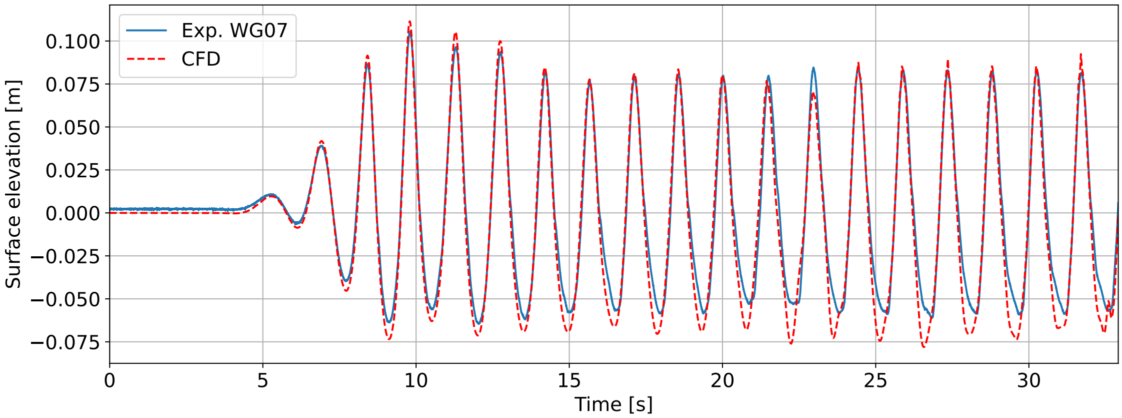

Figure G.14. Numerical and experimental measurements of the surface elevation for layer composition E ($P = 0.50$) at WG07 ($x = 9.057$ m).

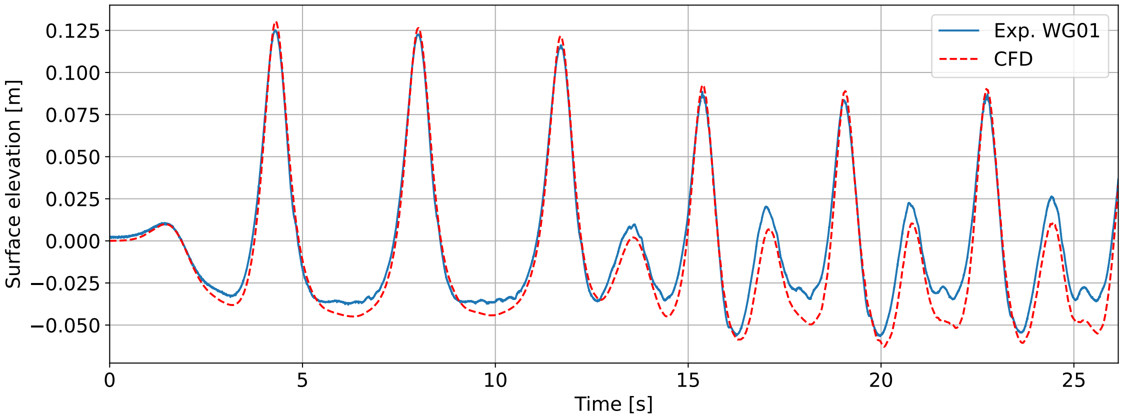

Figure G.15. Numerical and experimental measurements of the surface elevation for layer composition A ($P = 0.10$) at WG01 ($x = 2.179$ m).

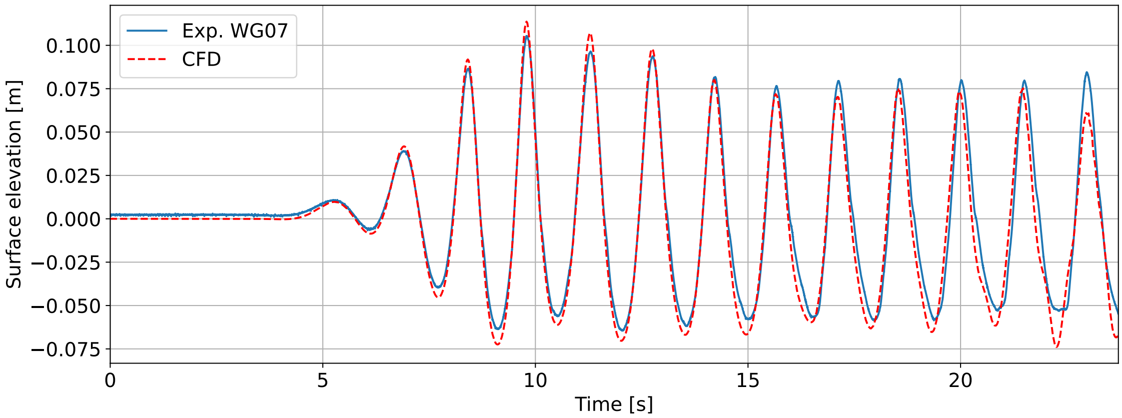

Figure G.16. Numerical and experimental measurements of the surface elevation for layer composition A ($P = 0.10$) at WG07 ($x = 9.057\,\mathrm{m}$).

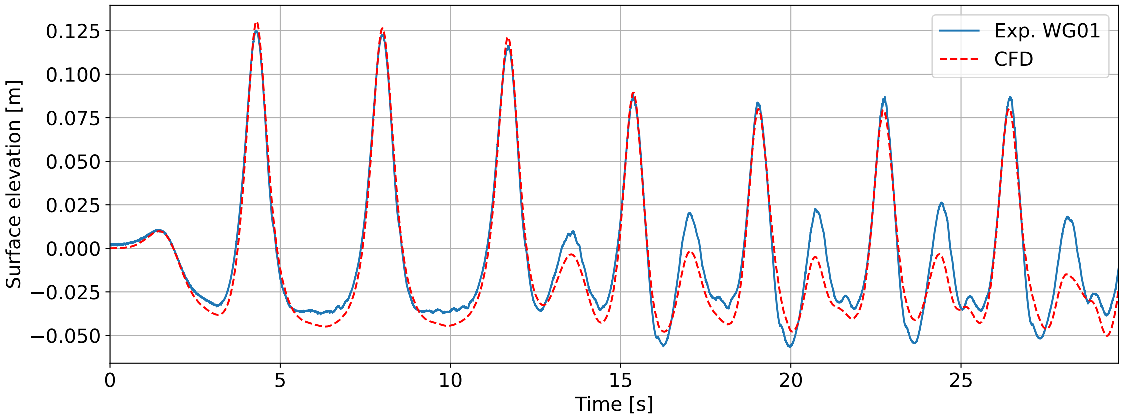

Figure G.17. Numerical and experimental measurements of the surface elevation for layer composition E ($P = 0.50$) at WG01 ($x = 2.179\,\mathrm{m}$).

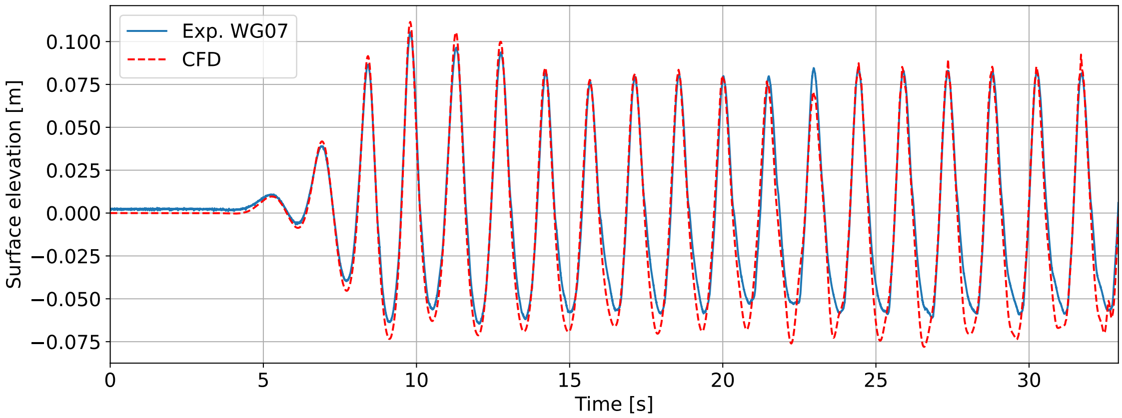

Figure G.18. Numerical and experimental measurements of the surface elevation for layer composition E ($P = 0.50$) at WG07 ($x = 9.057\,\mathrm{m}$).